

SINGLE- AND TWO-PHASE PRESSURE-DRIVEN FLOW TRANSPORT DYNAMICS IN
MICRO-CHANNELS

By

RENQIANG XIONG

A DISSERTATION PRESENTED TO THE GRADUATE SCHOOL
OF THE UNIVERSITY OF FLORIDA IN PARTIAL FULFILLMENT
OF THE REQUIREMENTS FOR THE DEGREE OF
DOCTOR OF PHILOSOPHY

UNIVERSITY OF FLORIDA

2007

©2007 Renqiang Xiong

ACKNOWLEDGMENTS

I would like to express my sincere appreciation to my advisor, Dr. Jacob N Chung, for his invaluable patience, support and encouragement. Without his direction and support, this work would not go further. Many thanks go to Dr. Steve Wereley from Purdue University and Dr. Lichuan Gui from University of Mississippi for helping me to build the Micro-PIV system and tutorials in this research.

Drs. S.A. Sherif, Corin Segal, William E. Lear, Jr, and Jason E. Butler were extremely helpful in several aspects of this research while serving on my supervisory committee. Their suggestions and encouragement have shaped this work considerably.

My fellow graduate students, Kun Yuan, Yunwhan Na, Yan Ji and Mo Bai, have graciously given their time and experience. Finally, I would like to thank my parents and my elder brother's family for the most needed encouragement to finish my studies. Special thanks are given to my wife, Xiaoxing Feng, for years of support. Without her sacrifice, it would have been impossible for me to complete this work.

TABLE OF CONTENTS

	<u>page</u>
ACKNOWLEDGMENTS	3
LIST OF TABLES	6
LIST OF FIGURES	7
NOMENCLATURE	9
ABSTRACT.....	12
CHAPTER	
1 INTRODUCTION	14
1.1 Research Background	14
1.2 Research Objectives.....	16
1.3 Research Overview	16
2 ENTRANCE FLOW AND BEND EFFECT.....	18
2.1 Introduction and Background	19
2.2 Experimental Setup.....	22
2.2.1 Micro-Channels Fabrication.....	22
2.2.2 Apparatus.....	23
2.3 Data Reduction and Analysis.....	24
2.4 Results and Discussion	28
2.4.1 Friction Factor	28
2.4.2 Bend Loss Coefficient	28
2.5 Summary.....	30
3 FLOW STRUCTURES AROUND A BEND.....	36
3.1 Introduction and Background	36
3.2 Micro-PIV System.....	39
3.2.1 Laser Beam Alignment.....	39
3.2.2 Timing Scheme.....	40
3.2.3 Fluorescent Particles Image.....	42
3.2.4 Measurement Depth.....	43
3.3 System Validation.....	44
3.4 Results and Discussion	45
3.4.1 Flow Structures Around The Miter Bend.....	45
3.4.2 Circulation Calculation.....	46
3.4.3 Shear Strain	47
3.5 Summary.....	47

4	ADIABATIC GAS-LIQUID TWO-PHASE FLOW.....	62
4.1	Introduction and Background	62
4.2	Experimental Apparatus	66
4.3	Results and Discussion	68
4.3.1	Two-Phase Flow Patterns	68
4.3.2	Flow Regime Maps.....	71
4.3.3	Comparison With Prior Mini-Channel Flow Map.....	73
4.3.4	Time-Averaged Void Fraction	74
4.3.5	Frictional Pressure Drop.....	77
4.4	Summary.....	77
5	MICRO-BUBBLE DISPENSER.....	91
5.1	Introduction and Background	91
5.2	Experimental Setup.....	94
5.2.1	Dispenser Fabrication.....	94
5.2.2	Apparatus.....	94
5.3	Numerical Simulation.....	96
5.4	Results and Discussion	98
5.4.1	Bubble Break-Up.....	98
5.4.2	Bubble Distribution and Bubble Size	99
5.4.3	Bubble Frequency.....	100
5.4.4	Effect of Viscosity and Surface Tension	102
5.4	Summary.....	103
6	CONCLUSIONS AND RECOMMENDATIONS	115
6.1	Accomplishments and Findings.....	115
6.2	Future Research	116
6.2.1	Experimental Study	116
6.2.2	Numerical Study	117
	APPENDIX TIMING PROGRAM FOR MICRO-PARTICLE IMAGE VELOCIMETRY ...	118
	LIST OF REFERENCES	119
	BIOGRAPHICAL SKETCH	125

LIST OF TABLES

<u>Table</u>		<u>page</u>
2-1	Dimensions of three groups of micro-channels	31
2-2	Comparison of current pipe lengths with those of entrance regions.....	31
3-1	Specification of the Nd:YAG laser (Continuum Minilite II).....	48
3-2	Calculated vortex circulation	48
4-1	Generalized two-phase frictional pressure-drop correlations.	79
4-2	Non-dimensional parameters for a macro-channel and micro-channels.....	80

LIST OF FIGURES

<u>Figure</u>	<u>page</u>
2-1 Three groups of fabricated micro-channels	32
2-2 Experimental pressure drop measurement apparatus.....	33
2-3 Pressure drop defect $K(x^+)$ vs x^+	33
2-4 Experimental pressure gradients without removing the entrance effect ($\Delta P_l - \Delta P_{sh}$)/($L_l - L_{sh}$) vs Re number.....	34
2-5 Experimental friction factor vs. Re number in straight micro-channels.....	34
2-6 Bend additional pressure drops vs. Re number in serpentine micro-channels	35
2-7 Bend loss coefficients vs Re number in serpentine micro-channels.....	35
3-1 Top view of the optical layout of the laser beam alignment.....	49
3-2 Timing diagram for the two lasers and CCD camera	49
3-3 Fluorescent images at straight and serpentine micro-channels.....	50
3-4 Schematic of micro-PIV system	50
3-5 Photo of the optical subsystem	51
3-6 Photo of the laser beam alignment component.....	51
3-7 Micro-PIV results for low speed flow.	52
3-8 Typical velocity vector in the serpentine micro-channel at $Re = 500$	53
3-9 Flow structure at the outer wall and at the inner wall.....	54
3-10 Streamlines at different Re numbers.....	57
3-11 Total vortex circulation vs. Reynolds number.....	59
3-12 Distribution patterns of shear strain rates	60
4-1 Schematic of the flow visualization apparatus and the mixer.....	81
4-2 Photograph of micro-channels and schematic of the micro-channel.....	83
4-3 Typical flow patterns in the micro-channel.....	83

4-5	Flow regime maps for three micro-channels	85
4-6	Flow map comparison between micro-channel and mini-channel predicted by the Weber number model.....	87
4-7	Measured time-averaged void fraction results vs two previous correlations.....	87
4-8	Comparison between the new correlation and experimental data	88
4-9	Ratio of predicted and experimental time-averaged void fraction vs. homogeneous void fraction β	88
4-10	Comparison between the experimental data and the models ($D_h = 0.412\text{mm}$).....	89
5-1	Schematic of the co-flowing micro-channel.....	104
5-2	3-D image and depth measurement by the optical profiler.....	104
5-3	Schematic of the experimental flow visualization apparatus.....	105
5-4	Schematic of micro-PIV measurement for micro-bubble dispenser.....	105
5-5	Schematic of 3D CFD mesh	106
5-6	Time evolution of the periodic bubble generation process ($Q_g = 6.3\text{ml/h}$, $Q_l = 21\text{ml/h}$, Air+Water) and the prediction by CFD simulation	106
5-7	Unsteady break-up process at different flow rates.....	107
5-8	Instantaneous micro-PIV measurements around the barrier ($Q_l = 21\text{ml/h}$, $Q_g = 6.3\text{ml/h}$).....	107
5-9	Bubble distribution along the channel at different flow rates.....	110
5-10	Dependence of the bubble length L on the gas flow rate ($Q_l = 18\text{ml/h}$) and liquid flow rate ($Q_g = 5\text{ml/h}$).....	110
5-11	Dimensionless ratio (L/w) with the ratio of gas and liquid flow rates	111
5-12	Bubble frequency with different liquid and gas flow rates (Air +water).....	112
5-13	Bubble shapes at different viscosities and surface tensions.....	113
5-14	Dimensionless ratio (L/w_b) with the ratio of gas and liquid flow rates.....	112
5-15	Dimensionless ratio (L_e/w) with the ratio of gas and liquid flow rates.....	114

NOMENCLATURE

A	Area [m^2]
A_i	Area of interrogation window [μm^2]
B	Coefficient in Eq. 2-6
Bo	Bond number
C	Coefficient in Eq. 4-4
C_v	Volumetric concentration [μm^{-3}]
C_0	Coefficient in Eq. 4-1
Ca	Capillary number
dP/dz	Pressure gradient [Pa/m]
D	Diameter [mm]
f	Fraction factor
fre	Frequency [$1/\text{s}$]
g	Gravity acceleration [m/s^2]
j	Superficial velocity [m/s]
K	Pressure drop defect
K_b	Bend loss coefficient
L	Length [mm]
L_d	Entrance length [m]
m	Mass transfer rate [g]
n	Refraction index
N	Total number
NA	Numerical aperature

P	Pressure [Pa]
Q	Flow rate [ml/min]
Re	Reynolds number
S	Depth of micro-channels [mm]
T	Time [s]
u	Local velocity at x direction [m/s]
U	Mean velocity [m/s]
V_{gj}	Mean drift velocity [m/s]
W/w	Width [mm]
We	Weber number
X	Martinelli parameter
x	The coordinate along the length
x^+	Dimensionless entrance length
y	The coordinate along the width
Z_m	Measurement depth [μm]

Greek letters

Δ	Variable difference
α	Aspect ratio
β	Homogeneous void fraction
Γ	Circulation [mm^2/s]
δ	Differential value
λ	Wavelength of light in a vacuum [μm]
μ	Viscosity [$\text{kg}/\text{m}\cdot\text{s}$]

θ	Light collection angle
ρ	Density [kg/m ³]
σ	Surface tension [N/s]

Subscripts

b	90° bend
c	Cross-section
dev	Developing and developed flow
exp	Experimental result
fd	Fully developed
G/g	Gas
GS	Superficial gas
h	Hydraulic diameter
i	Particle image
io	Inlet and outlet
L/l	Liquid
LS	Superficial liquid
l	Long straight micro-channel
m	Other type of flow patterns
p	Fluorescent particles
s	Serpentine micro-channel
sh	Short straight micro-channel

Abstract of Dissertation Presented to the Graduate School
of the University of Florida in Partial Fulfillment of the
Requirements for the Degree of Doctor of Philosophy

SINGLE- AND TWO-PHASE PRESSURE-DRIVEN FLOW TRANSPORT DYNAMICS IN
MICRO-CHANNELS

By

Renqiang Xiong

August 2007

Chair: Jacob N Chung
Major: Mechanical Engineering

The pressure-driven flow in a micro-channel is an important component of the micro-scale fluid dynamics and widely applied in many fields such as cooling of IC chips, micro-fuel cell fluid transport, and lab-on-a-chip. To enrich the current fundamental knowledge of micro-scale fluid dynamics, some experimental and numerical investigations were performed.

The pressure drops of liquid flow in straight and serpentine micro-channels with hydraulic diameters of 0.209 mm, 0.412 mm, and 0.622 mm were evaluated. To segregate the bends and entrance effects individually from the total pressure drop, for each size, three types of micro-channels: straight short, straight long, and long serpentine, were fabricated. An in-house micron-resolution particle image velocimetry system (micro-PIV) was built at the University of Florida and used to obtain the detailed velocity vector field in micro-scale channels. The friction factor result shows that the conventional theory is still valid under the current channel size. The additional pressure drop is consistent with the flow structure around the bend measured by the micro-PIV.

Adiabatic nitrogen-water flow patterns and void fractions in straight micro-channels were experimentally investigated. Gas and liquid superficial velocities were varied from 0.06-72.3 m/s and 0.02-7.13 m/s, respectively. The instability of flow patterns was observed. Four groups of

flow patterns including bubbly-slug flow, slug-ring flow, dispersed-churn flow and annular flow were observed in micro-channels of 0.412 mm and, 0.622 mm while in the micro-channel of 0.209 mm, the bubbly-slug flow became the slug-flow and the dispersed-churn flow disappeared. The current flow regime maps showed that the transition lines shifted to a higher gas superficial velocity due to a dominant surface tension effect as the channel size was reduced. The void fractions hold a non-linear relationship with the homogeneous void fraction as oppose to the relatively linear trend for the mini-channels. A new correlation was developed to predict the non-linear relationship that fits most of the current experimental data within $\pm 15\%$.

Bubble generation in a simple co-flowing micro-channel with a cross-section area of $1.69 \times 0.07 \text{ mm}^2$ was also investigated. Mixtures of water-glycerol and water-Tween 20 were also used to obtain the effects of viscosity and surface tension. The break-up dynamics can be predicted using a three dimensional incompressible two-phase flow numerical model based on the volume of fluid (VOF) method. The bubble length L is dependent on the liquid flow rate Q_l and gas flow rate Q_g . Further more the ratio of L to the channel width w is a function of the ratio of gas and liquid flow rates Q_g/Q_l which is similar to that previously used in the T-junction case. The bubble frequency is found to be related to w , channel depth h , and $Q_l Q_g / (Q_g + Q_l \cdot \pi/4)$, and shows a good agreement with the experimental data at the low frequency region. Different bubble shapes can be obtained at different liquid viscosities and surface tensions. The ratio L/w can still be predicted by a modified equation which uses the real bubble width w_b or an equivalent bubble length L_e .

CHAPTER 1 INTRODUCTION

Micro-scale fluid dynamics usually refers to the dynamics of fluid flow in the devices with length scales less than one millimeter. Studies of such fluid-related phenomena have long been an important part of the fluid mechanical component (Batchelor 1977). Due to the availability of MEMS fabrication methods (Ho and Tai 1998; Stone & Kim 2001), methods for fabricating individual and integrated flow configurations with length scales on the order of tens and hundreds of microns and smaller, micro-scale fluid dynamics research has received enormous recent attention and been widely applied in many fields such as biotechnology (Beebe et al. 2002), cooling of IC chips (Zhang et al. 2002), micro-fuel cell (Heinzel et al. 2002) and lab on a chip (Erickson and Li 2004). In many applications, a valuable feature of microflows is that the dynamics in a single channel can be replicated in many channels, so understanding the fundamental knowledge of fluid motion and associated transport processes in micro-channels is quite important for the micro-scale fluid transport system design.

In this study, we experimentally and numerically investigated many flow features of pressure-driven single- and two-phase flow in micro-channels to enrich the current fundamental knowledge of micro-scale fluid dynamics.

1.1 Research Background

Micro-scale flows can be manipulated using many kinds of external fields such as pressure, electric, magnetic, capillary, etc. Pressure-driven flow is an indispensable component in micro-scale fluid dynamics research. It is widely used in micro-heat exchanger (Brandner et al. 2000), and the pressure drop is a critical parameter to design the micro-pumps. For single phase liquid flow in straight micro-channels, many scientists have published numerous papers on the relationship between the friction factor and Re number in the past fifteen years. Some of them

found for a liquid flow an increase of the friction factor with the Re number including Wu and Little (1983), Peng and Peterson (1996), Mala and Li (1999), Qu et al. (2000), and Li et al. (2003). They attributed it to surface roughness effect or the early transition to turbulent flow ($Re=300-500$) in straight micro-channels. However, recent studies showed general agreement with theoretical macro-scale predictions for friction factors including Judy et al. (2002), Wu and Cheng (2003), Hetsroni et al. (2005), and Kohl et al. (2005). They attributed the deviation from the theoretical prediction in the previous literatures to the size measurement uncertainties and neglect of the entrance effects. Hence, the relationship is not clear yet. The studies for liquid flow in serpentine micro-channels just started (Lee et al. 2001; Maharudrayya et al. 2004). It is of concern in the field of micro-fuel cell.

Most measurements of microflows have been performed with optical microscopes. An adaptation of particle image velocimetry known as micro-PIV can yield a spatial resolution of the flow field of approximately one micron (Santiago et al. 1998). Due to the high expense of purchasing such a commercial system, around \$500,000, building an in-house micro-PIV system became timely to speed up the progress of micro-scale fluid dynamics research at the University of Florida.

Two-phase flow in micro-channels is also a major research subject in micro-scale fluid dynamics. Recent researches show that the surface tension becomes dominant when the channel size decreases which may result in a big change in the flow pattern and flow map, even the void fraction (Kawahara et al. 2002). A study of the size effect on those flow features need to be performed to provide a clear image of the micro-scale two-phase flow.

Micro-bubble dispenser is one of the fundamental elements in a lab-on-a-chip system. It can be integrated with other microfluidic components including valves, pumps, actuators,

switches, sensors, mixers, filters, separators, heaters, etc. to succeed with chemical synthesis, analysis, and reactions using only very small fluids volumes (Stone et al. 2004). Recent studies have reported several bubble dispensers but with complex structures (Ganan-Calvo and Gordillo 2001; Garstecki et al. 2004). New dispensers with simple structures that are easy to be scaled up or multiplexed need to be designed and tested.

1.2 Research Objectives

This research is performed to provide fundamental understanding for the following flow features in micro-scale:

- Friction factor, entrance effect and bend effect for a liquid flow in micro-channels.
- Flow structure around the bend and its correspondence to the additional pressure drop.
- Flow patterns, time-averaging void fraction and two-phase frictional pressure drop for gas-liquid two-phase flow in micro-channels
- Micro-bubble dispenser with a simple structure to generate uniform micro-bubbles.

To reach the above objectives, several micro-channels and bubble dispensers need to be fabricated and a micron-resolution particle image velocimetry system needs to be built to obtain the flow structure in micro-scale.

1.3 Research Overview

Chapter 2 presents the flow characteristics of liquid flow in straight and serpentine micro-channels including the friction factor and bend loss coefficient. The entrance effect and bend effect are discussed. This chapter can also refer to Xiong R. and Chung J.N., “Flow characteristics of water in straight and serpentine micro-channels with miter bends”, *Experimental Thermal and Fluid Science*, Vol . 31(7), pp. 805-812, 2007.

Chapter 3 describes an in-house micron-resolution particle image velocimetry system (Micro-PIV) used to measure the velocity profile in microscale and discusses the flow structure

around the bend in a serpentine micro-channel. This work has been submitted as Xiong R. and Chung J.N., “Effects of miter bend on pressure drop and flow structure in microfluidic channels”, *International Journal of Heat and Mass Transfer*, 2007.

Chapter 4 presents an experimental study of two-phase flow features in straight micro-channels including flow patterns, flow map, time-averaged void fraction and two-phase frictional pressure drop. This chapter can also refer to Xiong R. and Chung J.N., “An experimental study of the size effect on adiabatic gas-liquid two-phase flow patterns and void fraction in micro-channels”, *Physics of Fluids*, Vol. 19(3), 033301, 2007.

Chapter 5 describes a simple co-flowing micro-bubble dispenser which can be used in a lab-on-a-chip system. A VOF model is used to predict the bubble motion. Bubble size, bubble distribution, bubble frequency, and effects of viscosity and surface tension have been investigated in details. This chapter can also refer to Xiong R. and Chung J.N., “Formation of bubbles in a simple co-flowing micro-channel”, *Journal of Micromechanics and Microengineering*, Vol. 17(5), pp. 1002-1011, 2007.

Chapter 6 concludes the research with a summary of the overall work and suggests future work.

CHAPTER 2 ENTRANCE FLOW AND BEND EFFECT

Flow characteristics of pressure-driven de-ionized water were investigated in straight and serpentine micro-channels with miter bends. The micro-channels had rectangular cross-sections with hydraulic diameters of 0.209 mm, 0.412 mm and 0.622 mm. To evaluate bend loss coefficient in the serpentine micro-channel and micro-scale size effect on it, the additional pressure drop due to the miter bend must be obtained. This additional pressure drop can be achieved by subtracting the frictional pressure drop in the straight micro-channel from the total pressure drop in the serpentine micro-channel. Since currently there still has a debate on the relationship between the friction factor and Re number in the straight micro-channel, the frictional pressure drop had to be obtained experimentally here. Three groups of micro-channels were fabricated to remove the inlet and outlet losses. The experimental results show that after considering the measurement uncertainties the experimental Poiseuille number can be well predicted by the conventional laminar incompressible flow theory when Re number is less than some value around 1500, the discrepancy observed by the former researchers can be attributed to not accounting for the additional pressure drop in the entrance region. The onset of transition to turbulence might be at 1500-1700. For serpentine micro-channels, the additional pressure drop can be divided into two regions. One is $Re < 100$. It's very small since no circulation exists. The other one is Re larger than some value in 100-200. At this time the circulation appears and develops at the inner and outer wall of the bend. The additional pressure drop increases sharply with Re number. The bend loss coefficient was observed to decrease and tend to be a constant with decreasing Re number. It's found to be larger than the predicted value for macro-channel turbulent flow and related with the channel size when flow separation appears, namely $Re > 100-200$.

2.1 Introduction and Background

In recent years, the proliferation of MEMS and micro-fluidic devices has resulted in the use of micro-channels in many applications including propulsion and power generation of micro air vehicles, micro-scaled cooling systems of electronic devices, micro satellites, etc. Because of the wide range of uses for micro-channels, it is important to be able to well predict their behavior which requires a good knowledge of flow characteristics in straight and serpentine micro-channels (Ho and Tai 1998).

Flow characteristics in circular and non-circular macro-ducts with curved bends have been extensively studied (Humphrey et al. 1981; Berger et al. 1983; Bradshaw et al. 1987) in the past years. However, there were limited literatures on single phase flow characteristics in the channels with miter bends in the past. Streeter (1961) reported the bend loss coefficient for miter bend was taken to be around 1.1 for engineering applications, which was usually for turbulent flow. Yamashita et al. (1984, 1986) and Kushida et al. (1985) studied three-dimensional flow and heat transfer in miter-bend experimentally and numerically. They found a decreasing trend of the bend loss coefficient with Re number in laminar and turbulent flow region and analyzed the effects of Re number and aspect ratio on the flow structures. Though significant attention has been paid to the flow in macro-systems with bends, research on flow characteristics in micro-systems with bends has recently been started. In most practical applications the micro-channels are not straight due to required turns and sometimes it is complicated and expensive to keep the micro-channel straight. To minimize the pressure losses in the flow through the micro-channels for optimum design, flow characteristics in serpentine micro-channels with miter bends must be also well understood. Lee et al. (2001) researched on the gas flow in micro-channels having the dimensions $20 \times 1 \times 5810 \mu\text{m}^3$ with bends of miter,

curved and double-turn. They found the flow rate through the channel with the miter bend was the lowest at a certain inlet pressure and the largest drop was found in the miter bend with the lowest flow rate. They also found the secondary flow could develop in micro-channels, contrary to expectations. Maharudrayya et al. (2004) studied the pressure losses and flow structures of laminar flow through serpentine channels with miter bends by a CFD code but they didn't consider the micro-scale effect. After literature review, it can be seen that the experimental work of liquid flow in serpentine micro-channels with miter bends and the micro-scale size effect on flow characteristics have never been reported before.

As we know, the additional pressure loss due to the miter bend in serpentine channels was usually related with the flow separation and reattachment around the bend. To evaluate the bend loss coefficient, the additional pressure drop must be achieved. It can be calculated by subtracting the frictional pressure drop of straight micro-channels from the total serpentine micro-channel pressure drop. Hence, the issue of frictional pressure drop in straight micro-channels was involved in this work too.

For recent 15 years, many scientists have published numerous papers on the flow characteristics in straight micro-channels. Some of them found flow characteristics in the straight micro-channel were quite different with those predicted by the conventional laminar flow theory. One of the important flow performances was the relationship between the friction factor and Re number. For liquid flow in straight micro-channels, an increase of friction factor with Re number under certain conditions was found by the scientists including Wu and Little (1983), Peng and Peterson (1996), Mala and Li (1999), Papautsky et al. (1999), Qu et al. (2000), Pfund et al. (2000), and Li et al. (2003). Wu and Little's (1983) friction factor measurements appear to correlate with surface roughness, as the results agreed well with theory for smooth channels, but

the agreement decreased as the roughness increased. In an effort to understand the influence of geometrical parameters (specifically, hydraulic diameter and aspect ratio) on flow resistance, Peng et al. (1994) considered water flows in rectangular machined steel grooves enclosed with a fiberglass cover. A large range of Re were obtained (50 to 4000), and a geometrical dependence was observed. For the most part, the friction factor increased with increasing H/W and also with increasing D_h (holding H/W constant). Nonlinear trends between pressure drop and flow rate were observed for Re as low as 300 by Mala and Li (1999), specially for water flowing through a 0.13mm diameter stainless steel micro-tube. At small Re number ($Re < 100$) the measured friction factors were consistently higher in stainless steel and fused silica micro-tubes. Measured flow friction for trapezoidal channels was 8 to 38% higher than macroscale predictions for the range of parameters studied by Qu et al. (2000), and a dependence on D_h and Re was also observed. However, there were some other scientists finding general agreement with theoretical macroscale prediction for friction factor including Flockhart and Dhariwal (1998), Jiang et al. (1995), Sharp et al. (2000) and Wilding et al. (1994), Xu et al. (2000), Judy et al. (2002), Wu and Cheng (2003), Hetsroni et al. (2005), and Kohl et al. (2005). Jiang et al. (1995) got a linear relationship between flow rate and pressure drop in micro-channels with various cross-sectional shapes. In the circular case, the friction factor matched theoretical predictions within 10%-20%. Wilding et al. (1994) found the result for water flowing in silicon micro-machined channels agreed well with theory for at least the lower Re number (Re around 17 to 126) tested. Flockhart and Dhariwal (1998) found a good agreement between the numerical calculations for flow in trapezoidal channels and the experimental results for $Re < 600$. Sharp et al. (2000) found the microscale measurements of the friction factor generally agree with the macroscale laminar theory to within $\pm 2\%$ experimental error over all Re numbers up to transition (around $50 < Re < 2000$), for water flowing

through circular fused silica micro-channels with hydraulic diameter 0.075 to 0.242 mm. This group attributed the deviation from the theoretical prediction in the previous literatures to the size and measurement uncertainties. Hence, the relationship between the friction factor and Re number in straight micro-channels is not clear yet. The frictional pressure drop in straight micro-channels can't be calculated by a universal formulation and need to be achieved experimentally here.

In our research, three groups of micro-channels were fabricated. Each group has three micro-channels with the same size: straight long, straight short and single serpentine with miter bends. The straight long and straight short micro-channels were used to achieve the reliable frictional pressure drop in straight micro-channels, and the serpentine micro-channels were used to get the additional pressure drop due to the miter bend. The main objective of this study is to achieve this additional pressure drop and bend loss coefficient to evaluate flow characteristics in serpentine micro-channels, and compare it with the bend loss coefficient in macro-channels. The Poiseuille number for straight micro-channels can also be achieved experimentally and compared with the previous conclusions.

2.2 Experimental Setup

2.2.1 Micro-Channels Fabrication

Fig. 2-1 a) to d) shows the photographs of straight and serpentine micro-channels and schematic of the straight micro-channel used in this work. The micro-channel was laser etched in a silicon plate and then a Pyrex thin cover glass plate was anodically bonded on the top of the plate. The micro-channel plates have two dimensions of $30 \times 12 \times 2 \text{ mm}^3$ (straight long and serpentine) and $11 \times 12 \times 2 \text{ mm}^3$ (straight short). Two small connection tubes which can be inserted into the inlet and outlet assembly were connected with the small reservoirs. Each of the

serpentine micro-channels had five straight micro-channels with the same size and eight miter bends. A microscope (Olympus BX50), a 10× objective lens and a CCD camera with pixel size 6.45 μm were used to measure the dimensions of the micro-channels' rectangular cross-sections, which were listed in Table 2-1.

2.2.2 Apparatus

Fig. 2-2 shows schematic and 3-D assembly drawing of the experimental apparatus used to investigate the pressure-driven de-ionized water flow in straight and serpentine micro-channels. It includes a syringe infusion pump (Cole-Parmer Instrument), 60ml syringe (Mcmaster), micro-filter (Swagelok), pressure transducers (Kavlico), straight and serpentine micro-channel test sections and computerized data acquisition system. The de-ionized water at the flow rate from 0.1ml/min to 70ml/min, which can be set on the panel of the infusion pump with an accuracy of $\pm 0.5\%$, was driven to the micro-channel test section. The 2 μm micro-filter can remove any particles or bubbles which may block the micro-channel before the flow enters into the test section. Owing to the unavailability of appropriate internal pressure sensors which would allow in situ measurements, two pressure transducers with $\pm 0.5\%$ FS accuracy were installed at the inlet and outlet of the micro-channel to measure the upstream and downstream pressure and then sent to the data acquisition system. To get the accurate pressure at the upstream, two pressure transducers with different measurement range were used. The one with large measurement range (0-150PSI) was used for smaller micro-channels/larger flow rates, and the other one with small range (0-15PSI) were used for larger micro-channels/smaller flow rates. The data started recording when the pressures didn't change heavily for some time, which can be considered as steady state. The digital pressure output signals (0.5V-4.5V) were collected by an A/D data acquisition board (Measurement Computing PCI-DAS6034). This board has 16 single

ended or 8 differential channels, 16 bits resolution and the maximum sampling rate can be 200 KS/s. For the signal range of $\pm 5V$, the absolute accuracy is ± 10.9 LSB. A Labview program can read the signals from the board, show the pressure data in real time and save them to a data file. The test sections were placed horizontally, and all experiments were conducted at room temperature. Since the pressure measurements were made between the inlet and outlet, which is beyond the actual length of the micro-channel, there should be contraction and expansion losses in pressure drop from the inlet to micro-channel and micro-channel to the outlet. In our work, the pressure drops for the short and long straight micro-channels were measured separately. The short micro-channel has the entrance effect while the long micro-channel has the entrance effect and the friction effect, so the difference of these two pressure drops can be considered as the pressure drop due to the straight friction factor. Besides these two effects, the serpentine micro-channel has one more effect, bend effect. This effect is introduced by the flow separation around the corner and will be evaluated individually at the late section.

2.3 Data Reduction and Analysis

For a laminar flow in a macro-scale rectangular channel, the length of the developing flow in the entrance region can be estimated by the following equation given by Shah and London (1978):

$$L_d = (0.06 + 0.07\alpha - 0.04\alpha^2) \text{Re } D_h \quad (2-1)$$

Table 2-2 shows the minimum and maximum L_d/D_h for the flow rate range in our experiment and the L/D_h for the current short and long channels. It is clear that for a substantial number of cases, the flows are not fully developed under the current experimental conditions. The follow addresses the estimation of the friction factor for both entrance and fully developed flows.

For a fully developed laminar flow in a macro-scale rectangular channel with an aspect ratio α , Shah and London (1978) used a power series for the friction factor and fitted the coefficients using their experimental data as below:

$$(f \text{ Re})_{fd} = 96(1 - 1.3553\alpha + 1.9467\alpha^2 - 1.7012\alpha^3 + 0.9564\alpha^4 - 0.2537\alpha^5) \quad (2-2)$$

This empirical equation can approximate the two-dimensional theoretical exact solution (Nguyen and Wereley 2006) for the fully developed friction factor with an error less than 0.05%. For the current micro-channels, the aspect ratio range is from 0.9 to 0.97, so the corresponding theoretical Poiseuille numbers $(f\text{Re})_{fd}$ for the fully developed flow are around 57. However, the current micro-channels may not be long enough for the flow to become fully developed under laminar flow conditions. Actually in many practical applications, flows generally can not reach the fully developed state in micro-channels as they are relatively short due to space limitations in micro-systems.

For a developing flow, its pressure drop is higher than the fully developed flow. As a result, the pressure drop from the inlet of the channel to a downstream location x in the entrance region is the sum of the fully developed pressure drop and the pressure drop defect given by the equation below (Kakac et al. 1987):

$$\Delta P_{dev} = \left[(f \text{ Re})_{fd} x^+ + K(x^+) \right] \frac{\rho U^2}{2} \quad (2-3)$$

$$x^+ = \frac{x}{\text{Re} \cdot D_h} \quad (2-4)$$

where $K(x^+)$ is the pressure drop defect given by:

$$K(x^+) = \left[f_{app} \text{Re} - (f \text{ Re})_{fd} \right] x^+ \quad (2-5)$$

$$f_{app} \text{Re} = 4 \left\{ \frac{3.44}{(x^+)^{0.5}} + \frac{K(\infty)/(4x^+) + (f \text{Re})_{fd}/4 - 3.44/(x^+)^{0.5}}{1 + B(x^+)^{-2}} \right\} \quad (2-6)$$

where f_{app} is the apparent friction factor and Eq. (2-6) is given in Kalkac et al. (1987). According to White (1991), the constant B in Eq. (2.6) is equal to 2.93×10^{-4} . As plotted in Figure 2-3, the pressure drop defect $K(x^+)$ for the current micro-channels begins at the value of 0 for $x^+ = 0$ and increases asymptotically to the fully developed constant value $K(\infty)$ which has a dependence upon the channel aspect ratio for rectangular channels as suggested by Shah and London (1978).

$$K(\infty) = 0.6796 + 1.2197\alpha + 3.3089\alpha^2 - 9.5921\alpha^3 + 8.9089\alpha^4 - 2.9959\alpha^5 \quad (2-7)$$

Eq. (2-7) determines the fully developed $K(\infty)$ for a rectangular channel with an uncertainty of 0.04%. So the pressure drop for the straight short, ΔP_{sh} , and straight long channel, ΔP_l , can be expressed as:

$$\Delta P_{sh} = \Delta P_{io} + \Delta P_{dev}(x = L_{sh}) \quad (2-8)$$

$$\Delta P_l = \Delta P_{io} + \Delta P_{dev}(x = L_l) \quad (2-9)$$

where ΔP_{io} is the inlet and outlet assembly losses due to changes in tubing diameter, tees and elbows as indicated in Figure 2-1(e). Straight short and straight long micro-channels have the same channel size but different channel length.

Since the inlet and outlet pressure losses are proportional to U^2 , the inlet and outlet losses are the same for both lengths of the channels under a given Re number because that both have two ends placed in the same inlet and outlet assembly. ΔP_{sh} and ΔP_l are the measured pressure drops for the straight short and straight long channels, respectively. Hence, the experimental friction factor that takes the entrance effect into consideration is estimated by the following equation:

$$f_{\text{exp}} = \left\{ \frac{\Delta P_l - \Delta P_{sh}}{\rho U^2 / 2} - [K(L_l) - K(L_{sh})] \right\} \frac{D_h}{L_l - L_{sh}} \quad (2-10)$$

For the serpentine micro-channels, the measure pressure drop can be expressed as:

$$\Delta P_s = \Delta P_{io} + \Delta P_{dev}(x = L_s) + N \cdot \Delta P_b \quad (2-11)$$

where ΔP_s is the measured pressure drop for the serpentine channel and ΔP_b is the additional pressure drop due to the miter bend. N is the number of miter bends. So ΔP_b and the bend loss coefficient, K_b , can be written as:

$$\Delta P_b = \frac{\frac{\Delta P_s - \Delta P_l}{\rho U^2 / 2} - \left[\left\{ \frac{\Delta P_l - \Delta P_{sh}}{\rho U^2 / 2} - [K(L_l) - K(L_{sh})] \right\} \frac{L_s - L_l}{L_l - L_{sh}} + K(L_s) - K(L_l) \right]}{N / \frac{\rho U^2}{2}} \quad (2-12)$$

$$K_b = \frac{\frac{\Delta P_s - \Delta P_l}{\rho U^2 / 2} - \left[\left\{ \frac{\Delta P_l - \Delta P_{sh}}{\rho U^2 / 2} - [K(L_l) - K(L_{sh})] \right\} \frac{L_s - L_l}{L_l - L_{sh}} + K(L_s) - K(L_l) \right]}{N} \quad (2-13)$$

According to the error propagation analysis, the uncertainty of the friction factor and bend loss coefficient can be expressed as:

$$\frac{\delta(f \text{ Re})}{f \text{ Re}} = \left(\left[2 \frac{\delta D_h}{D_h} \right]^2 + \left[\frac{\delta A}{A} \right]^2 + \left[\frac{\delta Q}{Q} \right]^2 + \left[\frac{\delta(\Delta P / \Delta L)}{\Delta P / \Delta L} \right]^2 \right)^{1/2} \quad (2-14)$$

$$\frac{\delta K_b}{K_b} = \left(\left[2 \frac{\delta A}{A} \right]^2 + \left[2 \frac{\delta Q}{Q} \right]^2 + \left[\frac{\delta(\Delta P_b)}{\Delta P_b} \right]^2 \right)^{1/2} \quad (2-15)$$

The uncertainty range of the friction factor and bend loss coefficient can be calculated to be

$\pm 10.2\%$ – $\pm 15.1\%$ and $\pm 12.3\%$ – $\pm 16.1\%$.

2.4 Results and Discussion

2.4.1 Friction Factor

Fig. 2-4 shows the comparison between the experimental pressure gradients without removing the entrance effect, $(\Delta P_l - \Delta P_{sh}) / (L_l - L_{sh})$, and theoretical results for the current micro-channels. The dot lines represent the pressure gradients predicted by the 2-D conventional laminar incompressible flow theory, which shows a linear relationship with Re number theoretically. However, as the Re number increases, the measured pressure gradients shows a non-linear relationship with Re number. Some former researchers attribute it to the early transition to turbulence at $Re=700$. However, from Fig. 2-5, we can conclude it doesn't result from the early transition to turbulence but may from not accounting for additional pressure drop in the entrance region of the channel.

Fig. 2-5 shows the comparison between the experimental friction factor calculated by Eq. (2-10) and theoretical results predicted by Eq. (2-2). The solid line represents the predicted friction factor for fully developed flow, and the vertical bars denote the measurement uncertainty. From Fig. 2-5, we can see after the experimental uncertainties are considered, the experimental results show agreement with standard laminar incompressible flow predictions when $Re < 1500$. It's believed that the consistent offset observed by the previous researchers is the result of unaccounted for bias in experimental setups. When Re equals to 1500-1700, fRe begins to deviate from the theoretical value which may suggest the transition to turbulence.

2.4.2 Bend Loss Coefficient

For laminar flow, the additional pressure drop is related with the flow separation which need energy to be maintained and results in an additional pressure drop not associated with frictional losses. As we know, in micro-channels, the flow usually keeps in laminar flow region, so the flow pattern along the miter bend affects the additional pressure drop pretty much.

Maharudrayya et al. (2004) used CFD simulation and obtained the flow pattern along a miter bend at different Re numbers. When $Re = 100$, there are no eddies around the inner and outer wall. While $Re = 210$, significant recirculation at the inner and outer wall appears. The size and intensity of both vortices increase with increasing Re number.

Figure 2-6 shows the experimental additional pressure drop under different Re numbers. It can be divided into two regions. One is $Re < 100$. There is no eddies and the additional pressure drop is very small for all of the channels. The other one is the circulation appears on the inner and outer wall and develops with increasing Re number. The critical Re number is in the range 100-200. At this time the additional pressure drop increases sharply. The experimental results also show the additional pressure drop increases with decreasing hydraulic diameters. From Fig. 2-6, the additional pressure drop of the micro-channel with hydraulic diameter 0.209 mm is around 0.5atm when Re number reaches around 850, which is approximately equal to the frictional pressure drop of the same size straight micro-channel with 23.7 mm length, 101% of the current total length. Hence, the additional pressure drop due to the miter bend is also a big source of the micro-channel pressure drop, especially for small size and short length micro-channels.

Since the pressure drop for channel 1 is pretty high, Re number can only reach around 850 and the upstream pressure will exceed the measurement range of the transducer. Here the bend loss coefficients are calculated by using Eq. (2-13) and compared at Re number from 47-2268, which is shown in Fig. 2-7. The solid line represents the bend loss coefficient of the miter bend, 1.1, reported by Streeter (1961). From Fig. 2-7, we can see bend loss coefficients of the micro-channels are all larger than 1.1. It is a similar conclusion with that of Yamashita et al. (1984), the bend loss coefficient in laminar flow region is larger than that in turbulent region.

The second characteristic is it's dependent of Re number and decreases with increasing Re number, which is also different with turbulent flow. For macro-channel turbulent flow at larger Re number, K_b almost won't change with Re number. When Re is larger than some value in 1300-1500, K_b almost keeps constant and changes in the range of $\pm 10\%$. The last characteristic is the size effect on K_b . It's larger for smaller channel when there is flow separation, namely $Re > 100-200$. After considering the measurement uncertainty, these two curves still have difference. The quantitative relationship needs more experiments and simulation to be determined.

2.5 Summary

The investigation of a pressure-driven water flow in straight micro-channels and in serpentine micro-channels with miter bends was conducted experimentally. A short straight and a long straight micro-channel with the same channel size were fabricated and used to isolate the inlet and outlet assembly extra pressure losses. The following conclusions were obtained:

- The experimental friction factors show good agreement with the classical laminar incompressible flow predictions after considering the measurement uncertainties when the Re is less than 1500. When the Re is larger than 1500, the onset of transition to turbulence may take place. For laminar flows in micro-channels, the frictional pressure drops in the developing entrance region can still be predicted by the classical macro-scale equations for developing flows. In general, the frictional pressure drop in a micro-channel can be estimated by macro-scale theories and correlations.
- In serpentine micro-channels, the additional pressure drop due to miter bends can be divided into two groups. The first group is for $Re < 100$ where there is no eddies and the additional pressure drop is very small for all of the channels. The other group is for flows with the Reynolds numbers exceeding the threshold values that are in the range of 100-300. When the Reynolds is higher than the threshold value, we found the flow separation and formation of vortices that appear on the inner and outer wall around the miter bend. These vortices increase in strength with increasing Re number that causes the bend pressure drop to increase sharply with the Re number. The experimental results also show the bend pressure drop increases with decreasing hydraulic diameters. Bend loss coefficient K_b is a function of the Re number only when $Re < 100$, a function of the Re number and channel size when $Re > 100$, and almost keeps constant and changes in the range of $\pm 10\%$ when Re is larger than some

value in 1000-1500. The trend of the experimental pressure drop is consistent with the flow structure change.

The flow structures around the serpentine micro-channel can also be achieved by a relatively new laser diagnostic technique – micron-resolution particle image velocimetry (Micro-PIV), which is present in Chapter 5 in details.

Table 2-1. Dimensions of three groups of micro-channels

Channel group No.	Width $W \pm 2\mu\text{m}$	Depth $S \pm 2\mu\text{m}$	Hydraulic Diameter D_h (mm)	Total length of the micro-channels $L \pm 0.3\text{mm}$		
				Long Channel L_l (mm)	Short Channel L_{sh} (mm)	Serpentine Channel L_s (mm)
Channel 1	213	206	0.2094	23.6	4.1	118
Channel 2	419	406	0.4124	23.5	4	117.5
Channel 3	630	615	0.6224	23.8	4.2	119

Table 2-2. Comparison of current pipe lengths with those of entrance regions.

Re	L_d/D_h	L/D_h (Straight short)			L/D_h (Straight long)		
		Channel 1	Channel 2	Channel 3	Channel 1	Channel 2	Channel 3
47	4.23	19.58	9.70	6.74	112.7	56.98	38.24
2268	204.12						

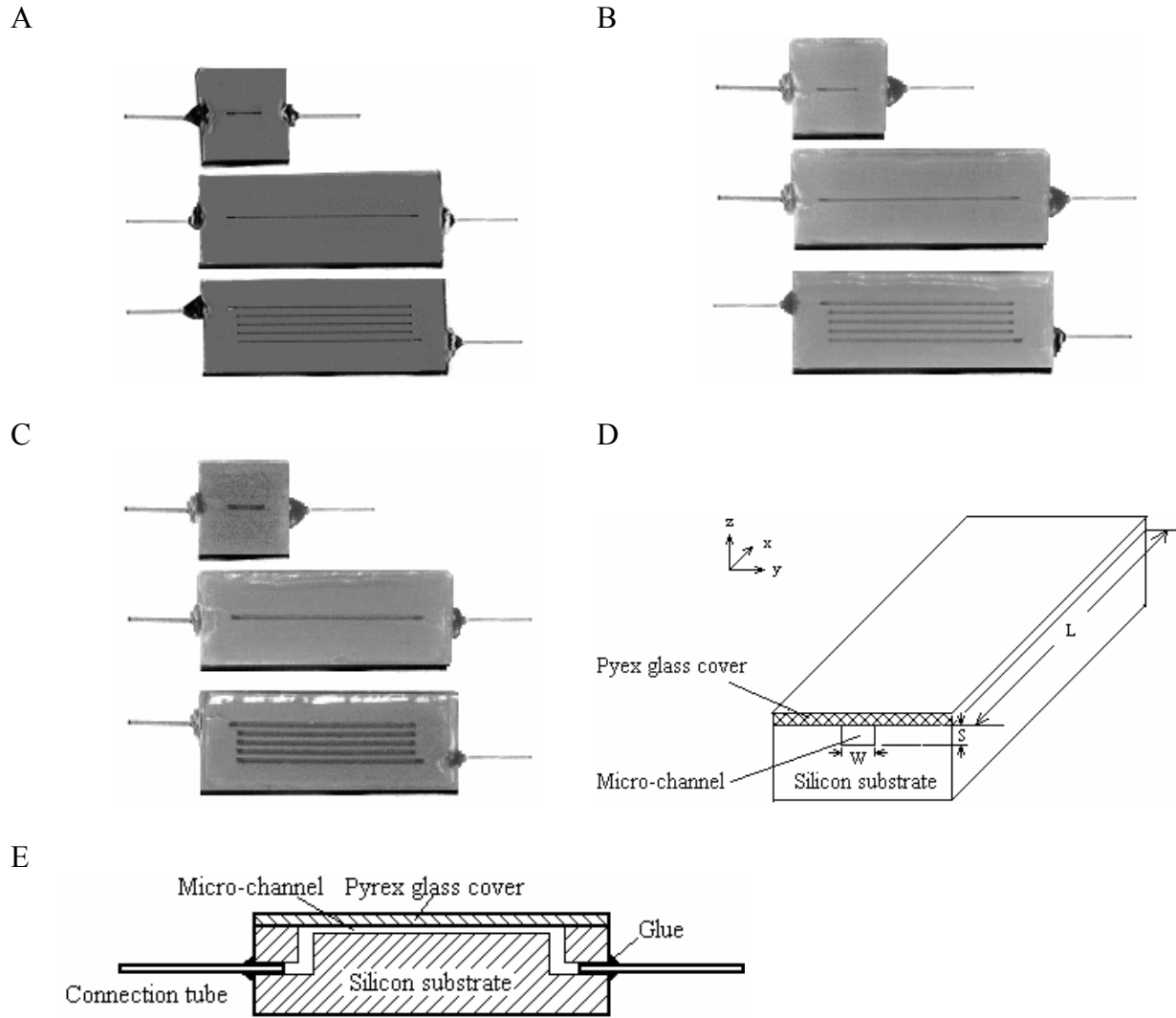


Figure 2-1. Three groups of fabricated micro-channels: A) Photograph of a group of micro-channels ($D_h = 0.209$ mm) B) $D_h = 0.412$ mm C) $D_h = 0.622$ mm D) Schematic of the straight micro-channel E) Schematic showing inlet and outlet elbows.

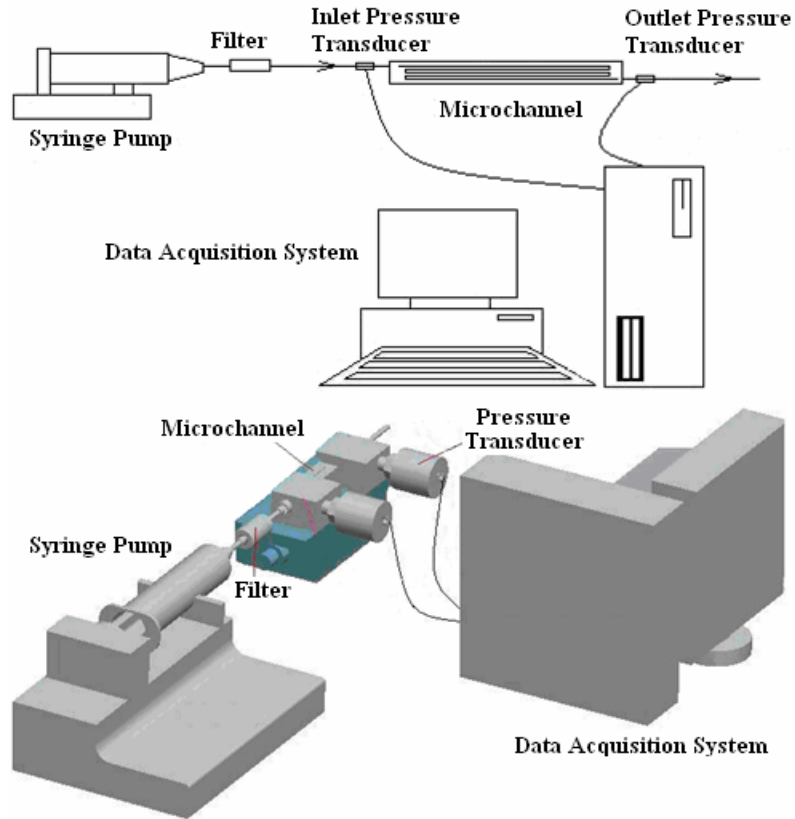


Figure 2-2. Experimental pressure drop measurement apparatus

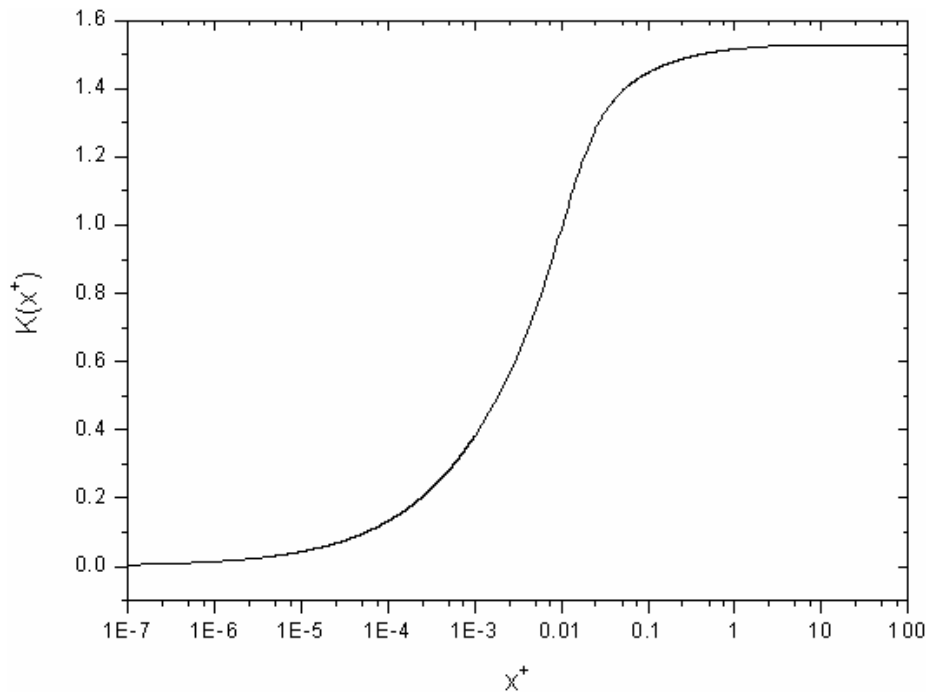


Figure 2-3. Pressure drop defect $K(x^+)$ vs x^+ .

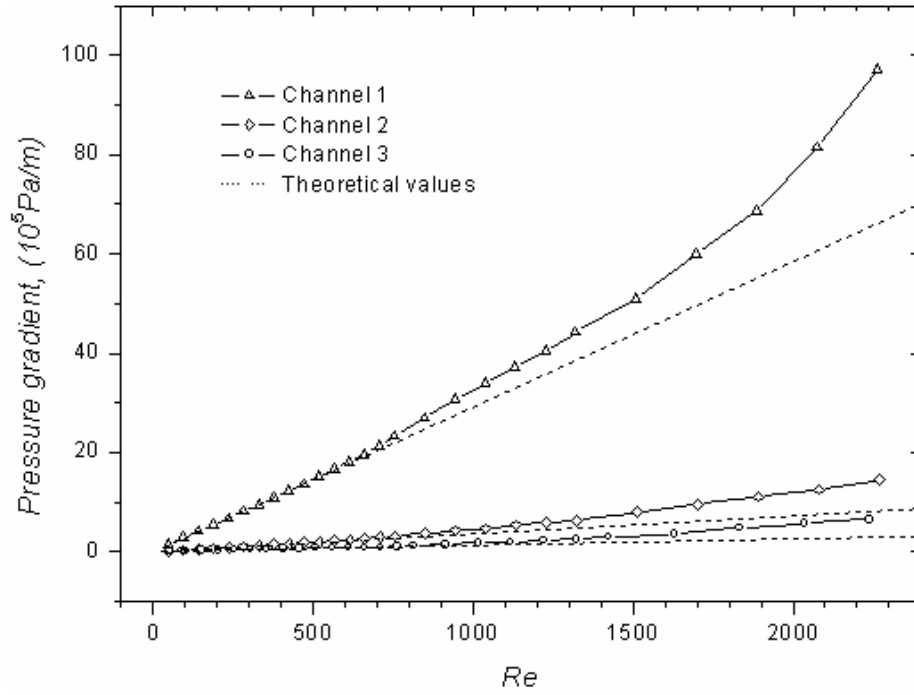


Figure 2-4. Experimental pressure gradients without removing the entrance effect $(\Delta P_T - \Delta P_{sh}) / (L_T - L_{sh})$ vs Re number.

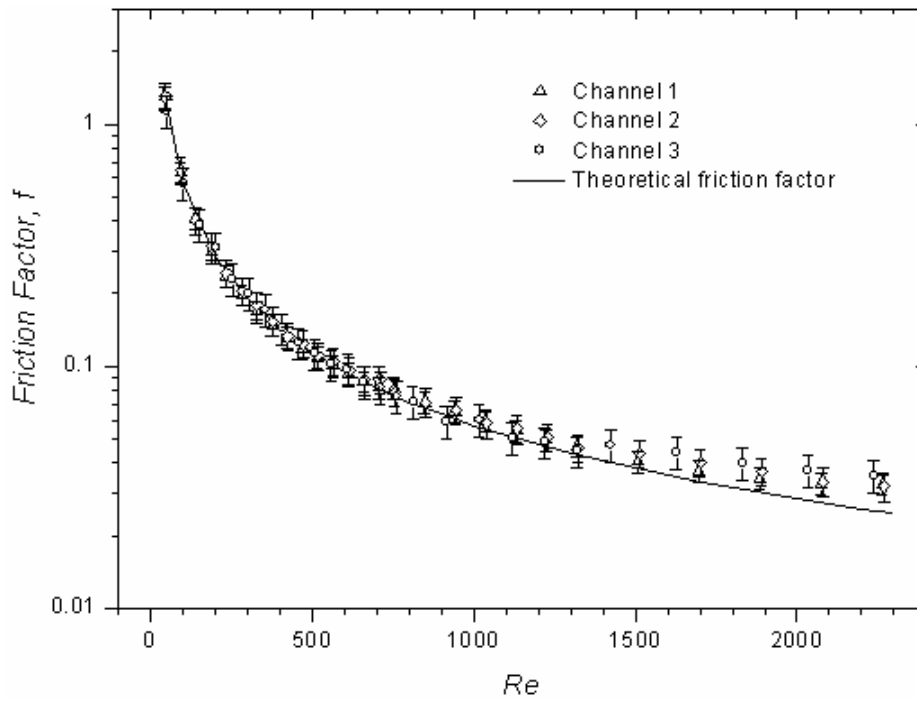


Figure 2-5. Experimental friction factor vs. Re number in straight micro-channels

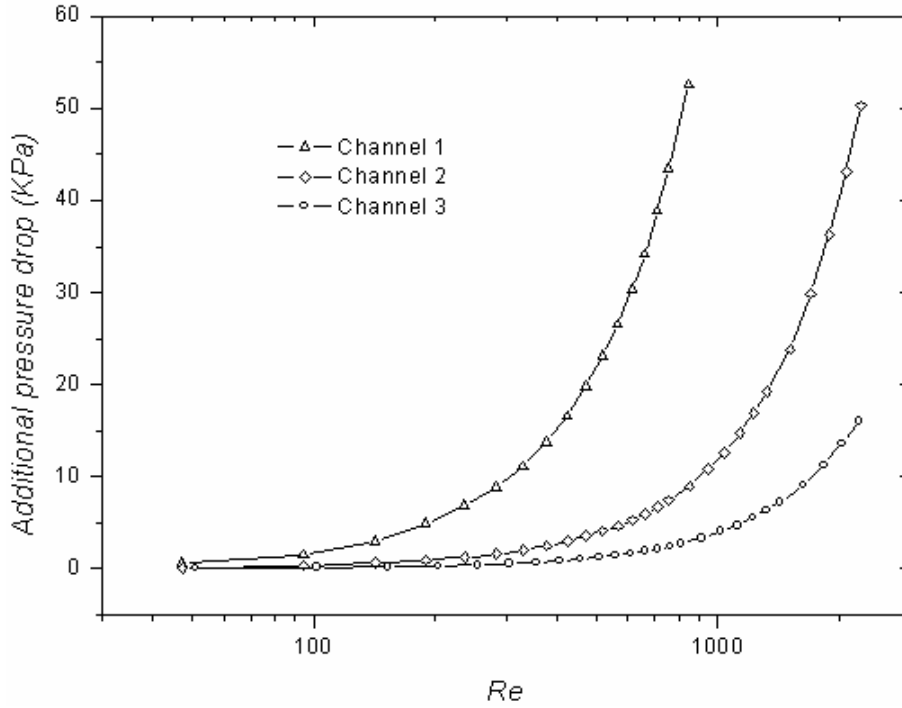


Figure 2-6. Bend additional pressure drops vs. Re number in serpentine micro-channels

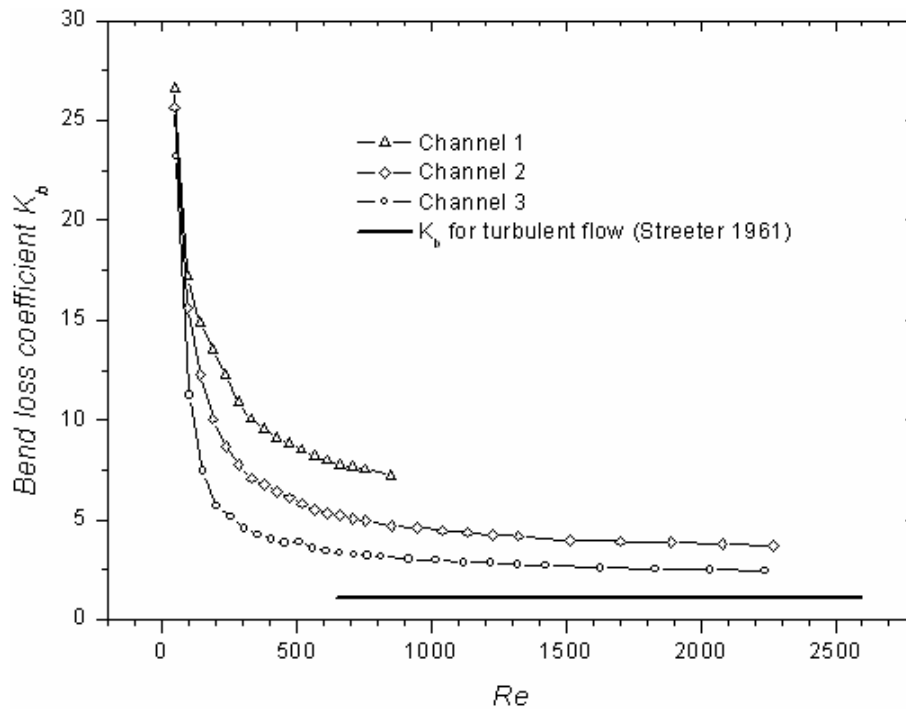


Figure 2-7. Bend loss coefficients vs Re number in serpentine micro-channels

CHAPTER 3 FLOW STRUCTURES AROUND A BEND

From chapter 3, we know the bend additional pressure drop is related to the flow structure around the bend, here a micron-resolution particle image velocimetry (micro-PIV) system was built and used to obtain the detailed velocity vector field in a serpentine micro-channel. The micro-PIV system was verified first by the velocity profile in a straight micro-channel of 0.209 mm. It was found that the vortices around the outer and inner walls of the bend do not form when $Re < 100$. Those vortices appear and continue to develop with the Re number when $Re > 100$, and the shape and size of the vortices almost remain constant when Re is larger than a value in 1000-1500. The results are compatible with those in chapter 3.

3.1 Introduction and Background

In curved channels, the centrifugal force drives the more rapid fluid toward the concave part of the curved channel while the fluid in the convex part is slowing down causing a secondary flow at a right angle to the main flow. The magnitude of the secondary flow increases with a decreasing bend radius and increasing fluid velocity. As expected, the curved channel will cause a much higher friction loss than that of the corresponding straight tube for both laminar flow and turbulent flow. In previous works, the researchers used computational method or color dye to visualize the flow structure. Here a relatively new experimental technique, microscopic particle image velocimetry (micro-PIV) was used to measure the velocity field. The micron-resolution Particle Image Velocimetry (μ PIV) system was first developed by Santiago et al. (1998) to investigate microscale fluid flow. He used an epi-fluorescent microscope with a continuous Hg-arc lamp, and a Princeton Instruments' intensified CCD camera to record the flow around a nominally 30 μ m diameter cylinder in a Hele-Shaw flow cell. A bulk velocity of 50 μ m/s was measured with a spatial resolution of 6.9 μ m \times 6.9 μ m \times 1.5 μ m, based upon the size of the first

correlation window and the depth-of-field of the microscope. Later, the system was modified by Meinhart et al. (1999) to measure higher speed flow using the pulsed laser. It is becoming one of the most versatile experimental tools in microfluidic research. Though μ PIV has evolved from conventional PIV, there are several important factors which differentiate μ PIV from conventional PIV.

One hardware difference is the method of illumination in μ PIV, i.e. volume illumination. The conventional PIV used a light sheet to illuminate a single plane of the flow with the thickness less than the depth of field of the image recording system. Volume illumination is an alternative approach, whereby the test section is illuminated by a volume of light. This illumination model may be necessary for obtaining two-dimensional measurements when optical access is limited to only one direction or in micro-scale geometries in which alignment of the light sheet is difficult. It is advantageous when one is interested in measuring flows through micro electromechanical systems for which optical access is limited to one direction and the length scale is of the order of micrometers (Meinhart et al. 2000a). The small length scales associated with microfluidic devices require that the thickness of the measurement plane should be only a few micrometers. Since it is difficult to form a light sheet that is only a few micrometers thick and virtually impossible to align such a light sheet with the optical plane, volume illumination is the only feasible illumination method for most micro-PIV applications. One shortcoming for volume illumination is it causes significant background noise and limits the particle concentration by reducing the signal to noise ratio (Gui et al. 2002; Meinhart et al. 2000b).

Image processing and advanced interrogation algorithms can be used to enhance image quality and to increase the signal-to-noise ratio. The images taken in micro-PIV are usually in

worse condition, i.e. lower signal-to-noise ratio, than those in the conventional PIV. Errors in PIV measurements can be reduced by improving the experimental conditions and by using advanced interrogation algorithms such as the average correlation method. Ensemble average correlation method is a time-averaged PIV algorithm developed by Meinhart et al. (2000b) to improve the signal to noise ratio, especially in case of the volume illumination. This algorithm can only be applied to steady or periodic flow fields. Since most typical microfluidic devices are working in steady flow conditions, the time averaged velocity field is sufficient to resolve the micro-scale flow. The central difference image correction algorithm (Wereley and Gui 2003) is a very effective and accurate method, especially for making measurements in regions of high velocity gradient. This method is a combination of the central difference interrogation algorithm developed by Wereley and Meinhart (2001), the continuous window shifting technique developed by Gui and Wereley (2002) and the modified image correction algorithm originally introduced by Huang et al. (1993). This central difference image correction method shows the significant reduction in the evaluation error, i.e. the bias and random errors, when compared to other more traditional methods.

Another important difference is the size of seed particles. Since a seed particle should be small enough compared to the dimension of the microfluidic device not to disturb the flow pattern, relatively small seed particles are required in μ PIV. However, when the particle diameter is much smaller than the wavelength of the illumination light, scattering from the particles is too weak to image them using elastic scattering, i.e. the frequency of the scattered light is the same as that of the incident light. An inelastic scattering technique such as fluorescence can be used to increase the signal-to-noise ratio by filtering the background light.

Brownian motion is another factor to be considered in μ PIV since Brownian motion becomes significant when the particle or the flow velocity is very small, and eventually causes errors in the velocity measurement and increases the uncertainty in the particle location. Brownian motion has two major effects on μ PIV measurements. One effect decreases the accuracy in estimating the particle displacement between the two light pulses, i.e. the time interval. Brownian motion also can cause errors in estimating the particle location during the illumination exposure. The latter problem can be solved readily by using pulsed lasers which reduce the exposure time so significantly (to 5 ns) that Brownian motion has no effect (Nguyen and Wereley 2002). The former error can be reduced by increasing the time interval. Though long time interval values generally have been avoided in PIV evaluation because of the larger evaluation error associated with the longer time interval, this problem can be minimized with advanced interrogation algorithms such as the central difference interrogation. Also the Brownian motion error is further reduced by a factor of $1/\sqrt{N_i}$ when N_i particle images are averaged in a single interrogation spot.

In this chapter, the main objective is to 1) build an in-house micro-PIV system and 2) achieve the flow structures under different Re numbers to explain the pressure drop data in chapter 3.

3.2 Micro-PIV System

3.2.1 Laser Beam Alignment

Two Nd:YAG laser machines(Continuum Minilite II) were used to create the illumination source. Some useful information of the laser is listed in Table 3-1. To make the two lasers illuminate approximately the same region, a laser beam alignment component is constructed to combine these two lasers in the same optical axis. Fig. 3-1 shows the top view of the optical

layout of the laser beam alignment component. A half waveplate (Newport) changes the vertical polarization of laser B to be horizontal polarization while laser A still keeps the vertical polarization. The beam merger, a dielectric polarizer (Newport), reflects the laser with vertical polarization, namely laser A and transmits the laser with horizontal polarization, namely laser B. A beam stop absorbs the light that transmits the beam merger. A linear and rotation stage A with high precision was fixed beneath the beam merger and another linear high precision positioning stage B was fixed beneath the laser B output. Rotate stage A to change the incline angle of laser A and make the intensity of the reflection beam maximum. After that, adjust stage B to make laser B merge into the optical axis of laser A. A beam expander including two spherical concave and convex lenses (Newport) expands the size of the laser beam after the beam merger. Adjusting the distance between these two lenses can change the expanded laser beam size. The reason why the spherical lenses were used here is to create volume illumination for micro-PIV measurement.

3.2.2 Timing Scheme

Since the laser beams are pulsed and the pulse width is so short, 3-5 nsec from Table 3-1, the CCD camera shutter is required to keep open to make the frame exposed during the pulse width. And one frame is required to be exposed once. Hence a timing scheme is required to externally control the two lasers and CCD camera.

To externally control the laser, turn the real panel FLASHLAMP and Q-SWITCH switch of the laser machine Minilite II from INT to EXT. It will disable the internally generated signals which respectively fire the flash lamp and open the Q-switch. At the same time, these switches let the Minilite II accept TTL signals into the FLASHLAMP TRIG IN and Q-SWITCH TRIG IN BNC ports to trigger flash lamp firing and Q-switch opening. The Q-switch delay can adjust the output pulse energy. For Minilite II, the delay of about 152 μ s yields highest energy laser pulse.

The time delay between the two lasers' firing the flash lamp is quite important and should be chose carefully since it sets the interframing time.

A specialized CCD camera (Cooke Sensicam QE), 1376 x 1040 pixels, was used to record the flow field. It uses thermo-electrical cooling to cool down to -12°C , which lowers the readout noise low to 4 e-rms so the weak fluorescent signal can be measured. The interframing time low to 500 ns make it enough to measure the flow with high Reynolds number up to 2000. To externally control the CCD camera, set the operation mode to double shutter in the software and use a coaxial cable to connect the TRIG IN BNC ports with the timing controller. The double exposure is controlled via an external TTL trigger signal from the controller.

A timing controller (Labsmith LC 880) was used to realize the timing scheme. It has 8 input and 8 output channels. It is also able to send a trigger-pulse delay from 50ns to 1370s and trigger-pulse duration from 7.7ms to 1370s with the resolution of 10 ns. A RS232 interface connects the controller with the computer to make remote control. Connect the two lasers (4 output ports) and the CCD camera (1 output ports) with the controller, and TTL trigger signals can be sent to them via some coaxial cables. Fig. 3-2 shows the timing diagram for the two lasers and CCD camera. How to program LC 880 to realize this time scheme refers to the Appendix.

When the shutter trigger signal falls, the shutter opens after a very short period. The integration time for image one will be finished some time after the trigger signal rises again and the integration time for image two starts. What we need control is to send two laser pulses by setting a proper time delay from the trigger signal to make one pulse be in the integration time of image one and the other pulse in the integration time of image two, so in each integration time the image will be exposed once, which is called double frames double shutter. The interfaming time can be shortened by sending the first pulse at the end of the image one's integration time

and the second pulse at the beginning of the image two's integration time. After testing the CCD camera, we find the minimum interframing time for our CCD camera can reach 300ns which is enough short for our experiment. Another important issue is the rising duration of the trigger signal must be long enough for the CCD to read out the two images.

3.2.3 Fluorescent Particles Image

To visualize the flow field in the micro-channel, fluorescent particles, polymer micro-spheres (Duke Scientific R500), are seeded in the flow. These micro-spheres have a measured mean diameter of $0.49\mu\text{m}$ and approximate a number of 1.5×10^{11} per mL. They also have the excitation maxima of 542 nm and the emission maxima of 612 nm with 70 nm Stokes shift. A filter cube (Olympus U-MWIG), assembled in the microscope (Olympus BX50), reflects the light with wavelengths between 520 and 550 nm, exciting TMRM (maximum excitation at 548 nm), and transmits fluorescence through a high-pass filter (565 nm). The process of taking fluorescent particles image was that the expanded laser beam was delivered into the microscope, where the filter cube directs the beams to the objective lens. The objective lens relays the light onto the micro-channel, where it illuminates the entire flow volume. Fluorescent particles in the cone of illumination absorb the illumination light, $\lambda=532\text{nm}$, and emit a distribution of red light, $\lambda=612\text{nm}$. The emitted red light can go through the filter cube and is recorded onto the CCD camera while the reflected green light from the background is filtered out by the filter cube. According to the timing scheme, the CCD camera shutter was opening when the lasers came. Hence two consecutive fluorescent particles images were recorded. Fig. 3-3 (a) and (b) show the real images and schematics of a straight micro-channel with the hydraulic diameter of $209\mu\text{m}$ and a serpentine micro-channel having a rectangular cross-section $650\mu\text{m} \times 100\mu\text{m}$ with hydraulic diameter of 0.173 mm.

3.2.4 Measurement Depth

Fig. 3-4 shows the schematic of micro-PIV used to investigate the pressure-driven de-ionized water flow in serpentine micro-channels. Fig. 3-5 and Fig. 3-6 show the photo of the system and the laser beam alignment component. Firstly the fluorescent particles were seeded into the de-ionized water flow. Two Nd:YAG lasers were directed to the same optical path by optical lenses and expanded by a beam expander made up of a concave and a convex lens. The 0.69 μm particles absorb green light ($\sim 542\text{nm}$) and emit red light ($\sim 612\text{nm}$). The emitted light is imaged through a 10 \times objectives lens (NA=0.3) and passed to the fluorescent filter cube, where the green light from background reflection is filtered out and the red fluorescence from the sub-micron particles is passed to the 0.5 \times lens and recorded on the CCD camera. With the micro-PIV technique, the depth of field is described by Meinhart et al. (2000a) as:

$$z_m = \frac{3n\lambda}{NA^2} + \frac{2.16D_p}{\tan\theta} + D_p \quad (3-1)$$

where n is the index of refraction of the immersion medium between the microfluidic device and the objective lens, λ is the wavelength of light in a vacuum, NA is the numerical aperture of the objective lens, D_p is the diameter of the PIV particle and θ is the small light collection angle. In our case, n was 1, λ was 612 nm, NA was 0.3, d was 0.69 μm and $\tan\theta$ was 0.31. Therefore, the depth of field was calculated to be 26.06 μm . The concentration of the fluorescent particles solution was prepared to ensure at least 5-10 seed particles in each interrogation volume. The necessary minimum seed density was estimated using the equation (Li et al. 2006):

$$N_p = C_v A_i (2z_m) \quad (3-2)$$

where N_p is the desired minimum number of particles in each interrogation volume; C_v is the volumetric concentration of the fluorescent particle solution; A_i is the area of each interrogation

window. The interrogation windows in current experiments measure 42 μm square. Adjacent interrogation windows were overlapped by 50%, yielding a spatial resolution of 21 μm . To achieve this spatial resolution required a volumetric particle concentration of approximately 0.0082%. This volume fraction of seed particles is small enough to neglect any two-phase effects, and the working fluid can be considered a single-phase fluid. In this work, this time delay is set to be 1-15 μs for the micro-channel flow at different Re numbers, so the particles move approximately 1/4th of an interrogation window between pulses. The interrogation windows measure 32 camera pixels square, thus the particles moves approximately 8 pixels between laser pulses. Assume that the measured velocity is accurate to within 1/5th of a pixel. It results in an experimental uncertainty of less than $\pm 2.5\%$ (Prasad et al. 1992).

3.3 System Validation

To validate the micro-PIV system, the velocity field is initially obtained at room temperature in the straight micro-channel of 0.209 mm at low Re numbers. The time delay between consecutive frames is 5ms. An interrogation window of 32 \times 32 pixels and a grid size of 16 \times 16 pixels are used. The analytical solution for the velocity profile at the PIV measurement depth can be formulated as:

$$u(y) = -\frac{W^2}{2\mu} \frac{dP}{dx} \left[\frac{y}{W} - \frac{y^2}{W^2} - \left(\frac{2}{\pi}\right)^3 \sum_{k=0}^{\infty} \frac{(-1)^k}{(2k+1)^3} \frac{\cosh\left[(2k+1)\frac{\pi z_m}{2W}\right]}{\cosh\left[(2k+1)\frac{\pi S}{2W}\right]} \cos\left[(2k+1)\frac{\pi(2y-W)}{2W}\right] \right] \quad (3-3)$$

where dp/dx is the pressure gradient, W and S are the width and depth of the micro-channel respectively. Figure 3-7(a)-(b) shows the results of PIV analysis for the square micro-channel of 0.209 mm and comparison with the theoretical profile computed from Eq. (3-3). The average discrepancy between our PIV measurements and the predicted velocities is averagely about 4%

for the center line $\pm 70\mu\text{m}$ while about 10% for the measurements closet to the wall due to the near-wall effect.

3.4 Results and Discussions

3.4.1 Flow Structures Around The Miter Bend

Figure 3-8 shows a typical image and velocity vector field generated by the micro-PIV system. The focus of the flow field in Fig. 3-8 is the effects of the 90 degree turning on the flow micro-structures around the miter bend in the serpentine micro-channel at $Re = 500$. We note that the main stream velocity increases while the flow is rounding the corner. It is also apparent that micro-structures of flow recirculation have formed around the outer corner and immediately after the inner corner (flow separation). A detailed visualization and discussion on the onset and development of induced vortices around the outer and inner corners with the Re number are given below. Fig. 3-9(a-e) shows the enlarged velocity fields at the outer corner for the Reynolds numbers ranging from 100 to 1500. Fig. 3-9(f-j) shows the enlarged velocity fields at the inner corner for the same Reynolds numbers. Fig. 3-10 shows the corresponding streamlines computed from the experimental velocity vectors. For the induced micro flow structures at the outer corner, there is basically no recirculation for $Re = 100$ and only some fluctuations in the flow adjacent to the wall due to the wall roughness are captured by the PIV. At $Re = 300$, a very small vortex located at $(x = 0.2 \text{ mm}, y = 0.95 \text{ mm})$ is seen, but its circulatory motion is not fully developed. It is clear that at $Re = 500$, the recirculation vortex is fully developed and located at $(x = 0.3 \text{ mm}, y = 1.07 \text{ mm})$. As the Reynolds number is further increased to 1000 (Fig. 3-10(d)) and then to 1500 (Fig. 3-10(e)), the locations of recirculation vortices stay at the same point and only the size and strength are increased with the Reynolds number.

For flow structures near the inner corner, the micro flow structures that form due the flow separation always start right after the sharp edge as the flow separates. Again, there is basically

no separation vortex for $Re = 100$. The separation vortex is very clear for $Re = 300$. As the Reynolds number is further increased, the size and strength of the separation vortex are also increased accordingly. However, the growth of the vortex seems saturated after $Re = 1000$ as there is no significant difference in the size between $Re = 1000$ and $Re = 1500$ but the strength continues to increase as discussed later. For $Re = 1000$, the inner corner vortex approximately occupies 20% of the width of the channel in the downstream of the bend.

In summary, micro-structured recirculation vortices are induced when the flow is making the turn in a serpentine micro-channel. These vortex structures are responsible for the bend additional pressure drops for the serpentine micro-channel as compared to a straight micro-channel. The following presents the measured pressure drops and discussions for serpentine channels.

3.4.2 Circulation Calculation

In order to further substantiate the relatively large bend pressure drops, we calculated the circulation, Γ , for every induced vortex from the velocity field given in Fig. 3-9. The circulation, Γ , that is the strength of the vortex is defined as:

$$\Gamma = \iint (\nabla \times \vec{V}) \cdot d\vec{A} \quad (3-4)$$

The results of the calculated vortex circulation are given in Table 3-2. In general, the outer vortices are three to six times stronger than the inner vortices. Figure 3-11 shows the total vortex circulations as a function of the Reynolds number. The total circulation is the sum of the absolute values of the inner and outer vortices. The similar trends between the total vortex circulation (Figure 3-11) and the bend pressure drop of $D_h = 0.209$ mm channel (Figure 3-6) serve to confirm the measured data.

3.4.3 Shear Strain

For further understanding the micro-structures of the flow, the flow shear strain rate distributions were computed based on the Eq. (3-5) and plotted in Figure 3-12.

$$\varepsilon_{.xy} = \frac{1}{2} \left(\frac{\partial u}{\partial y} + \frac{\partial v}{\partial x} \right) \quad (3-5)$$

As we examine Figure 3-12, the shear strain rates generally increase with the Reynolds number and there is an uneven distribution pattern with highest rates concentrated along the inside wall and they peak around the sharp edge. Before the vortices appear, the velocity only changes much around the bend, so we can see bright color around the bend when $Re = 100$. After the vortices appear, the velocity also changes a lot from the vortex to the main stream, so we can see the color change around the vortex structure.

3.5 Summary

A micron-resolution particle image velocimetry system has been built. The minimum interframing time can be set to 200ns which make the system has the ability to measure the velocity up to 10m/s. The flow structure in a serpentine micro-channel with miter bends was conducted experimentally. The following conclusions were obtained:

- The Micro-PIV system is verified by the flow field in the micro-channel with the hydraulic diameter of 0.209 mm.
- The flow micro structures around the bend of a serpentine micro-channel can be divided into three categories depending on the flow Reynolds number. When $Re < 100$, there is no induced flow recirculation and flow separation. When $Re > 100$, vortices and flow separation appear and further develop. The outer corner vortex develops along the wall of the channel, and the vortex center moves slightly from the upper stream to the down stream with the increasing of the Re number. The inner wall vortex due to flow separation develops immediately after the flow makes the turn. When Re is around 1000, the inner wall vortex approximately occupies 20% of the width of the channel in the downstream side of the bend. When $Re > 1000-1500$, the shape and size of the outer and inner vortices become almost constant.
- The shear strain rates generally increase with the Reynolds number and there is an uneven distribution pattern with highest rates concentrated along the inside wall and they peak

around the sharp edge. After the vortices appear, the velocity also changes a lot from the vortex to the main stream, so we can see the color change around the vortex structure.

Table 3-1. Specification of the Nd:YAG laser (Continuum Minilite II)

Parameters	Value
Wavelength	532 nm
Energy	25 mJ
Pulse width	3-5 nsec
Polarization	Vert.
Beam size	<3 mm
Divergence	<3 mradx
Repetition Rate	1-15 Hz

Table 3-2. Calculated vortex circulation

Re	Inner Wall Vortex Strength (mm^2/s)	Outer Wall Vortex Strength (mm^2/s)
100	0.082	-0.41
300	4.10	-12.47
500	10.97	-77.48
1000	28.10	-203.9
1500	97.99	-266.9

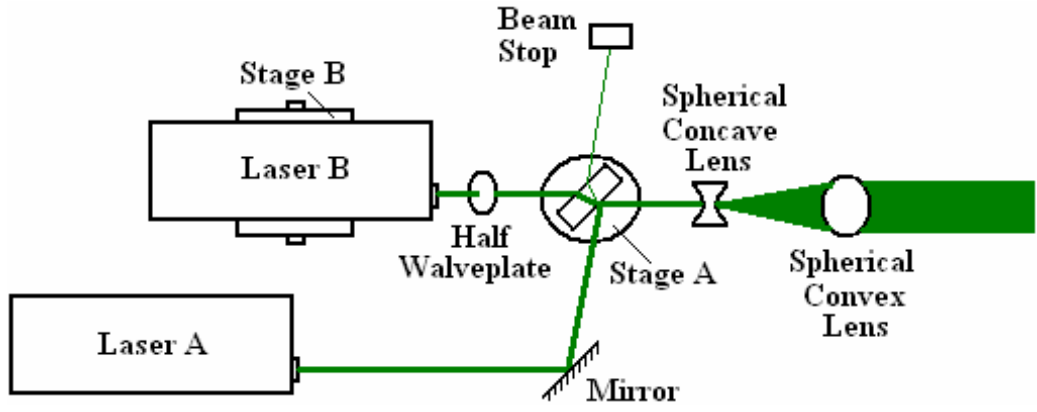


Figure 3-1. Top view of the optical layout of the laser beam alignment

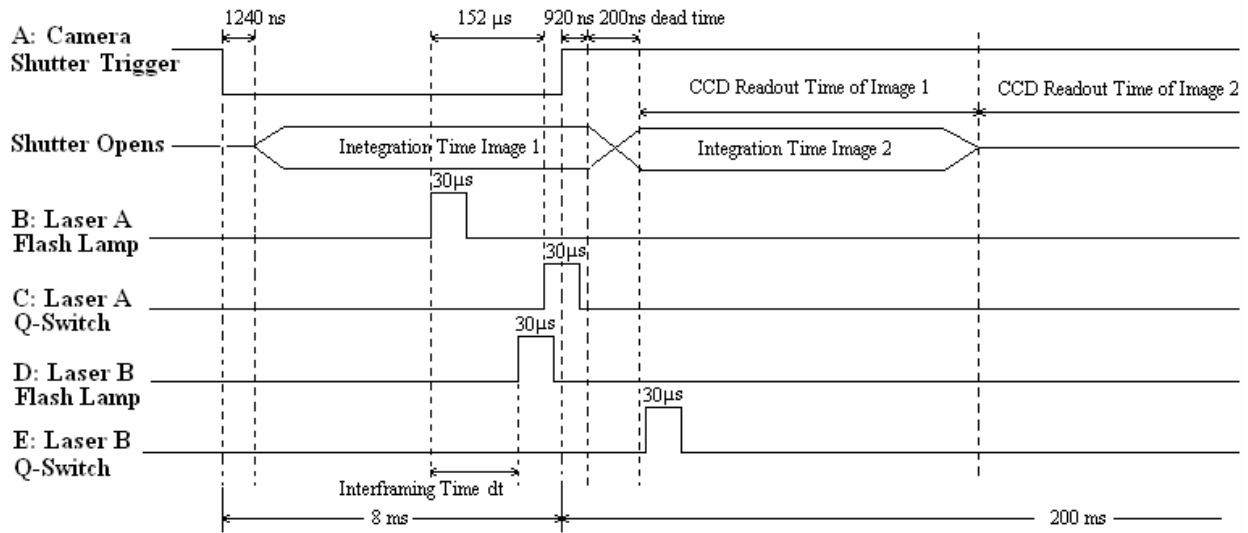


Figure 3-2. Timing diagram for the two lasers and CCD camera

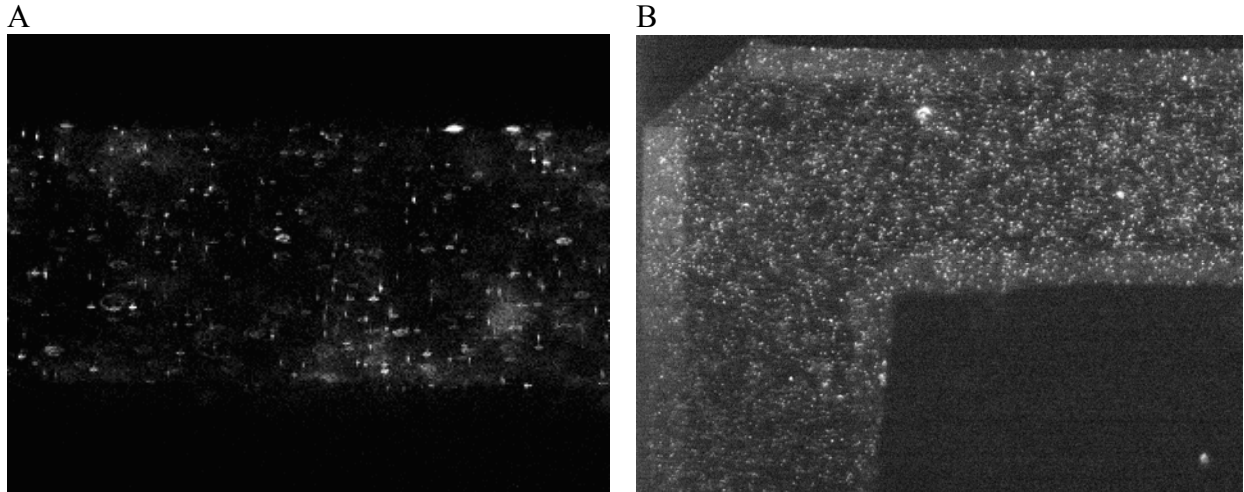


Figure 3-3. Fluorescent images at straight and serpentine micro-channels : A) A real image of the straight micro-channel with hydraulic diameter of 0.209 mm and B) the serpentine micro-channel with hydraulic diameter of 0.172 mm (a 10× objectives used; white spots are the fluorescent particles).

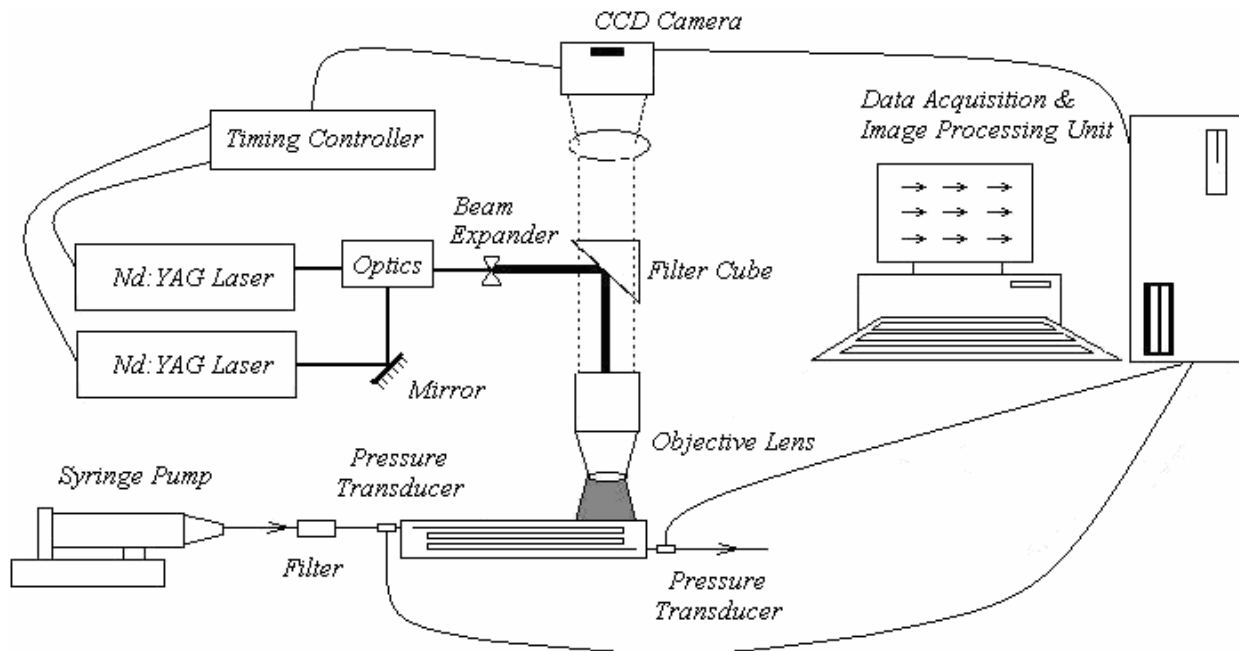


Figure 3-4. Schematic of micro-PIV system

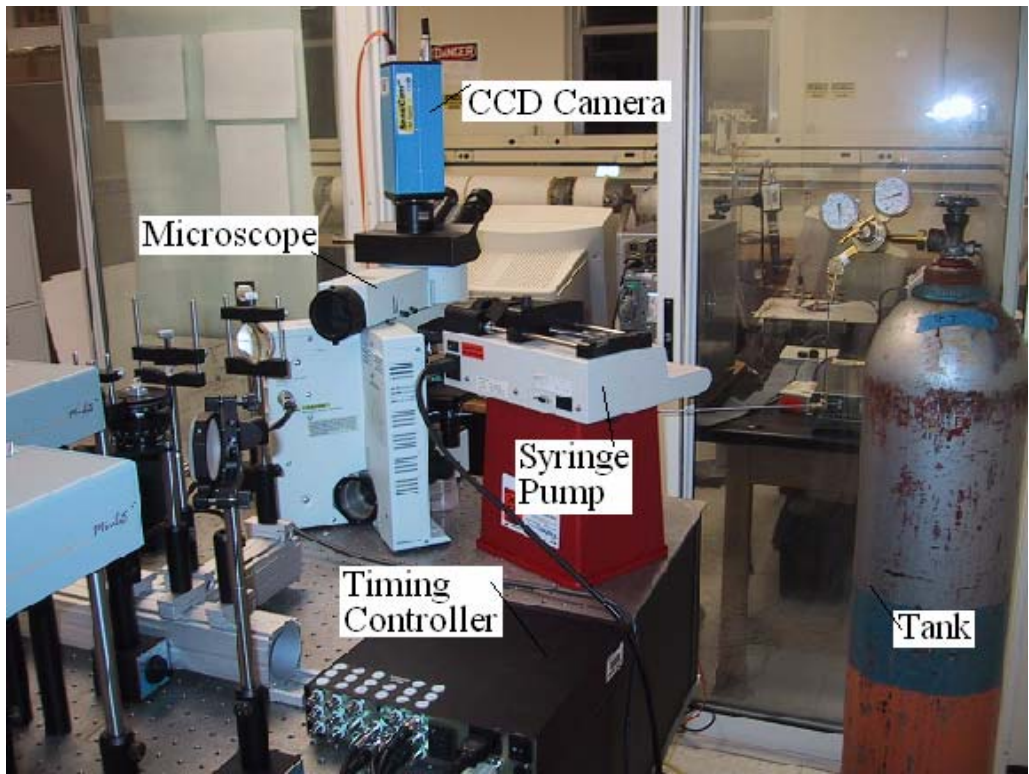


Figure 3-5. Photo of the optical subsystem

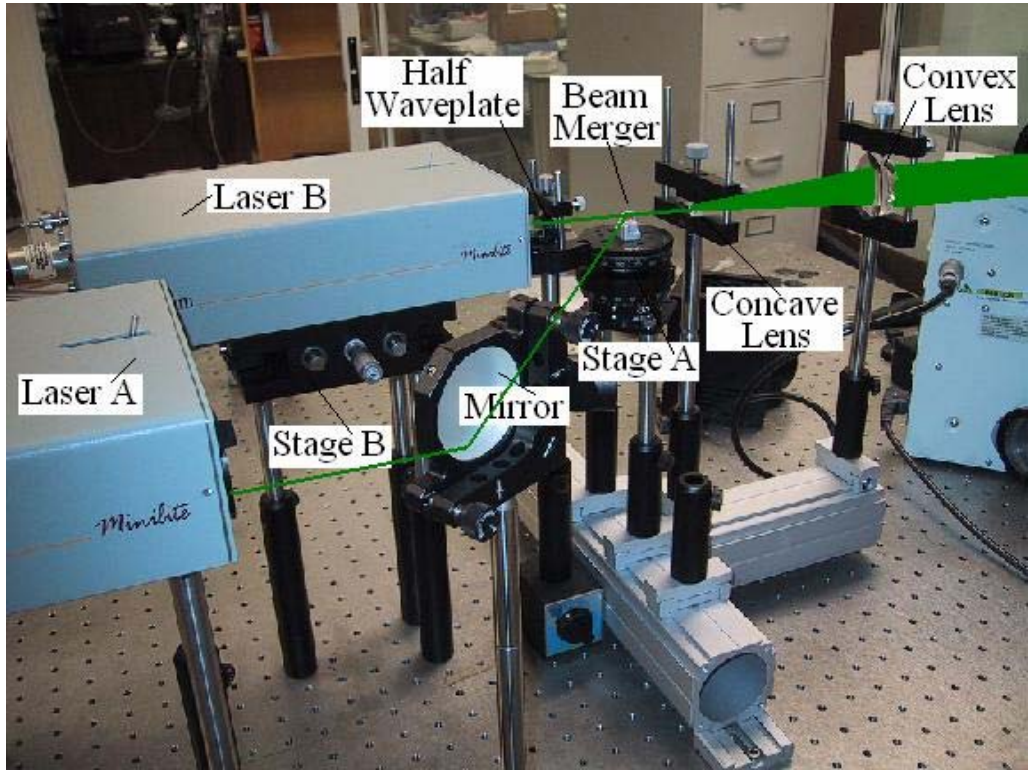
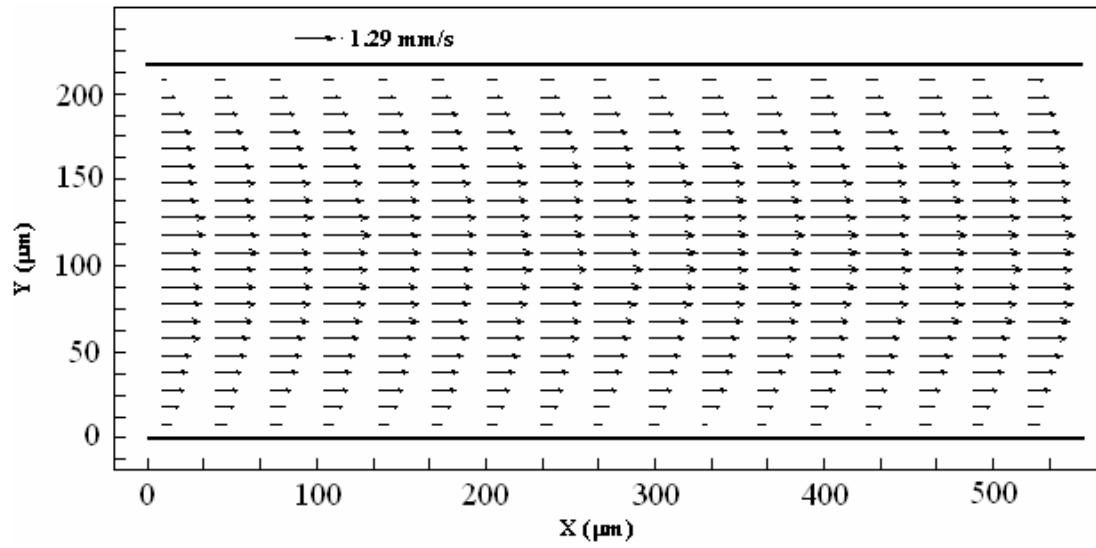


Figure 3-6. Photo of the laser beam alignment component

A



B

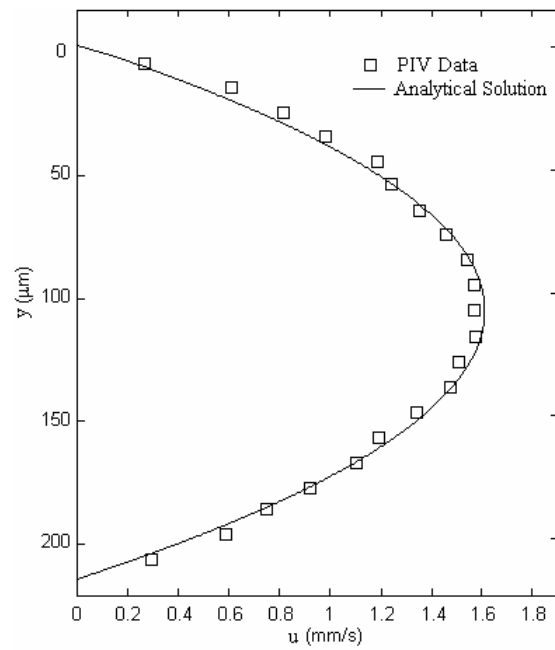


Figure 3-7. Micro-PIV results for low speed flow. A) Velocity vectors (112 pairs of images were ensemble-averaged) B) Comparison of the measurements with the theoretical profile ($Re = 0.3$).

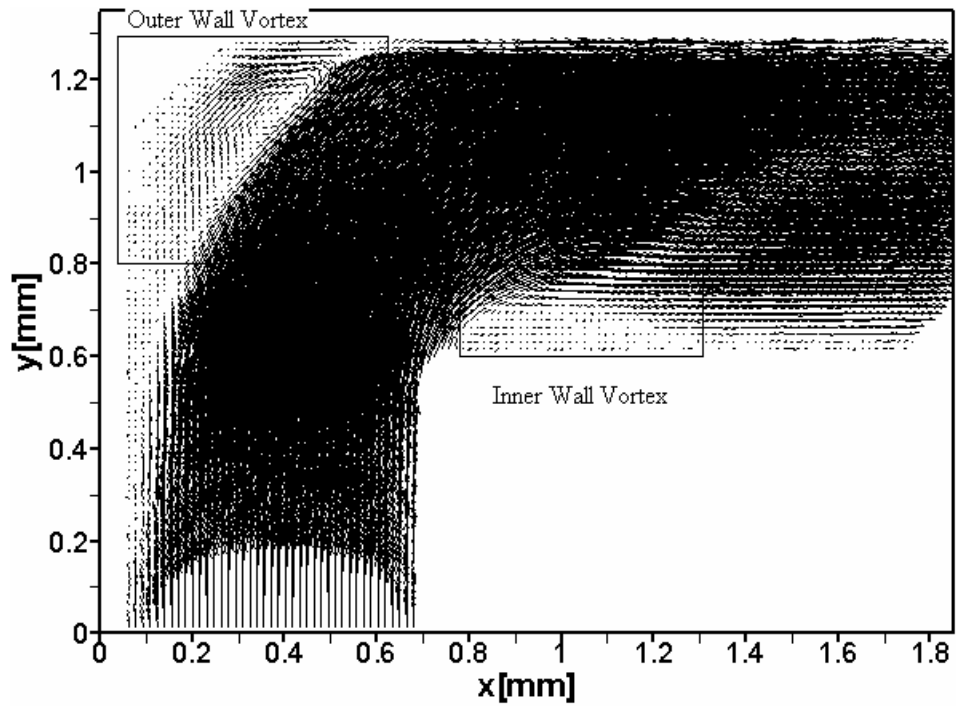


Figure 3-8. Typical velocity vector in the serpentine micro-channel at $Re = 500$.

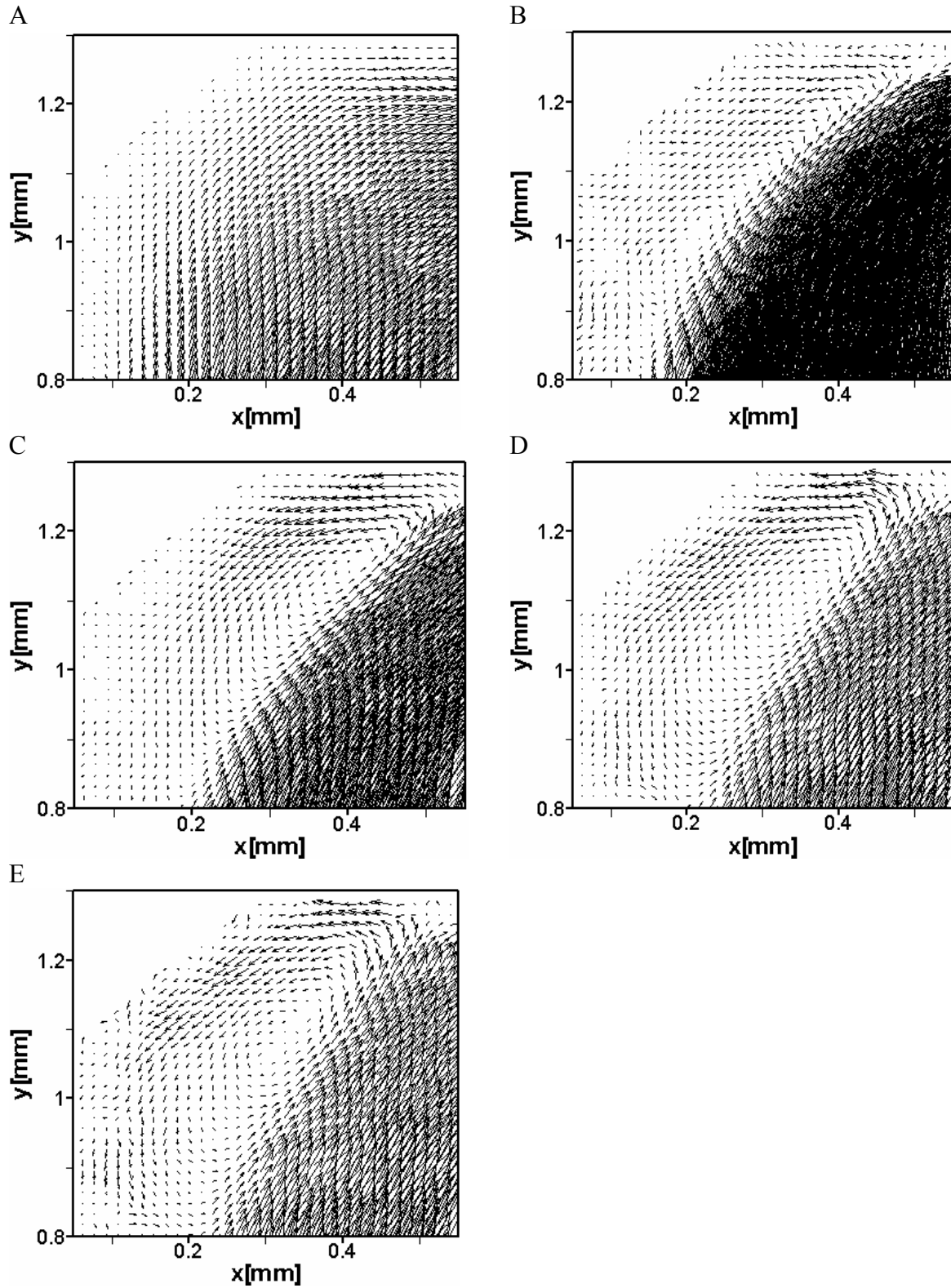
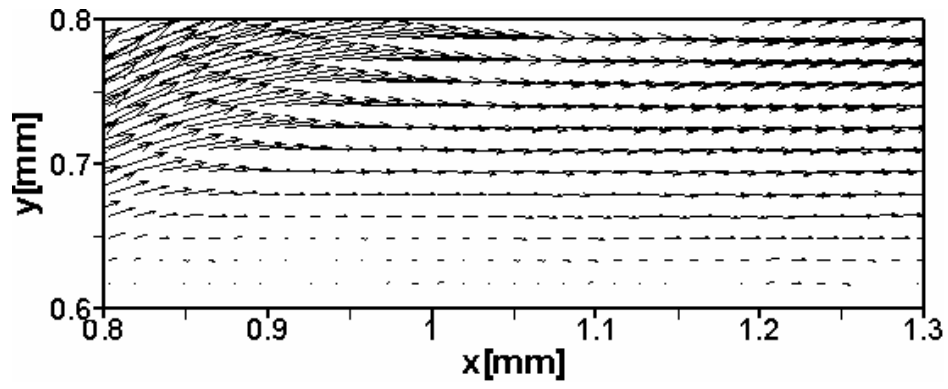
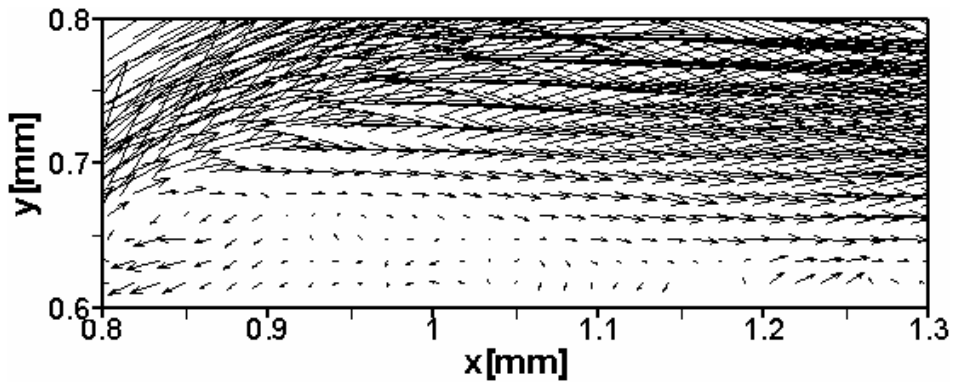


Figure 3-9. Flow structure at the outer wall A) $Re = 100$ B) $Re = 300$ C) $Re = 500$ D) $Re = 1000$ E) $Re = 1500$ and at the inner wall F) $Re = 100$ G) $Re = 300$ H) $Re = 500$ I) $Re = 1000$ J) $Re = 1500$

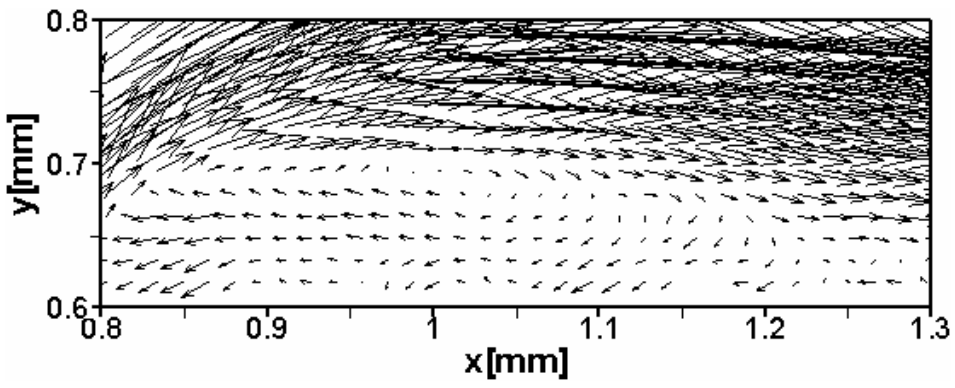
F



G



H



I

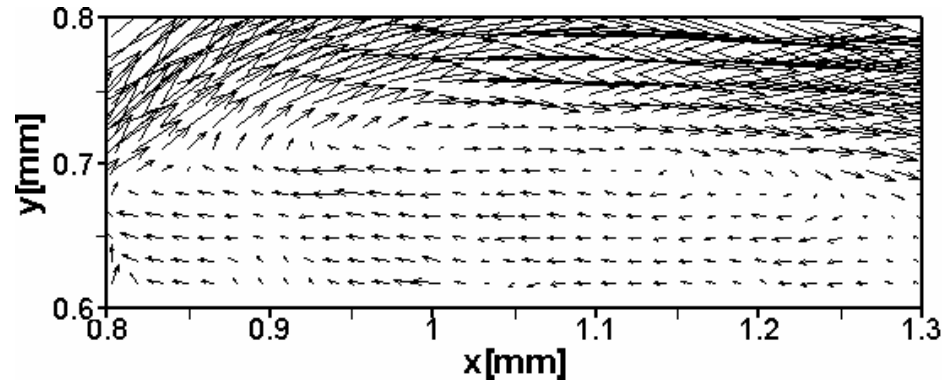


Figure 3-9. Continued

J

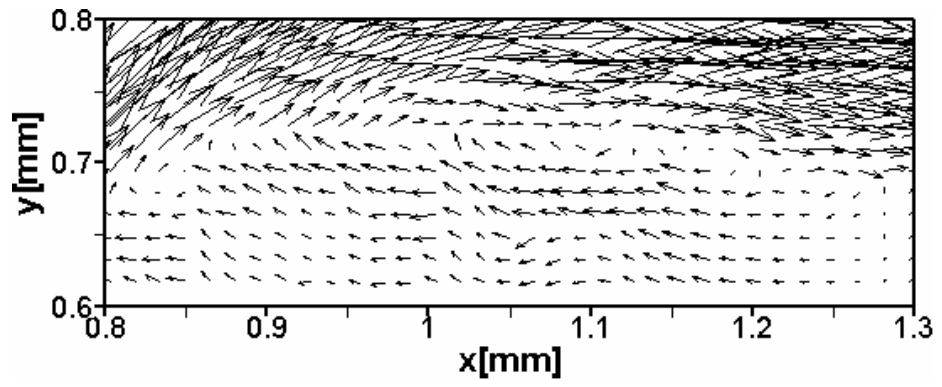
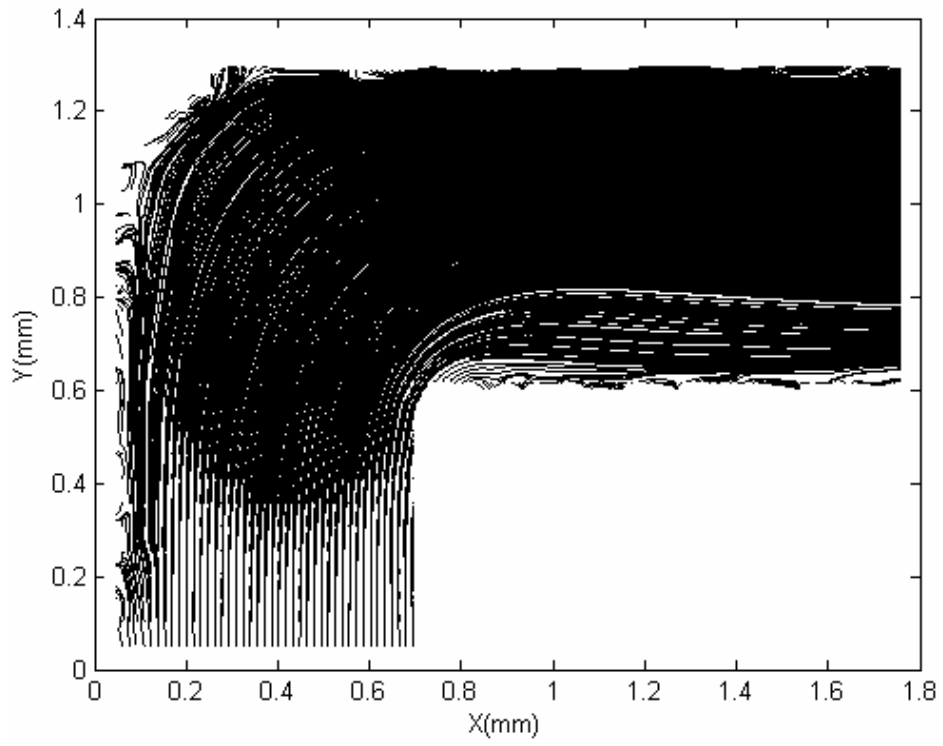


Figure 3-9. Continued

A



B

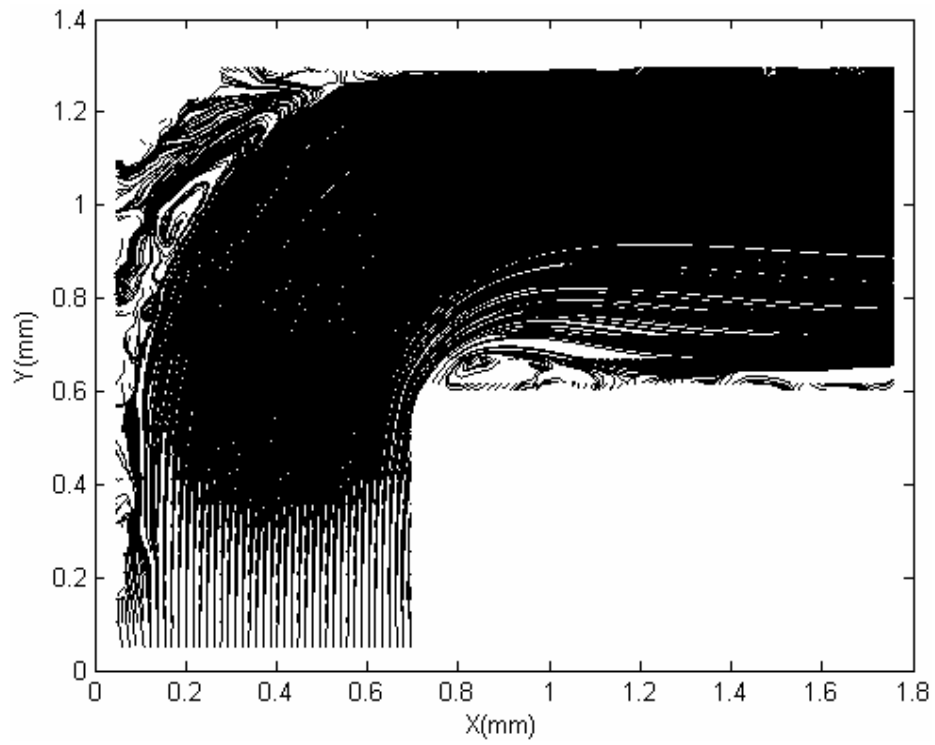
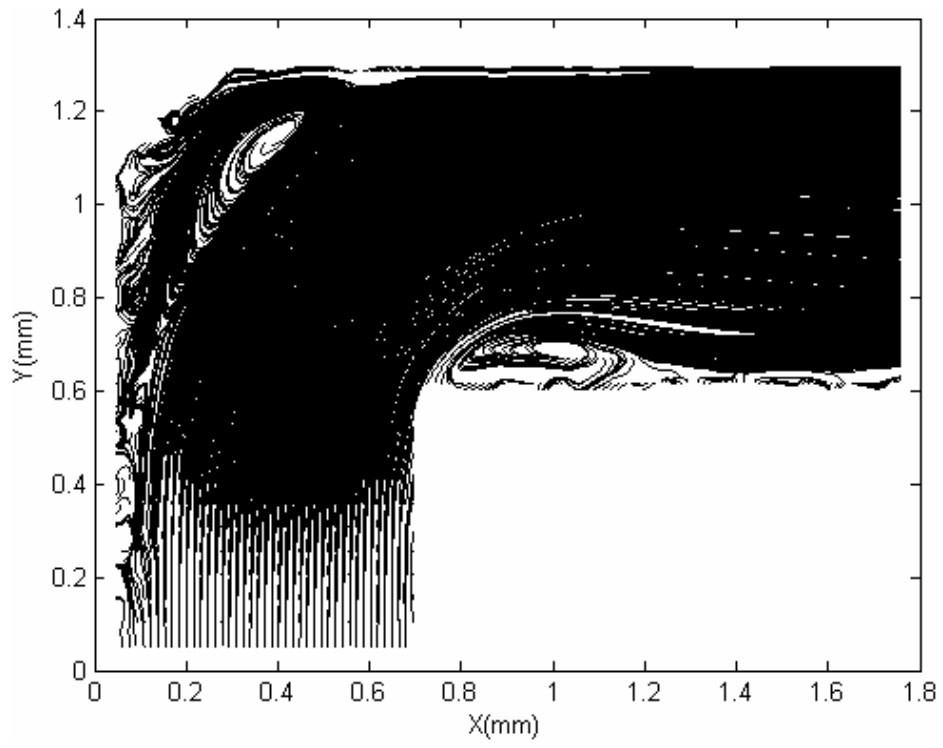


Figure 3-10. Streamlines at different Re numbers: A) $Re = 100$, B) $Re = 300$, C) $Re = 500$, D) $Re = 1000$, and E) $Re = 1500$

C



D

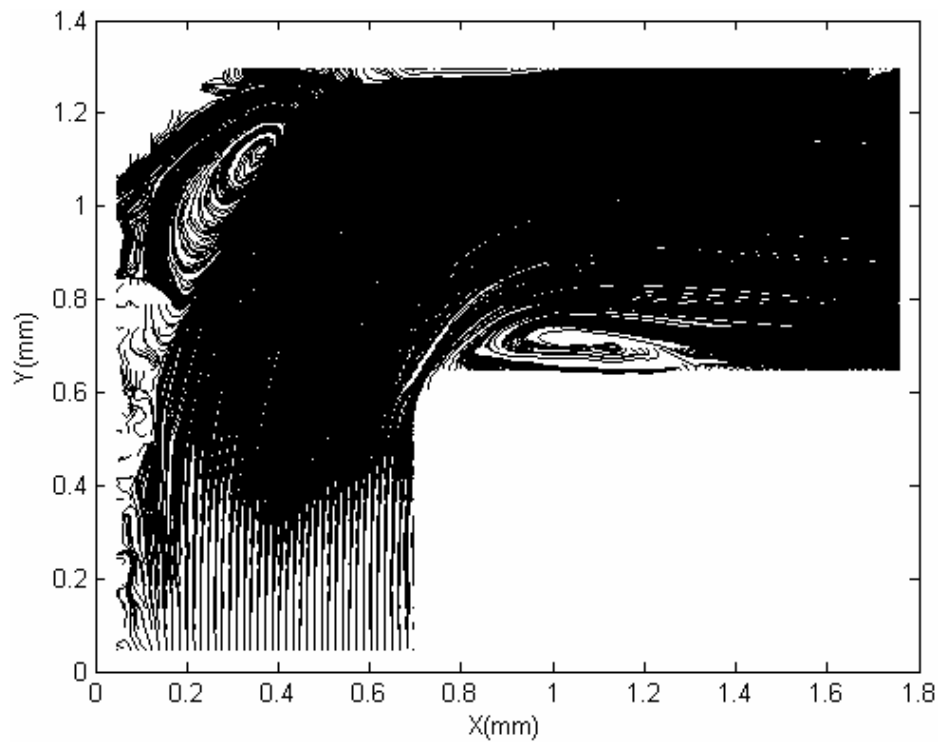


Figure 3-10. Continued

E

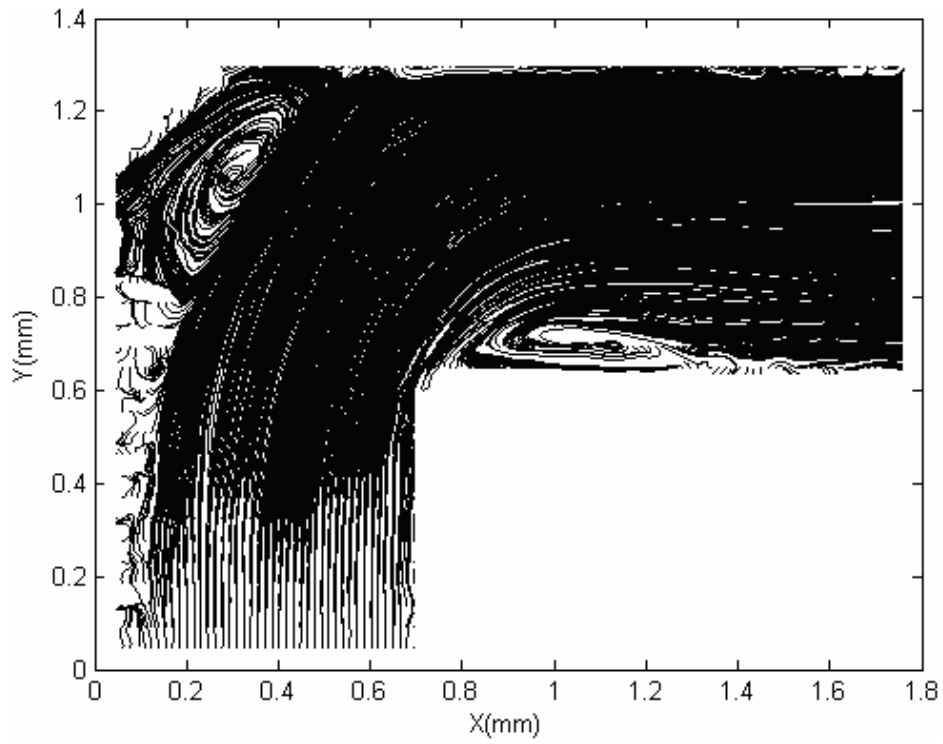


Figure 3-10. Continued

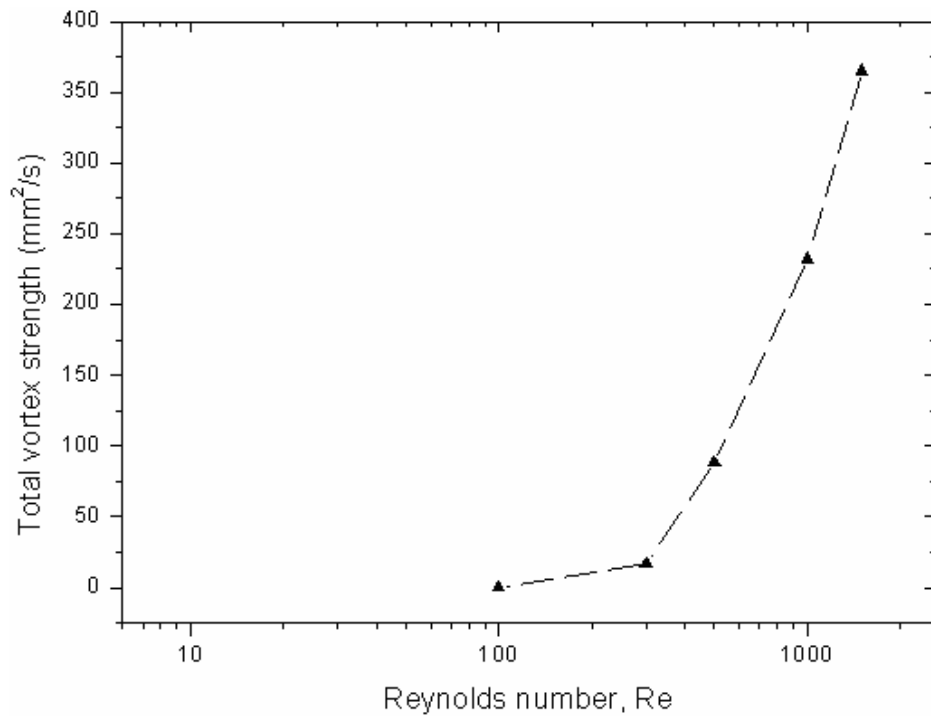


Figure 3-11. Total vortex circulation vs. Reynolds number.

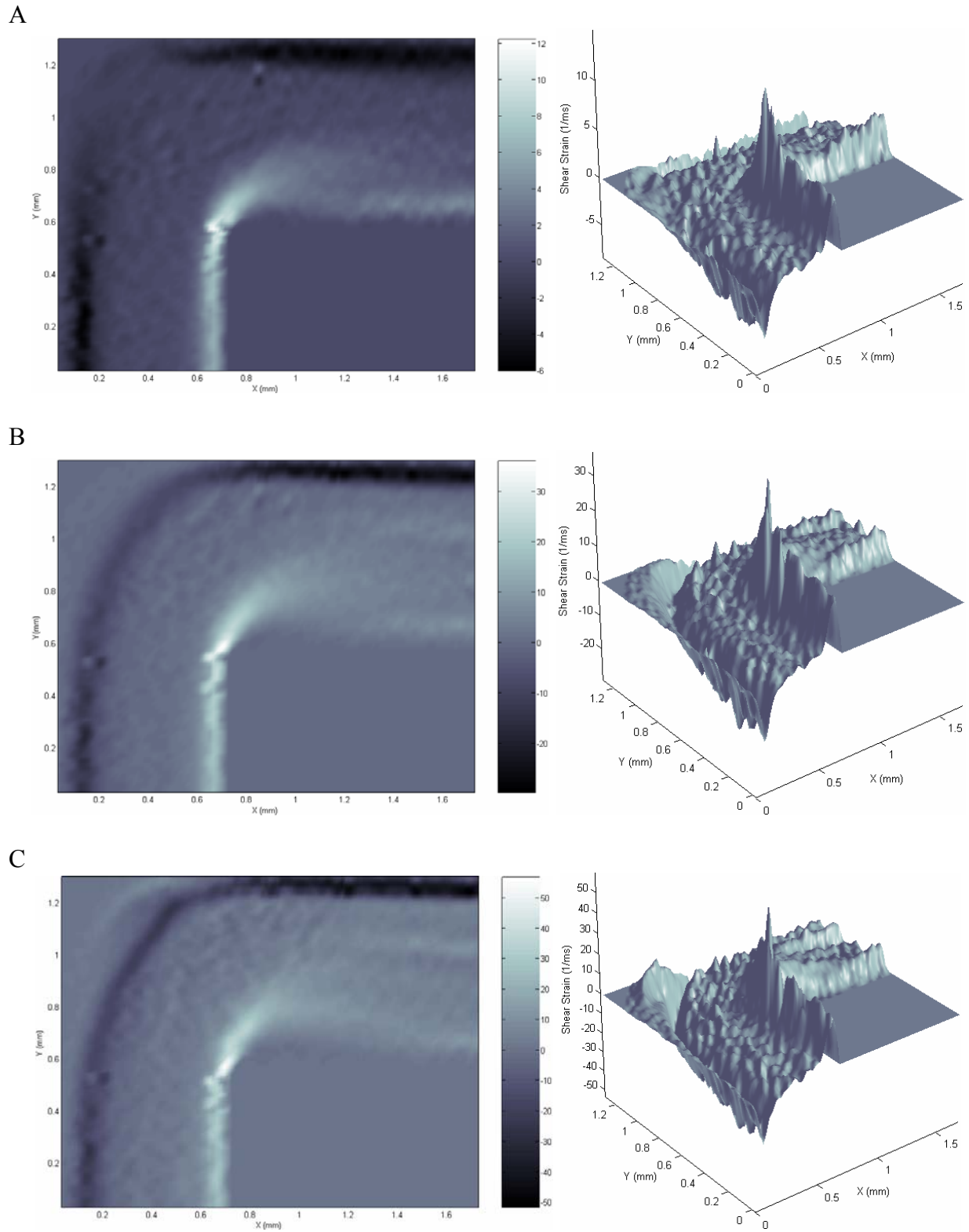
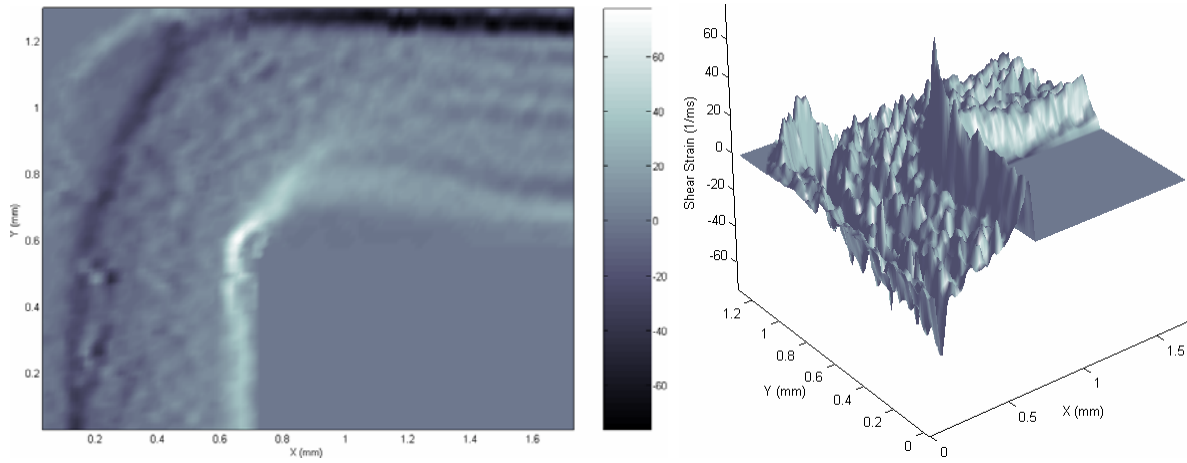


Figure 3-12. Distribution patterns of shear strain rates. A) $Re = 100$, B) $Re = 300$, C) $Re = 500$, D) $Re = 1000$, E) $Re = 1500$.

D



E

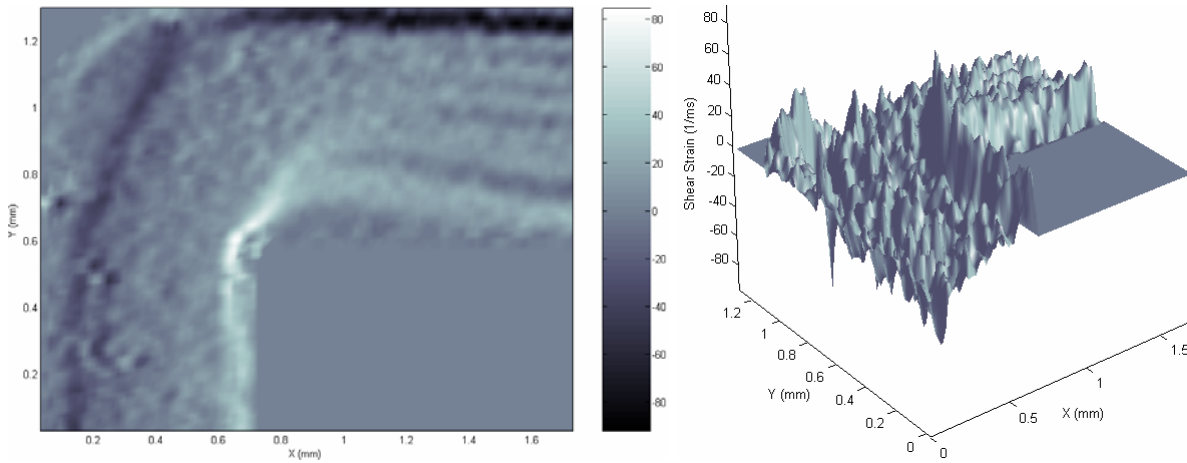


Figure 3-12. Continued

CHAPTER 4 ADIABATIC GAS-LIQUID TWO-PHASE FLOW

In this chapter, adiabatic gas-liquid flow patterns and void fractions in micro-channels were experimentally investigated. Using nitrogen and water, experiments were conducted in rectangular micro-channels with hydraulic diameters of 0.209 mm, 0.412 mm and 0.622 mm, respectively. Gas and liquid superficial velocities were varied from 0.06-72.3 m/s and 0.02-7.13 m/s, respectively. The main objective is focused on the effects of micro-scale channel sizes on the flow regime map and void fraction. The instability of flow patterns was observed. Four groups of flow patterns including bubbly-slug flow, slug-ring flow, dispersed-churn flow and annular flow were observed in micro-channels of 0.412 mm and, 0.622 mm. In the micro-channel of 0.209 mm, the bubbly-slug flow became the slug-flow and the dispersed-churn flow disappeared. The current flow regime maps showed the transition lines shifted to higher gas superficial velocity due to a dominant surface tension effect as the channel size was reduced. The regime maps presented by other authors for mini-channels were found not applicable for micro-channels. Time-averaged void fractions were measured by analyzing 8000 high speed video images for each flow condition. The void fractions hold a non-linear relationship with the homogeneous void fraction as oppose to the relatively linear trend for the mini-channels. A new correlation was developed to predict the non-linear relationship that fits most of the current experimental data and those of the 0.1 mm diameter tube reported by Kawahara et al. within $\pm 15\%$. Two-phase frictional pressure drop can be predicted within $\pm 10\%$ by Lee and Lee's model.

4.1 Introduction and Background

The flow patterns of adiabatic liquid-gas two-phase flow in the macro-channel have been extensively studied in the past (Mandhane et al. 1974, Taitel and Dukler 1976). Since the

buoyancy effect is suppressed by the surface tension, the flow patterns in the mini/micro channel are different from those observed in the macro-channel (Ghiaasiaan and Abdel-Khalik 2001). Recently many researchers published research results on the gas-liquid two-phase flow patterns in micro/mini channels. Wilmarth and Ishii (1994) researched on adiabatic concurrent vertical and horizontal two-phase air-water flows through narrow rectangular channels with gap widths of 1 and 2 mm. Five flow regimes (stratified smooth, plug, slug, dispersed bubbly, wavy annular) and three transition regions (elongated plug, elongated slug, cap-bubbly) were identified for the horizontal flow. Mishima and Hibiki (1996) measured the flow regimes, void fraction and frictional pressure loss for air-water flow in vertical capillary tubes with inner diameters from 1 to 4 mm. Bubbly flow, slug flow, churn flow and annular flow were observed. Churn flow was never observed in the 1 mm channel. Coleman and Garimella (1999) studied air-water flows in four round tubes with 1.3 mm, 1.75 mm, 2.6 mm, and 5.5 mm inner diameters. Eight flow patterns (bubble, dispersed, elongated bubble, slug, stratified, wavy, annular-wavy, and annular) were observed. Triplett et al. (1999) investigated the air-water two-phase flow patterns in circular channels with 1.1 and 1.45 mm inner diameters and in semi-triangular channels with hydraulic diameters of 1.09 and 1.49 mm. The results showed bubbly, churn, slug, slug-annular and annular patterns can be observed but they poorly agreed with the previous transition models and correlations for macro-channels. Chen et al. (2002) presented the nitrogen-water two-phase flow regimes in circular channels with 1.0 and 1.5 mm. Five flow patterns (bubbly, slug, bubble-train slug, churn, and annular) were found. Kawahara et al. (2002) investigated the two-phase nitrogen-water flow patterns in a 0.1 mm diameter circular tube. Intermittent and semi-annular flows were observed while bubbly and churn flows were not observed. Qu et al. (2004) studied the nitrogen-water two-phase flow in a rectangular micro-channel with a gap of

0.406 mm. The results revealed the dominant flow patterns were slug and annular flows, with the bubbly flow occurring only occasionally and stratified, and the churn flow was never observed.

Void fraction is also an important issue in heat transfer and flow characteristics for gas-liquid two-phase flows. Armand et al. (1946) investigated the void fraction for the horizontal and vertical air-water flow in macro-channels and gave a correlation widely used by others. Zuber and Findlay (1965) built a model named drift flux model to correlate the void fraction data in two-phase flow. This model relates the gas velocity with the mixture mean velocity, distribution parameter C_0 and the mean drift velocity V_{gj} , which can be given by:

$$\frac{j_G}{\alpha} = C_0(j_G + j_L) + V_{gj} \quad (4-1)$$

C_0 depends on the pressure, the channel geometry and the flow rate for a given flow pattern. Ali et al. (1993) found that the mean drift velocity V_{gj} can be neglected in narrow channels due to the inability of the bubbles to rise through the stagnant liquid and reported that the void fraction in narrow channels with the hydraulic diameter around 1 mm can be approximately given by the Armand-type correlation with a different distribution parameter. Chung et al. (2004) investigated the void fraction in a 0.1 mm diameter circular tube and a square micro-channel with a hydraulic diameter of 0.096 mm and found the void fraction was independent of the channel geometry in their experiment. Kawahara et al. (2002) experimentally achieved a non-linear relationship between the measured void fraction and the homogeneous void fraction in a 0.1 mm diameter tube. According to the above literature review, more experimental data for the flow patterns and void fraction in the channels of sizes from 1 mm to 0.1 mm need to be obtained to understand the flow performance in micro-channels.

To evaluate the frictional pressure drop of two-phase flow, there were a lot of models and correlations to predict it for macro-channels, mini-channels and micro-channels. Table 4-1 listed

the previous two-phase pressure drop correlations. Triplett et al. (1999) researched on the two-phase pressure drop for the channels with hydraulic diameter of 1.1 and 1.45 mm. He found the homogeneous model provided the best agreement with experimental data for bubbly and slug flow patterns, but all of the widely used correlations significantly over predicted the frictional pressure drop for annular flow. Kawahara et al. (2002) found Lee and Lee's model present the good agreement (within $\pm 10\%$) with experimental data for his circular channel of 0.1 mm diameter. Zhao and Bi (2001) found the Lockhart-Martinelli correlation well predicted the two-phase pressure drop for the triangular channels with hydraulic diameters of 0.866, 1.443 and 2.886 mm.

In this chapter, three near-square micro-channels with the hydraulic diameters of 0.209 mm, 0.412 mm and 0.622 mm were fabricated by laser etching to investigate the nitrogen-water two phase flow patterns, regime maps and time-averaged void fraction. The main objectives of this study are to (1) obtain the flow patterns using a high speed CCD video camera, construct flow regime maps for three micro-channels with superficial velocities of nitrogen and water ranging from 0.06 to 72.3 m/s and 0.02 to 7.13 m/s, respectively, and investigate the size effect on the flow regime maps, (2) compare the new flow maps with the mini-channel flow map based on the Weber number model, (3) evaluate the time averaged void fraction for each micro-channel and compare them with previous correlations, and build an empirical correlation for micro-channels based on current data. Check the predictive ability of the new correlation by using existing time-averaged void fraction data in the literature, (4) obtain the two-phase frictional pressure drops and evaluate the present pressure drop models.

Since the majority of publications in the literature were dealing with the air-water flows, the current work is aimed at providing fundamental understanding and design information for

nitrogen-water two-phase flows in micro-channels due to their close relationship with the PEM fuel cells that are receiving top priority for their central role in the hydrogen economy.

4.2 Experimental Apparatus

Fig. 4-1 shows the schematic of the experimental apparatus and the mixer used to investigate the adiabatic nitrogen-water two-phase flow in micro-channels. It includes a syringe infusion pump (Cole-Parmer Instrument), 60ml syringe (McMaster), micro-filter (Swagelok), nitrogen gas cylinder, regulator (McMaster), flow meters (Omega), valves (Swagelok), Fiber-Lite MI-150 high intensity illuminator (Dolan-Jenner), micro-channels, high speed CCD camera (Redlake), and computerized image acquisition system.

The de-ionized water with flow rates ranging from 0.5ml/min to 46ml/min, which can be set on the panel of the infusion pump, was driven to the micro-channel test section. The 2 μ m micro-filter can remove any particles or bubbles before the flow entered into the micro-channel. The nitrogen gas was released from the compressed gas cylinder. After the regulator, the gas pressure was reduced to 0-30 PSI. The gas flow rate was measured by two volume flow meters with ranges of 0-50 SCCM and 0-2610 SCCM, respectively. The mixer was fabricated as a bubble generator. A needle with a 0.2 mm inner diameter was connected to the 1/8 inch gas tube. It was inserted onto the centerline of the 1/8 inch liquid tube. After going through the 1/8 inch gas tube and the needle, the gas flow was mixed with the de-ionized water coming from the 1/8 inch liquid tube and directed into the micro-channel. The superglue was used to bond the micro-channel to the 1/8 inch tube, and it can be easily removed by the superglue remover, so the micro-channel can be replaced easily to make up different test sections. Two pressure transducers with a $\pm 0.5\%$ FS accuracy were installed at the inlet and outlet of the micro-channel respectively to measure the upstream and downstream pressure. The data acquisition system

started recording when the flow can be considered as steady state. The test sections were placed horizontally. All experiments were conducted in room temperature and under atmospheric pressure at the discharge of the test section. Flow visualization was achieved by the high speed CCD camera, which can operate at a frame rate up to 8000 fps and a shutter speed of 1/8,000 s. In this work, the frame rate of 1000 fps and a shutter speed of 1/2,000 s were used. The resolution of the camera was 240(H) × 210(V) pixels. Two Fiber-Lite illuminators provided the high intensity light, which was directed onto the test section by two optical fiber light guides. An adjustable microscopic magnification lens was used to magnify the test section. The view field was near the outlet of the micro-channel to minimize the entrance effect, and the view field length was 1.48 mm.

Fig. 4-2 shows the photograph of three size micro-channels and schematic of the micro-channel used in the experiment. The micro-channel was laser etched in a silicon substrate and then a Pyrex thin cover glass plate was anodically bonded on the top of the substrate. Two small connection tubes which can be inserted into the inlet and outlet assembly were connected with the small reservoirs. A microscope (Olympus BX50), a 10× objective lens and a CCD camera were used to measure the dimensions of the micro-channels.

In order to facilitate a meaningful discussion, the relative dominance of the forces involved in the two-phase flow is analyzed through six dimensionless groups. These are defined as

follows: $Bo = g(\rho_L - \rho_G)D_h^2 / \sigma$, $Ca = \mu_L j_L / \sigma$, $Re_{GS} = \rho_G j_G D_h / \mu_G$, $Re_{LS} = \rho_L j_L D_h / \mu_L$,

$We_{GS} = \rho_G j_G^2 D_h / \sigma$, and $We_{LS} = \rho_L j_L^2 D_h / \sigma$. Here g is gravitational acceleration, ρ is density,

D_h is hydraulic diameter of the channel, σ is surface tension, μ is viscosity, and j is superficial

velocity. The subscripts “L”, “G” mean the variables are based on liquid, gas flow respectively

and “LS”, “GS” mean the dimensionless numbers are based on superficial liquid, superficial gas

flow respectively. Table 4-2 lists the ranges of those dimensionless parameters for the three channels under experimental conditions. For comparison purposes, parallel values for a 10 cm macro-scale channel are also provided to focus on the scale effects.

With the information given in Table 4-2, we can examine the major differences on the relative importance of various forces involved in a gas-liquid flow between the macro and micro scales. For the flow rates used in our experiments, both the surface tension and the viscous forces are at least two to three orders of magnitude smaller than the gravitational and inertia forces for the macro-scale channel as indicated in Table 4-2. Whereas for the three micro channels in our experiments, it is very clear that the gravitational and viscous force are dominated by the surface tension and inertia forces by at least two orders of magnitude. Comparing between the macro and micro scales, we can conclude that the major change in the force balance is the surface tension which is negligibly small in the macro scale and then becomes dominant in the micro scale while the inertia force is important in both scales as it is proportional to the momentum of the flow only. As a result, the following results and discussion are based on the scenario that the two-phase micro-channel flow is dominated by the balance between surface tension and inertia.

4.3 Results and Discussions

4.3.1 Two-Phase Flow Patterns

The high speed CCD camera can record a continuous video for 8 seconds with a frame rate of 1000 fps. Since the frame rate was set at 1000 fps, one image was recorded for every 1ms. For a specific channel size and each flow condition, a total of 8000 images were obtained in one continuous video. From the recorded images, the dynamic structures of the two-phase flow were obtained and the instability of the flow pattern was observed: At a certain gas and liquid superficial velocity, the micro-channel two-phase flow pattern changes with time at a fixed downstream location. Moving the viewing window from the end of the channel to the middle of

the channel, the same phenomenon was found. A scale bar was thought to be helpful in estimating the size of flow structures. It was developed by multiplying the pixel size of the camera by the number of pixels and then dividing it by the magnification factor. For example, in our experiment the pixel size of the CCD camera was 7.4 microns and the magnification factor was around 1.1 in this experiment, so the actual 100-micron length was covered in 15 pixels in the image, and the uncertainty was 2-3 microns. A variety of flow patterns appeared such as “single-phase liquid”, “bubbly flow”, “slug flow”, “bubble-train slug flow”, “liquid ring flow”, “liquid lump flow”, etc. Only limited numbers of typical flow pattern images from our experiment are given in Fig. 4-3. According to the appearance of the transition flow patterns such as the “liquid ring flow”, “liquid lump flow”, and “disruption tail of the slug”, the entire flow patterns in the present micro-channels can be categorized into four basic flow patterns based on the balance between the inertia and surface tension. As indicated by the values of Webber numbers in Table 4-1, the relative dominance between inertia and surface tension covers a wide span ranging from where surface tension is three orders of magnitude larger than the inertia to where it is two orders of magnitude smaller. The four basic flow patterns are explained below:

- 1) *Bubbly-Slug flow*: This regime is dominated by the surface tension force. It mainly has the “slug flow”, and occasionally “bubbly flow” would show up. Transitional flow patterns of “liquid ring flow” and “liquid lump flow” do not appear here. It usually appears at a low gas flow rate. The “slug flows” were separated by a thick liquid bridge. The width of nitrogen gas slugs is slightly smaller than that of the channel due to the existing smooth and thin liquid film on the walls. Occasionally, some spherical bubbles, whose diameters are much smaller than the width of the channel, appear.

2) *Slug-Ring flow*: This regime is controlled by the balance between the surface tension force and the inertia force, also called the transition regime. Surface tension force and inertia force are comparable to each other in this region. It mainly features the “slug flow”, “liquid ring flow”, “bubble-train slug flow”, and occasionally “bubbly flow”. It often appears at intermediate gas flow rates. The liquid bridge sometimes is thick and forms the “slug flow”, while other times it is quite thin and forms the “bubble-train slug flow”, and even at times it disappears half and forms the “liquid ring flow”. The ring-shaped liquid film is smooth and axi-symmetrically distributed around the channel inner wall. The nose of the slug is flatter than that observed in a bubbly-slug flow.

3) *Dispersed-Churn flow*: In this regime, the flow is strongly influenced by the inertia force but not totally dominated. The main characteristic feature is a mixture of small vapor slugs and liquid chunks. It has no stable “slug flow”. Dispersed-churn flow is also called bubbly/slug, liquid/slug, and ring/slug by other researchers. It normally appears at the intermediate liquid and gas flow rates. For example, among the dispersed-churn flows from the recorded images, we can see the “disruption tail of the slug” flow pattern usually followed by some very small shedding bubbles.

4) *Annular flow*: This regime is totally dominated by the inertia force. It mainly consists of the flow pattern of “gas core with a smooth interface”, and occasionally the “liquid lump flow”. It usually appears at a low to intermediate liquid flow rate together with a high gas flow rate. The water film flows along the channel inner wall while the nitrogen gas core flows through the center of the channel. The gas-liquid interface is smooth due to the weak interaction between the gas and liquid at the interface in the micro-channel, which is different from the wavy interface observed in mini-channels and macro-channels.

Fig. 4-4 shows the instable temporal pressure measurement at the upstream and downstream for a slug-ring flow. This instability of P_{in} can be attributed to or cause the density wave oscillation in the micro-channel, which was also found in parallel channels and believed to be intrinsic to the test module itself (Qu and Mudawar 2004). The density oscillation could change the gas inertia force $\rho_G j_G^2$ at the interface. That could be the reason why the time instability of flow patterns observed in the micro-channel.

4.3.2 Flow Regime Maps

Based on the images and pattern distinctions discussed above, we have summarized our observations using two-phase flow regime maps. Traditionally, the regime map was developed with the superficial velocities of water and nitrogen, j_L and j_G , as the vertical and horizontal coordinates, respectively. Instead of the superficial velocities, we decided to use the respective gas and liquid Webber numbers as the coordinates for the regime maps. Essentially, the Webber number is the dimensionless superficial velocity square and physically it represents the ratio of inertia to surface tension that is the guiding parameter for two-phase flow patterns in micro-channels. Fig. 4-5 shows the regime maps for the three channel sizes. The solid lines are used to indicate the boundaries between different flow patterns. Figs. 4-5(a) and 4-5(b) provide the two-phase flow regime maps for the current micro-channels with hydraulic diameters of 0.622 mm and 0.412 mm, respectively. Fig. 4-5(c) shows the flow regime map for the micro-channel with a hydraulic diameter of 0.209 mm.

In general, for the larger channels (0.622 mm and 0.412 mm), the regime maps are relative similar as shown in Figs. 4-5(a) and 4-5(b). They all have bubbly-slug flows located in the lower left corner representing very small Webber numbers that correspond to a total dominance by the surface tension force. For higher gas velocities that are associated with larger gas Webber

numbers and dominance by the inertia force, the flow pattern becomes the annular flow and it is not very sensitive to the liquid velocities. Between the bubbly-slug flow and the annular flow, we found the slug-ring and dispersed-churn flows that corresponds to the relatively balance between the inertia and the surface tension and neither one is dominant. The slug-ring flow is under relatively more control by the surface tension while the disperse-churn is controlled more by the inertia as a larger inertia force offered by the higher liquid flow is needed to break the slug into dispersed fragments. This is why the disperse-churn flow is located above the slug-ring flow. While for the smallest channel (0.209 mm), the regime map displays some differences from those of the larger channels. We observed that the bubbly flow pattern was no longer present and the slug flow filled its place in the lower left corner, lower We_{LS} and We_{GS} (lower j_G and j_L). A plausible explanation is that as the channel size gets smaller the surface tension force holds a deeper control over the inertia for the same low gas flows that prevents the break up of the bridge between slugs to form bubbles. Therefore the slug flow resulted. The dispersed-churn flow was also absent in Fig. 4-5(c), the slug-ring flow took its place. Again, the reason is that the strong surface tension effect prevented break-down of the slugs and the disruption of the gas-liquid interface.

From the current experimental data, we also observed the boundary lines have a tendency to shift slightly to right, namely higher We_{GS} or gas superficial velocity, as the hydraulic diameter was decreased, which was different from what reported by Taitel et al. (1980) that the boundary line was not affected by tube diameter for circular vertical macro-tubes, or by Mishima and Ishii (1984) that the boundary line shifted to the left in vertical macro-tubes as the tube diameter was decreased. This again may be explained by the stronger surface tension effect in micro-channels that requires a higher inertia force (boundary line moving to the right) to balance in order to

maintain the same flow pattern. Tabatabai and Faghri (2001) reported a new flow map based on their theoretical study that accounted for surface tension effects in horizontal miniature and micro tubes. They showed an increasing ratio of gas superficial velocity to liquid superficial velocity with the decreasing of hydraulic diameter, which indicated a right shift of the transition boundary lines too.

4.3.3 Comparison with Prior Mini-Channel Flow Map

Akbar et al. (2003) reviewed the flow maps in mini-channels with hydraulic diameter around 1 mm and concluded that there were some similarities between the flow regime transitions in mini-channels and channels operating under microgravity. They developed a flow map for circular and near-circular mini-channels based on the Weber number, which can be represented by the following expressions:

- Surface tension dominated region (including bubbly, plug, and slug flows):

- For $We_{LS} \leq 3.0$, $We_{GS} \leq 0.11We_L^{0.315}$

- For $We_{LS} > 3.0$, $We_{GS} \leq 1.0$

- Annular flow region:

$$We_{GS} \geq 11.0We_{LS}^{0.14}, We_{LS} \leq 3.0$$

- Dispersed flow region:

$$We_{LS} > 3.0, We_{GS} > 1.0$$

This model can reasonably explain the flow maps for circular and near-circular mini-channels with hydraulic diameter around 1 mm including the data of Mishima et al. (1996), Triplett et al. (1999), and Yang & Shieh (2001). However, it only provided a fair prediction to the data of Zhao and Bi (2001) due to the channel geometry effects. Fig. 4-6 shows the transition lines predicted by the Weber number model (solid lines) with the current data for the channel with $D_h = 0.622$

mm (dashed lines). A poor agreement was found. One of the possible reasons might be the significant sensitivity of gas-liquid flow patterns to the working fluid, channel geometry and channel size. Another possible reason may be related to some special flow characteristics associated specifically with micro-channels. The liquid and gas flow remain laminar even at high flow rates, and a weaker interaction between the liquid and gas at the interface in micro-channels than in mini-channels. We may conclude that the flow regime criteria developed for mini-channels should not be applied for micro-channels without further verification.

4.3.4 Time-Averaged Void Fraction

For each gas-liquid flow combination, the time-averaged void fraction can be estimated by analyzing its 8000 recorded images. The method of analyzing the time-averaged void fraction is described as follows. 22 data points were selected from the video image files for each channel size to cover the entire range of the homogeneous void fraction. It is noted that each data point corresponds to a specific homogeneous void fraction. The homogeneous void fraction is defined as $\beta = j_G/(j_G+j_L)$ which has a range between zero and one. The physical meaning of the homogeneous void fraction is that the actual void fraction is equal to the homogeneous void fraction when both phases have the same velocities in a dynamic equilibrium condition. The actual void fraction would deviate from the homogeneous void fraction for the dynamic non-equilibrium conditions investigated in the current study where the two phases have non-equal velocities (slip ratio) in different flow regimes. Each recorded image covers the flow pattern for a streamline distance of 1.48 mm. The instantaneous void fraction on each image can be calculated by estimating the ratio of the volume occupied by the gas to that of the whole region on each image field. The time averaged void fraction was obtained by adding all the instantaneous void fractions and dividing the sum by the total number of images, the time-averaged void fraction, α , can be determined and expressed as follows :

$$\alpha = \frac{\sum_{n=1}^N \alpha_n}{N} = \frac{\sum_{i=1}^{N_l} \alpha_{l,i} + \sum_{j=1}^{N_g} \alpha_{g,j} + \sum_{k=1}^{N_m} \alpha_{m,k}}{N}, \quad N = N_l + N_g + N_m \quad (4-2)$$

Eq. (4-2) represents a strategy that we divided the images into three major groups based on the number of images for a specific type. For the total recorded images, approximately, 90% of all the images belong to either pure liquid type or gas core with a smooth interface, and all other types such as “liquid ring flow”, “liquid lump flow”, and “bubbly flow” account for only 10%. As a result, we chose “pure liquid” (zero void fraction), “gas core with a smooth interface” and “all the rest types combined” as the three groups. Therefore, in Equation (4-2), $\alpha_{l,i}$, $\alpha_{g,j}$, $\alpha_{m,k}$ are the estimated void fractions for “pure liquid type”, “gas core with a smooth interface type”, and “any other type”, respectively. N is the total number of the recorded images. N_l , N_g , N_m are the number of the images of “liquid”, “gas core with a smooth interface”, and “other types”, respectively. According to the error propagation, the uncertainty of the estimated time-averaged void fraction, $\Delta\alpha$, can be expressed as:

$$\Delta\alpha = \sqrt{\left(\frac{N_l}{N} \Delta\alpha_l\right)^2 + \left(\frac{N_g}{N} \Delta\alpha_g\right)^2 + \left(\frac{N_m}{N} \Delta\alpha_m\right)^2} \quad (4-3)$$

where $\Delta\alpha_l$, $\Delta\alpha_g$, $\Delta\alpha_m$ are the uncertainties of the void fractions for “liquid”, “gas core with a smooth interface”, and “all other flow pattern”, respectively. Even though, the void fraction of “pure liquid” is zero, there is still an uncertainty associate with it because of possible trace amount of gas in the liquid core, but in general this uncertainty is very small compared to other types. Based on the above, we estimated that the range of uncertainties for the time averaged void fractions is from 3.1% to 9.8%.

Fig. 4-7 shows the measured time-averaged void fraction results for the present three micro-channels. Also shown in Fig. 4-7 is the data given by Kawahara et al. (2002) for a micro-tube with 0.1 mm in diameter. The dotted line represents the homogeneous void fraction β . Ali et al. (1993) suggested that the void fraction in narrow channels with a D_h around 1mm can be correlated with the equation, $\alpha = 0.8 \beta$. When applying this correlation to our results, we found that for the vast majority of our data, it overestimated the void fractions, especially for the smaller channels. The predictions become worse as the size of the channel is decreased further. The over-predictions are more than 100% for many data points. The time-averaged void fraction patterns for the smaller channels showed a non-linear relationship with the homogeneous void fraction. As explained before, when the channel sizes are smaller, the effects of surface tension are more prevalent, and allow the liquid film to bridge the gas core more easily, so the flow pattern is more likely to be bubbly-slug flow, which results in a lower time-averaged void fraction due to the absence of gas phase.

Based on our own data for the three micro-channel sizes (0.209 mm, 0.412 mm and 0.622 mm) and those of Kawahara et al. (2002) for a 0.1 mm diameter micro-tube, we have developed an empirical correlation of the time-averaged void fraction for micro-channels with hydraulic diameters less than 1 mm. The correlation is expressed in Eq. (4-4) and Eq. (4-5)

$$\alpha_p = \frac{C\beta^{0.5}}{1 - (1 - C)\beta^{0.5}} \quad (4-4)$$

$$C = \frac{0.266}{1 + 13.8 \cdot e^{-6.88D_h}} \quad (4-5)$$

where the unit of D_h is in mm. Fig. 4-8 shows the comparison between the predictions by the new correlation and the corresponding measured results. Fig. 4-9 is a plot of the α_p/α_d vs β for all the data points in Fig. 4-8, where α_p and α_d are the void fraction predicted by the correlation

and that of the measured data, respectively. 57 of our 66 data points fall within $\pm 15\%$. Most of the outliers came from Kawahara et al's data (17 out of 26 outliers) which may be attributed to the lack of the total number of sample images (200-300) in their experiment resulting in higher uncertainties. If the uncertainty range was increased to $\pm 35\%$, only 2 data out of 66 were out of the range.

4.3.5 Frictional Pressure Drop

Currently most of the two-phase pressure drop models are based on the model of Lockhart-Martinelli (1949), such as Mishima and Hibiki (1996), Lee and Lee (2001), Qu and Mudawar (2004). To compare our experimental data with the prediction of those models, the Martinelli parameter X should be determined experimentally first, which is defined as:

$$X = \frac{(dP/dz)_L}{(dP/dz)_G} \quad (4-6)$$

$(dP/dz)_L$ and $(dP/dz)_G$ are the frictional pressure drop of single phase liquid and vapor with the same mass flow rate respectively. Then insert X into the above models to get the two-phase frictional pressure drop. Fig. 4-10 shows the comparison between the experimental data of the micro-channel ($D_h = 0.412$ mm) and the value predicted by those models. From the figure, we can see Lockhart-Martinelli's model ($C=5$) obviously underestimate the pressure drop here. Mishima and Hibiki's model can predict the pressure drop very well. All of the data fall in $\pm 10\%$ of the predicted value. Lee and Lee's model may also predict well, but it's worse than Mishima and Hibiki's model for our experimental data.

4.4 Summary

Nitrogen-water flow patterns in rectangular micro-channels with hydraulic diameters of 0.209 mm, 0.412 mm and 0.622 mm were obtained and analyzed. Based on our experimental

results and comparison with other results in the literature, the following conclusions can be obtained:

- The phenomenon that micro-channel flow pattern changes with time at a fixed location under a certain gas and liquid superficial velocity was found, which can be attributed to the density wave oscillation in the micro-channel. According to the appearance of the transition flow patterns such as “liquid ring flow”, “liquid lump flow” and “disruption tail of the slug”, four flow patterns can be defined for micro-channels with the hydraulic diameters of 0.412 mm and 0.622 mm: bubbly-slug flow, slug-ring flow, dispersed-churn flow and annular flow. For the micro-channel with the hydraulic diameters of 0.209 mm, the bubbly-slug flow became the slug-flow and the dispersed flow disappeared.
- The current flow regime maps show the transition boundary lines shift to high We_{GS} or gas superficial velocity with the decreasing of the hydraulic diameter. It can be explained by the strong surface tension effect in micro-channels. The micro-channel flow maps were compared with the mini-channel flow map based on the Weber number model, which showed poor agreement.
- Time-averaged void fractions of each micro-channel were measured for 22 runs to cover the whole range of homogeneous void fraction. The data of each run were obtained from the analysis of 8000 flow pattern images captured at a certain gas and liquid superficial velocity. With the decreasing of the hydraulic diameter, the time-average void fraction showed a non-linear relationship with the homogeneous void fraction. A new empirical correlation was proposed to predict the non-linear relationship, and most of the current experimental data and Kawaraha’s data fall within $\pm 15\%$ of the new correlation. The uncertainty of this measurement method was analyzed and the uncertainty range was approximately from 3.1% to 9.8% under the current experimental conditions.
- Lockhart-Martinelli’s model ($C=5$) which was widely used to predict the two-phase frictional pressure loss in macro-channel obviously underestimate the pressure drop in micro-channel. Mishima and Hibiki’s model formulated from experimental data of small channels can predict the pressure drop here very well. All of the data fall within $\pm 10\%$ of the predicted value. Lee and Lee’s model can also predict well, but it’s worse than Mishima and Hibiki’s model for our experimental data.

Table 4-1. Generalized two-phase frictional pressure-drop correlations.

Correlation	Reference	Frictional pressure drop
1	Homogeneous model (1994)	$-\left(\frac{dP}{dz}\right) = \frac{2f_{tp}G^2}{\rho_l D_h} \left[1 + x \frac{\rho_l - \rho_v}{\rho_v}\right]$
2	Lockhart-Martinelli (1949)	$-\left(\frac{dP}{dz}\right) = \frac{2f_l G^2 (1-x)^2}{\rho_l D_h} \phi_l^2$ $\phi_l^2 = \left(1 + \frac{C}{X} + \frac{1}{X^2}\right)$ $X = \frac{(dP/dz)_l}{(dP/dz)_v}$ <p>C = 20 for turbulent liquid-turbulent vapor C = 12 for laminar liquid-turbulent vapor C = 10 for turbulent liquid-laminar vapor C = 5 for laminar liquid-laminar vapor</p>
3	Mishima and Hibiki (1996)	$-\left(\frac{dP}{dz}\right) = \frac{2f_l G^2 (1-x)^2}{\rho_l D_h} \phi_l^2$ $\phi_l^2 = \left(1 + \frac{C}{X} + \frac{1}{X^2}\right)$ $C = 21[1 - e^{-319D_h}]$
4	Lee and Lee (2001)	$-\left(\frac{dP}{dz}\right) = \frac{2f_l G^2 (1-x)^2}{\rho_l D_h} \phi_l^2$ $\phi_l^2 = \left(1 + \frac{C}{X} + \frac{1}{X^2}\right)$ $C = 6.185 \times 10^{-2} \text{Re}_{Lo}^{0.726}$ <p>for laminar liquid-turbulent vapor</p>
5	Qu and Mudawar (2004)	$-\left(\frac{dP}{dz}\right) = \frac{2f_l G^2 (1-x)^2}{\rho_l D_h} \phi_l^2$ $\phi_l^2 = \left(1 + \frac{C}{X} + \frac{1}{X^2}\right)$ $C = 21[1 - e^{-319D_h}] (0.00418G + 0.0613)$

Table 4-2. Non-dimensional parameters for a macro-channel and micro-channels

	Bo	Ca	Re		We	
	(Ratio of gravitational force to surface tension force)	(Ratio of viscous force to surface tension force)	(Ratio of inertia force to viscous force)	Re_{LS}	Re_{GS}	(Ratio of inertia force to surface tension force)
					We_{LS}	We_{GS}
10cm Channel	1354.3	0.00047-0.12	4665-1166276	6320-63200	2.21-138333	1.6-158
Channel 1	0.0117	0.00023-0.08	4.64-1670	7-1631	0.001-135	0.0005-32
Channel 2	0.0230	0.00035-0.04	14.1-1602	7-1838	0.005-63	0.0003-28
Channel 3	0.0525	0.00015-0.02	9.36-1436	7-2270	0.0014-34	0.0003-33

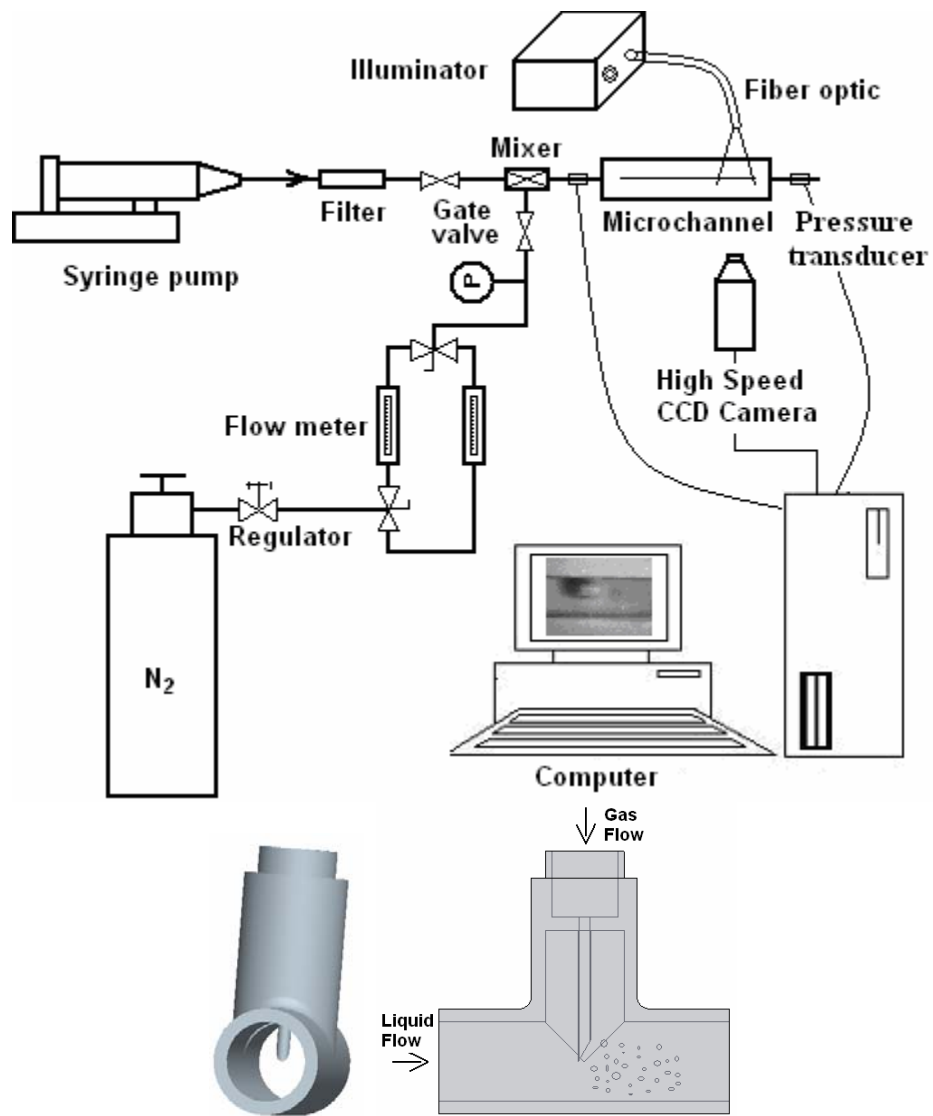


Figure 4-1. Schematic of the flow visualization apparatus and the mixer.

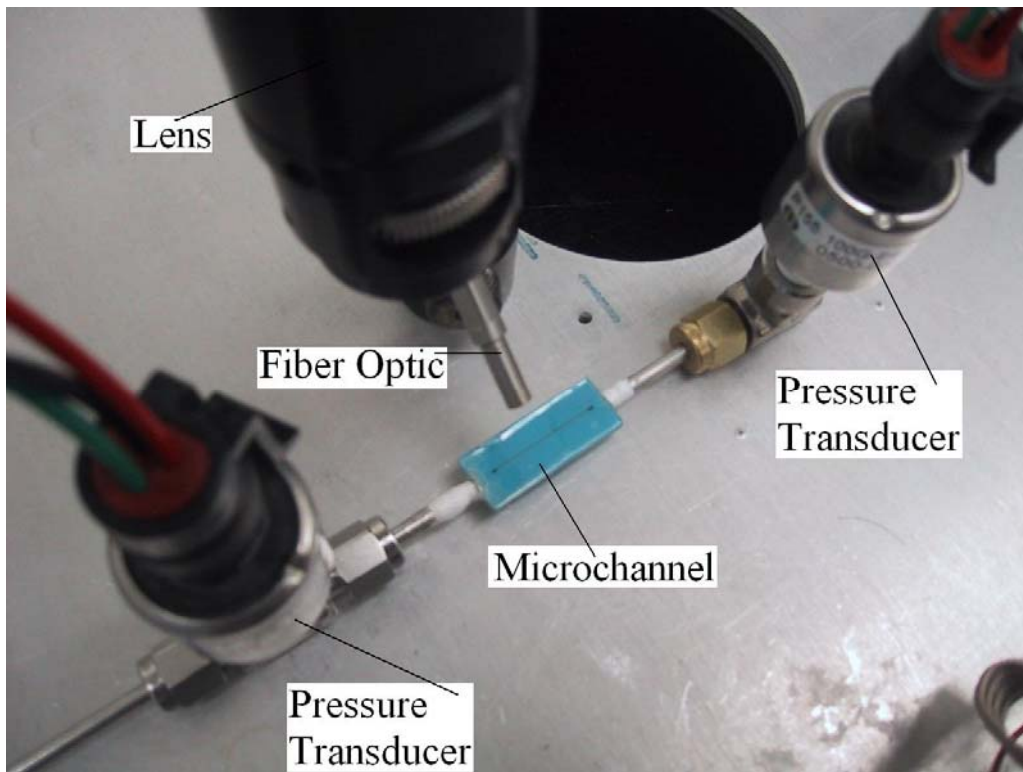
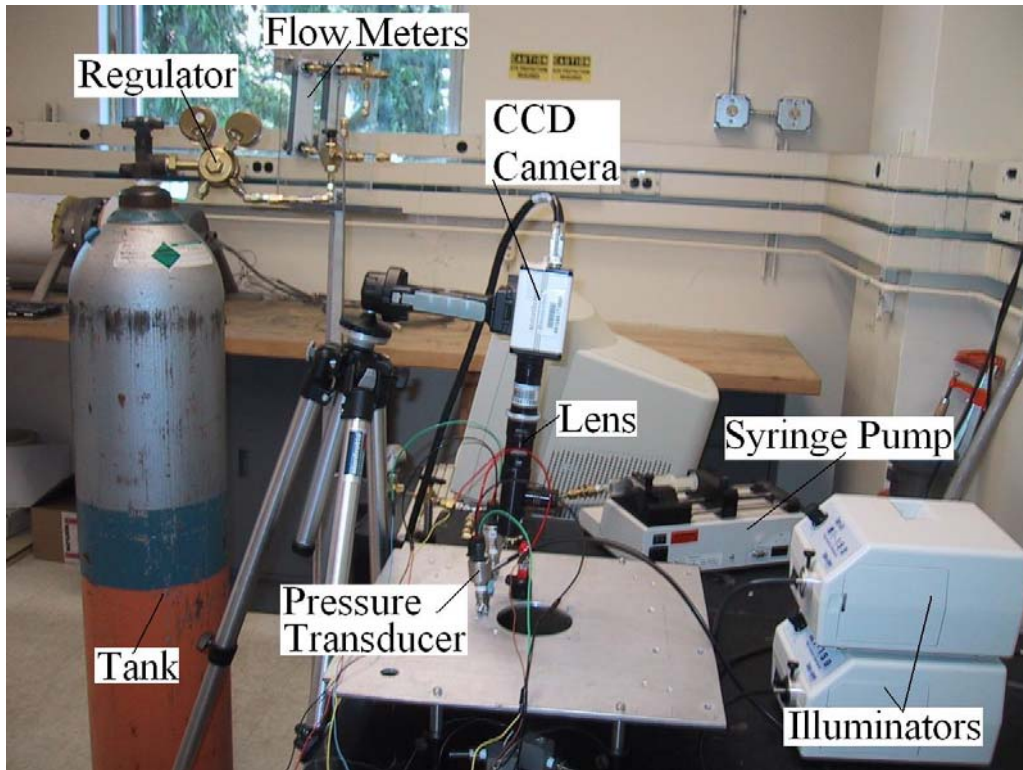


Figure 4-2. Photos of the experimental apparatus

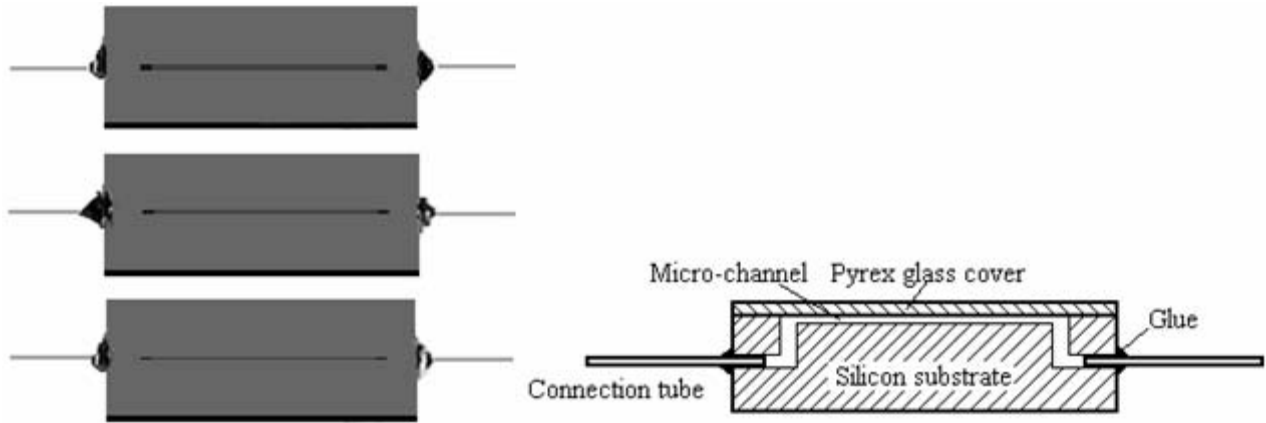


Figure 4-2. Photograph of micro-channels and schematic of the micro-channel.

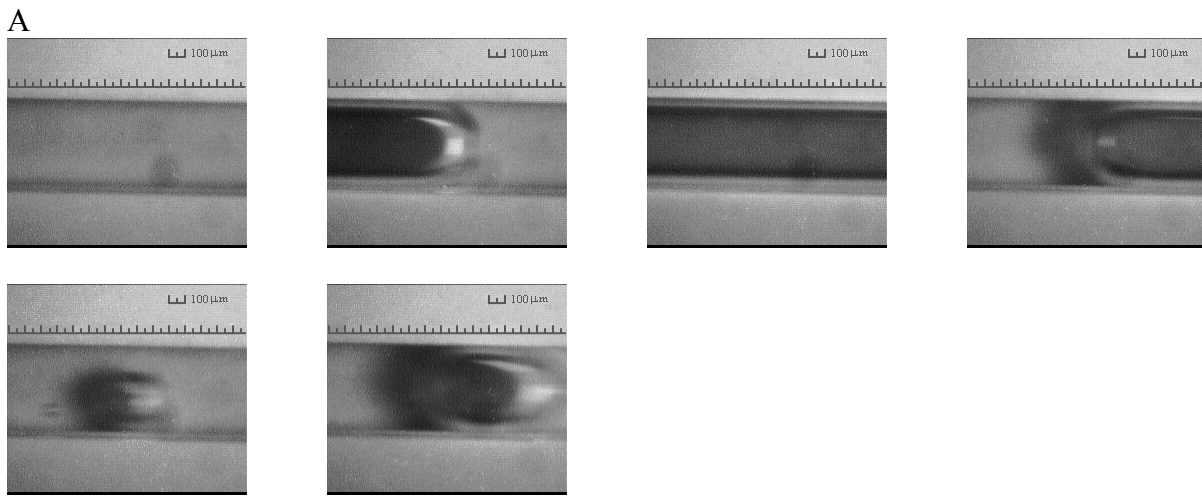
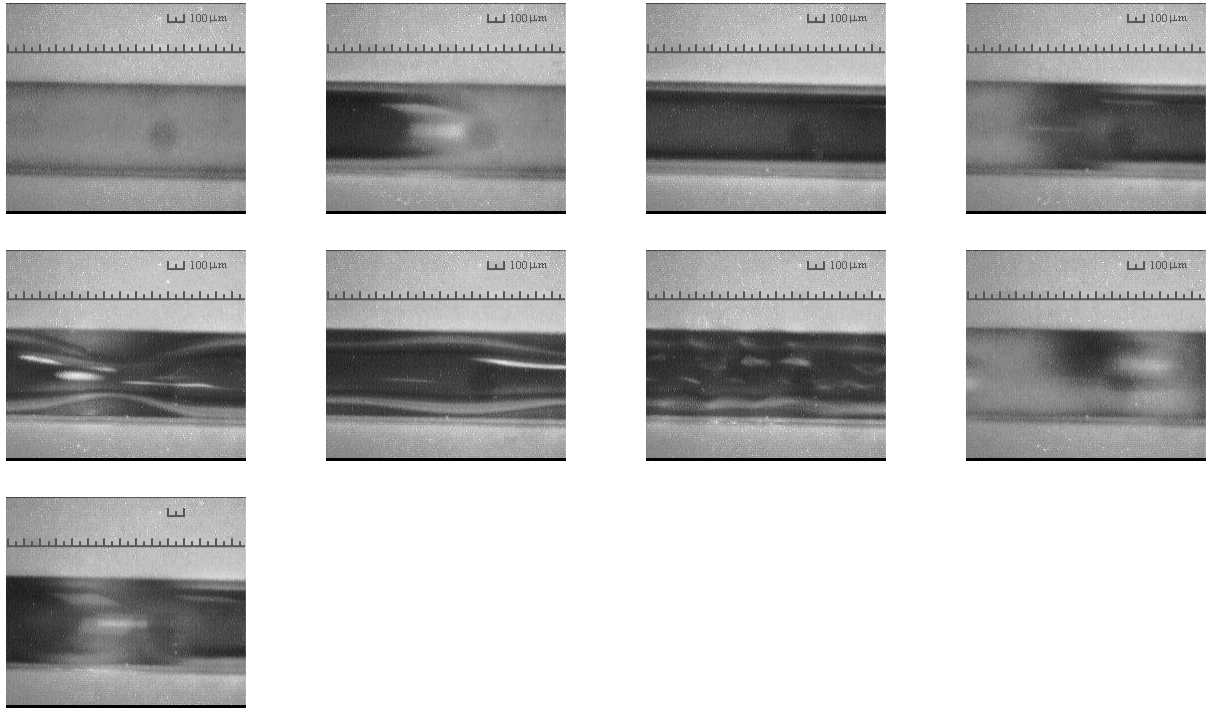
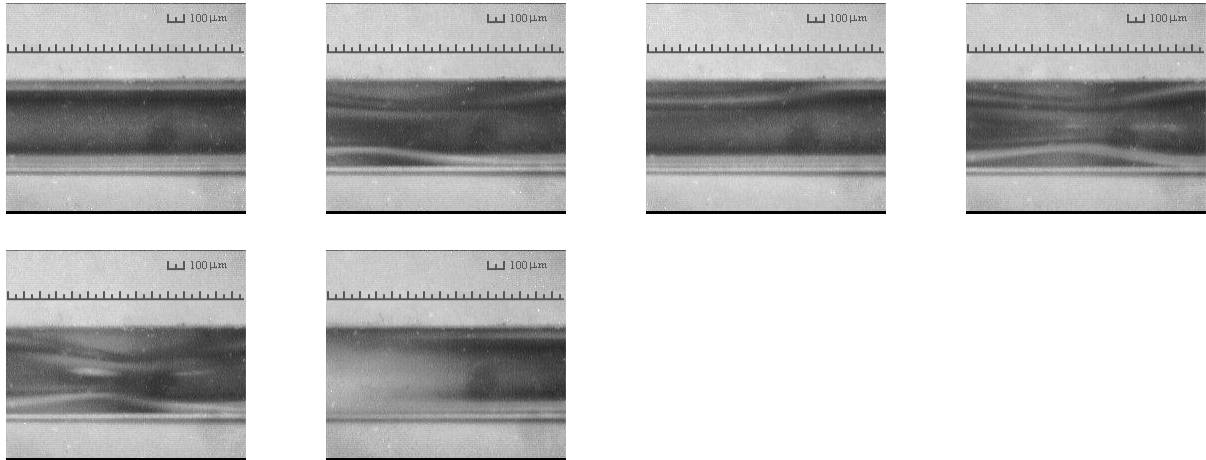


Figure 4-3. Typical flow patterns in the micro-channel: A) Bubbly-Slug flow B) Slug-Ring flow C) Dispersed-Churn flow D) Annular flow.

B



C



D

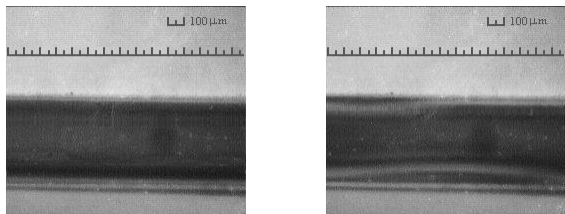


Figure 4-3. Continued

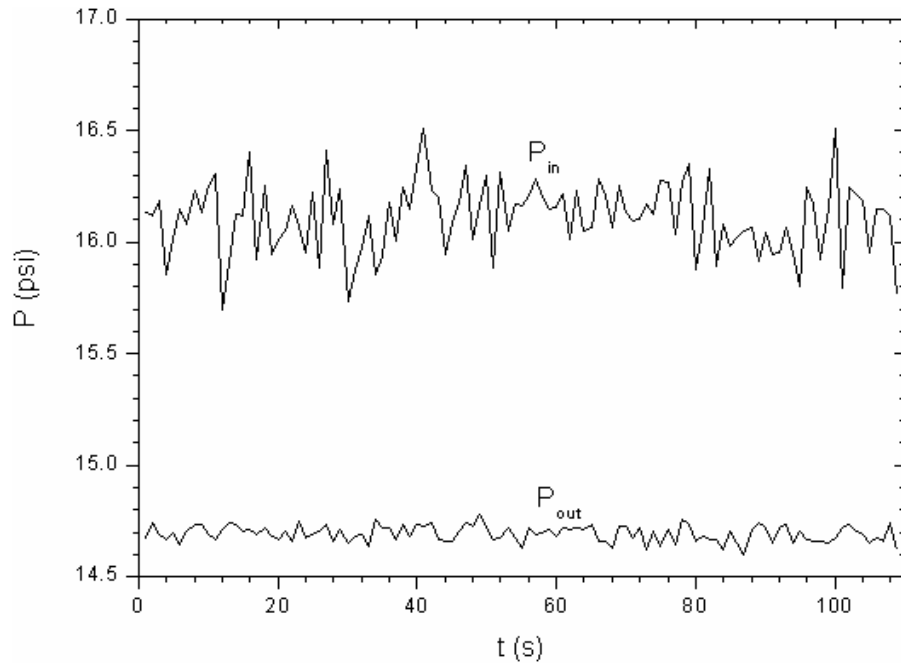


Figure 4-4. Temporal records of inlet and outlet pressures (Slug-Ring flow, $j_L = 0.215\text{m/s}$, $j_G = 1.2\text{m/s}$)

A

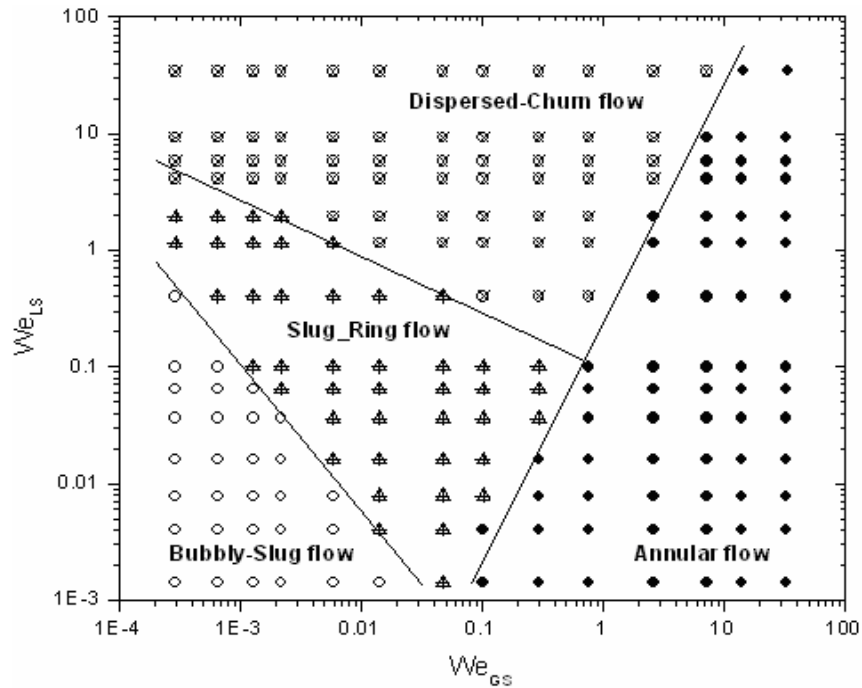
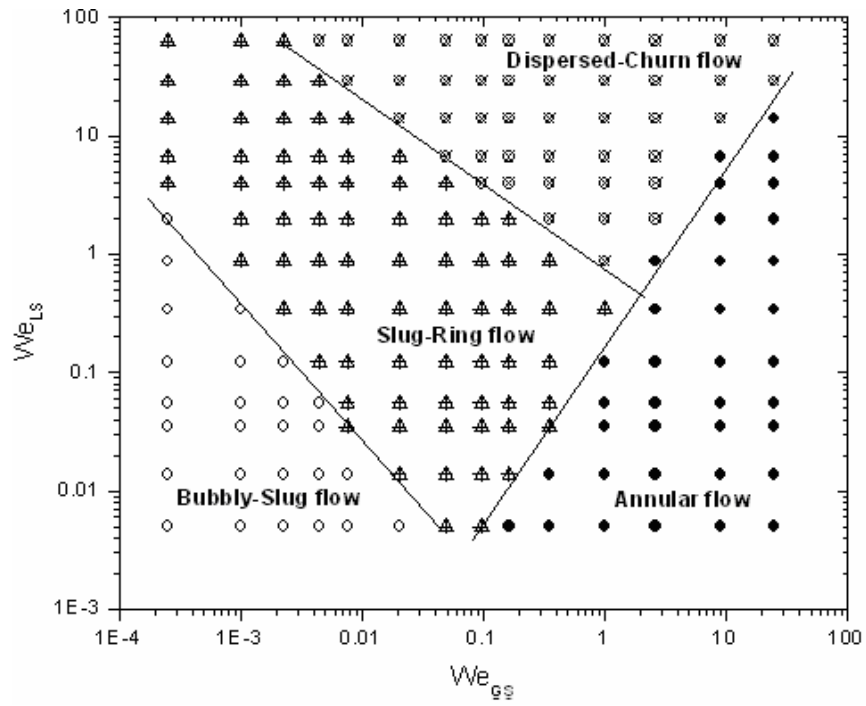


Figure 4-5. Flow regime maps for three micro-channels: A) $D_h = 0.622\text{ mm}$ B) $D_h = 0.412\text{ mm}$
C) $D_h = 0.209\text{ mm}$

B



C

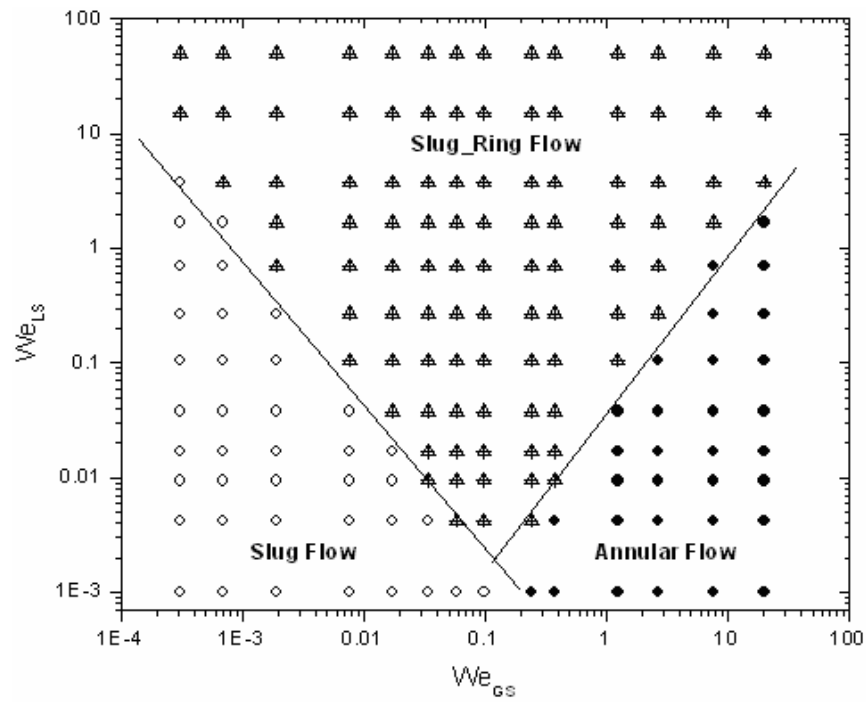


Figure 4-5. Continued

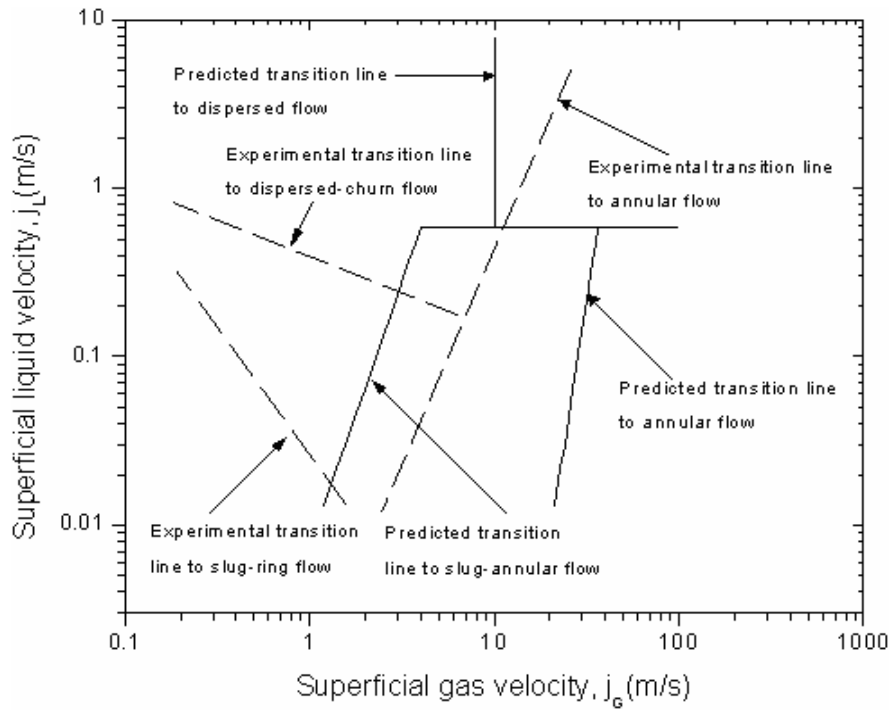


Figure 4-6. Flow map comparison between micro-channel and mini-channel predicted by the Weber number model.

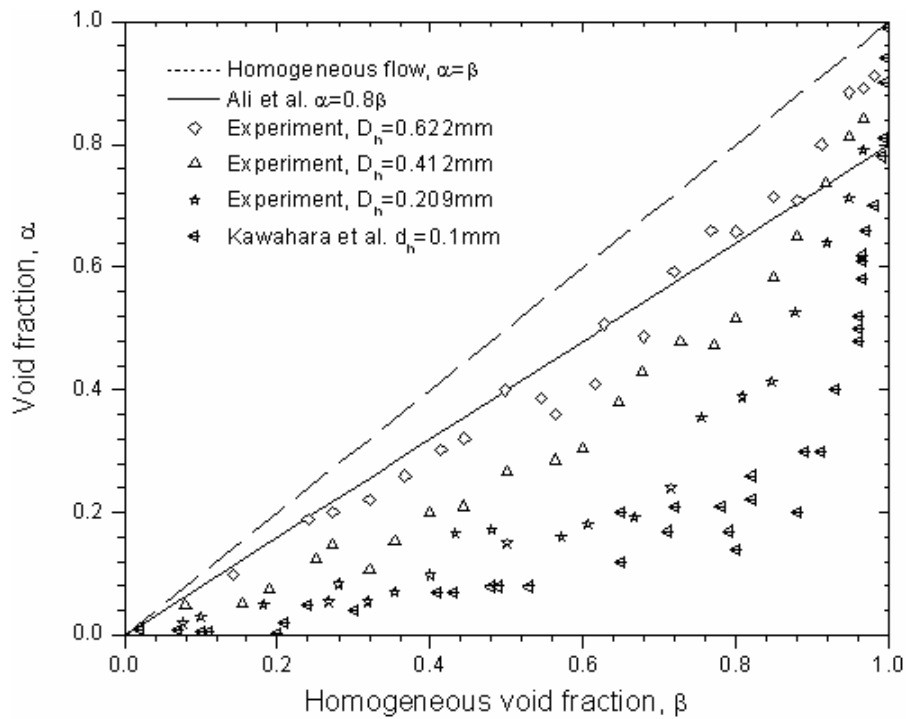


Figure 4-7. Measured time-averaged void fraction results vs two previous correlations

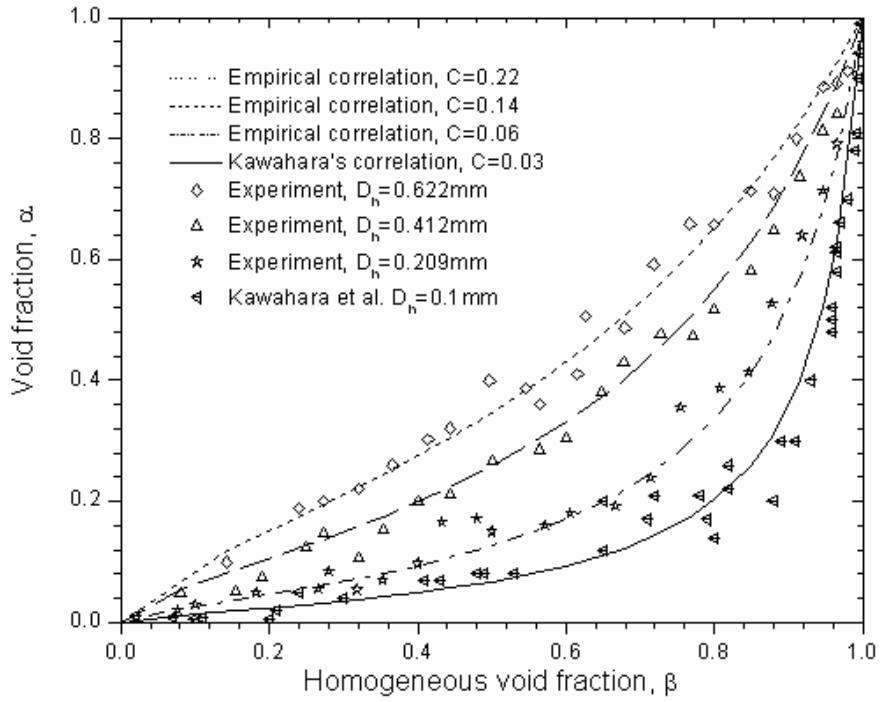


Figure 4-8. Comparison between the new correlation and experimental data

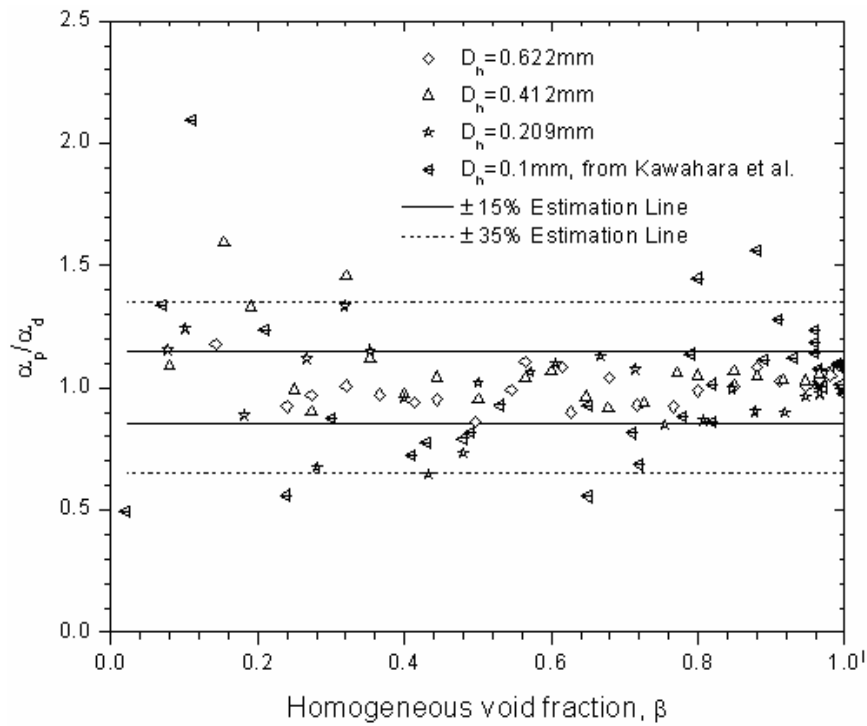
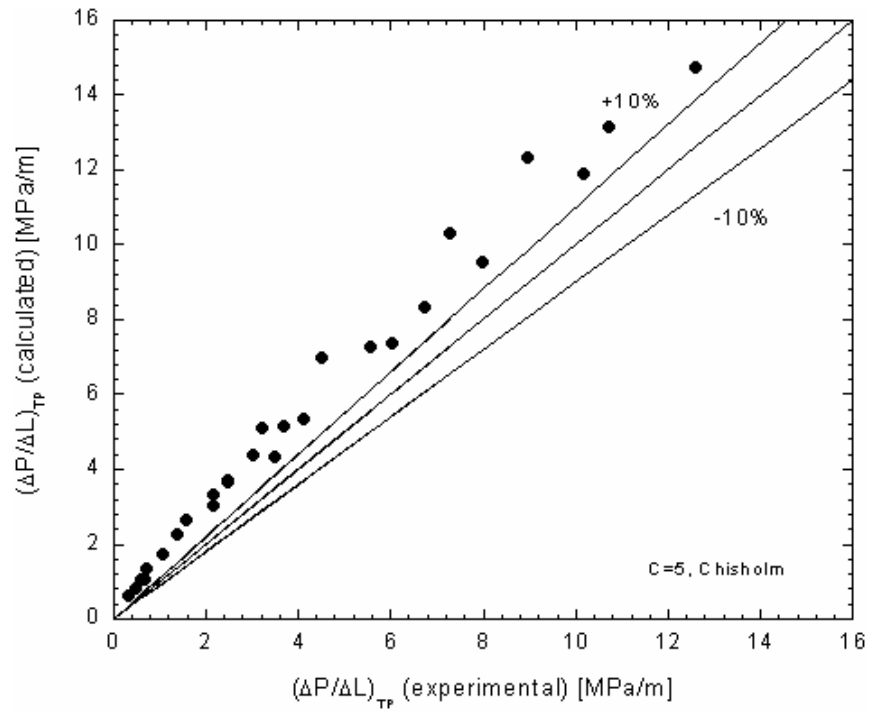


Figure 4-9. Ratio of predicted and experimental time-averaged void fraction vs. homogeneous void fraction β

A



B

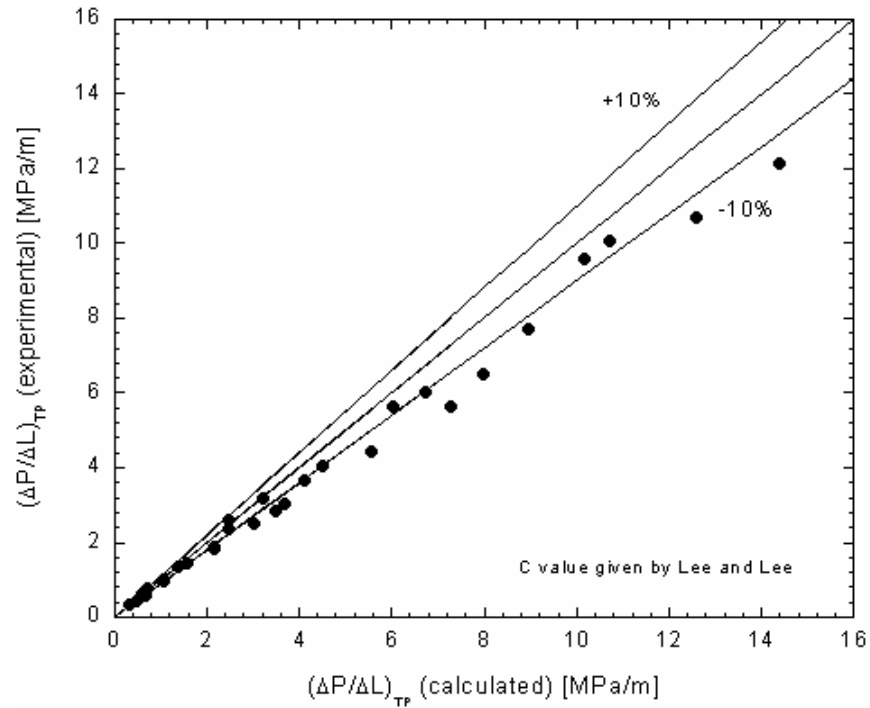


Figure 4-10. Comparison between the experimental data and the models ($D_h = 0.412$ mm) A) Lockhart-Martinelli's model ($C = 5$) B) Lee and Lee's model C) Mishima and Hibiki's model

C

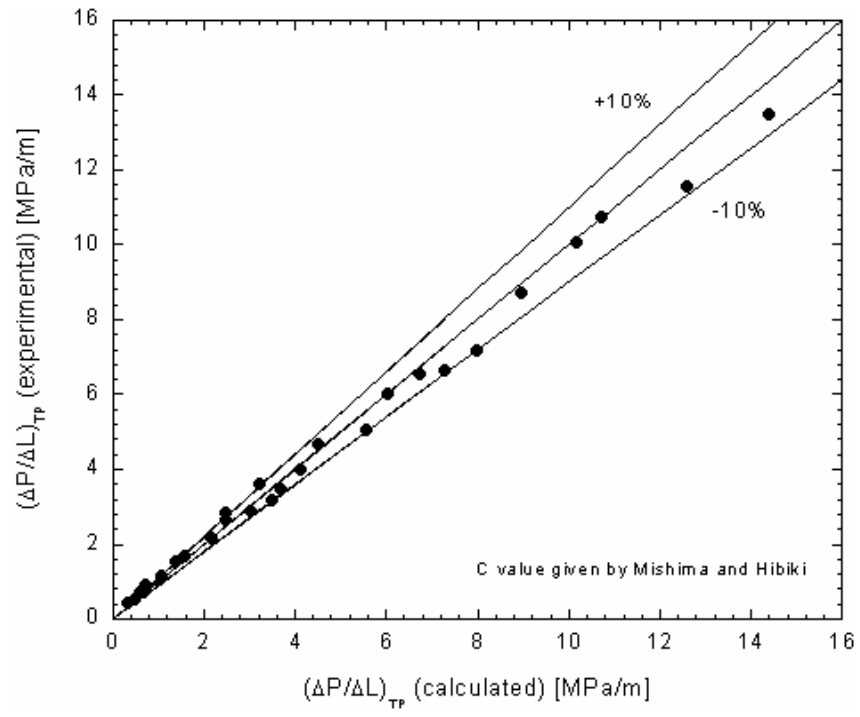


Figure 4-10. Continued

CHAPTER 5 MICRO-BUBBLE DISPENSER

Bubble generation in a simple co-flowing micro-channel with a cross-section area of $1.69 \times 0.07 \text{ mm}^2$ was experimentally and numerically investigated. Air and water were used as the gas and liquid, respectively. Mixtures of water-glycerol and water-Tween 20 were also used to obtain the effects of viscosity and surface tension. The experimental data shows that the break-up process is periodic under certain operating conditions. The break-up dynamics are also examined using three dimensional incompressible two-phase flow numerical simulation based on the volume of fluid (VOF) method. The simulation successfully predicts the flow behavior and provides a more detailed examination of the bubble shape. The physics can be further explained by the detailed micro-PIV measurements which show that the bubble is formed due to the velocity component perpendicular to the gas flow created by the sudden change of the liquid velocity distribution around the barrier. The bubble length L is dependent on the liquid flow rate Q_l and gas flow rate Q_g , and the ratio of L to the channel width w is a function of the ratio of gas and liquid flow rates Q_g/Q_l which is similar to that previously used in the T-junction case. The bubble frequency f is found to be related to w , channel depth h , and $Q_l Q_g / (Q_g + Q_l \cdot \pi/4)$. This formulation shows a good agreement with the experimental data at the low frequency region. Different bubble shapes can be obtained at different liquid viscosities and surface tensions. The ratio L/w can still be predicted by a modified equation which uses the real bubble width w_b or an equivalent bubble length L_e .

5.1 Introduction and Background

Single phase and multiphase flows in micro-geometries have been investigated by many researchers in recent years (Brutin and Tadrist 2003; Xiong and Chung, 2007a & 2007b). Microfluidic devices can be applied in many scientific and industrial developments such as

on-chip separation (Fu et al. 1999), chemical reaction (Song et al. 2003) and biochemical synthesis (Zheng et al. 2004). These devices require the control of small volumes of fluids, and the understanding of multiphase flows, especially with a special interest in formation of gas-liquid dispersions. Gas-liquid dispersion is common in macroscopic processes and products of the chemical, health-care, and food industries. Not surprisingly, many studies of emulsification and droplet behavior have been performed in macroscopic, unbounded shear, and extensional flows (Stone et al. 2004). Recent investigations focused on generating and manipulating emulsions with microfluidic devices are motivated by the potential to use controlled flows and structures on the scale of the droplets to tailor the properties of the emulsions. In particular, it's of interest to control the droplet size and the distribution of sizes. The microchannel geometry takes on added significance because it can influence the relative rate of rotation to extension in the flow, which is fundamental to break-up processes. Currently several techniques exist for the generation of bubbles (Ganan-Calvo and Gordillo 2001; Garstecki et al. 2004; Gordillo et al. 2004; Guillot and Colin 2005; Xu et al. 2006; Haverkamp et al. 2006). First is the T-junction. In the T-junction case, the continuous flow is in one arm and sheared off by a dispersion flow in the perpendicular arm. The break-up of gas-liquid threads is dominated by the pressure drop across the bubble as it forms, and the size of the bubbles is determined solely by the ratio of the volumetric flow rates of the two fluids. A scaling law for the size of the discrete fluid segments can be written as (Garstecki et al. 2006):

$$L/w = 1 + \alpha \frac{Q_g}{Q_l} \quad (5-1)$$

where L is the length of the bubble slug, w is the width of the channel, Q_g and Q_l are the gas and liquid flow rates respectively, and α is a constant of order one, whose particular value depends

on the geometry of the T-junction. Second is the flow-focusing device. The first type of the flow-focusing device arranges two channels in a concentric manner upstream of a small orifice to create a strong extensional flow (Stone et al. 2004). The bubble size is effectively set by the size of the orifice designed into the micro-channels under an operating condition while it can also produce threads that break into drops substantially smaller than the orifice in other cases. The second type uses a water nozzle and does not have an orifice. The bubble is formed in a co-flowing water jet discharging into a stagnant air atmosphere (Sevilla et al. 2005). Recently Cubaud et al. (2005) used a four-crossed square channel to generate the bubble. The results showed the breakup occurs at the intersection and the bubble size and distribution can be expressed by the same equation as Eq. (5-1) with $\alpha=1$. The empirical expression can well predict the bubble length when $0.1 < (Q_g + Q_l) / Q_l < 1$. For $(Q_g + Q_l) / Q_l < 0.04$, the flow becomes annular. The control of drop breakup in microdevices such as those mentioned above is influenced significantly by surfactants and wetting characteristics. For example, the continuous phase should be the phase that most strongly wets the boundaries. Contact angles and wetting properties depend on the type and concentration of surfactant, and such surfactant effects on drop formation in a T-junction have been investigated experimentally (Dreyfus et al. 2003), but have yet to be analyzed in detail; In addition, because shear rates can be large, new interfacial area is created rapidly. Thus, the kinetics, and possibly rheology, of surfactants may also play significant roles in the emulsion formation process.

In this paper, we describe a co-flowing device which is easy to be scaled up or multiplexed due to the simple structure. The objectives of this work are to 1) obtain the physics of the bubble break-up process, 2) discuss the flow parameters affecting the bubble length and get a

formulation of the bubble length, 3) analyze the bubble generation frequency, and 4) evaluate the effect of fluid viscosities and surface tension on bubble formation.

5.2 Experimental Setup

5.2.1 Dispenser Fabrication

The 3-D schematic of the co-flowing micro-channel is shown in Fig. 5-1(a). The micro-channel was made of glass and silicon fabricated in a clean room environment. The fabrication steps include a selective deep reactive ion etching of a double-sided polished silicon wafer. The inside barrier (splitter plate) can be made by first covering a photo-resist layer and then creating patterns with photolithography, leaving the barrier with a desired width and the gas and liquid channel exposed. Pyrex thin cover glass plate was anodic bonded on the top of the etched silicon wafer. Three larger holes are etched through the bottom of the wafer and glued with 1/16" soft tubes. In Fig. 5-1(b), w is the width of the main channel, w_g and w_l are the width of the gas and liquid channel respectively, d is width of the barrier, and h is the depth of the micro-channel. A microscope (Olympus BX50) and a CCD camera with a pixel size $6.45 \mu\text{m}$ were used to measure the dimensions of the micro-channel. The geometries are measured as: $w \approx 1.691 \text{ mm}$, $w_g = w_l \approx 0.545 \text{ mm}$, $d \approx 0.601 \text{ mm}$, and $h \approx 0.07 \text{ mm}$. The depth of the micro-channel was measured by the Veeco Wyko NT1000 optical profiler. Figure 5-2 shows the depth and 3-D image measured by the profiler.

5.2.2 Apparatus

Fig. 5-3 shows the schematic of the experimental flow visualization apparatus used to investigate the bubble dispersion in the co-flowing micro-channel. It includes two syringe infusion pumps (Cole-Parmer Instrument), 60ml and 3ml syringes (McMaster), micro-filter (Swagelok), Fiber-Lite MI-150 high intensity illuminator (Dolan-Jenner), micro-channels, and

high speed CCD camera (Redlake). The liquid fluid at flow rates ranging from 3ml/h to 63ml/h, which can be set on the panel of the infusion pump with an accuracy of $\pm 0.5\%$, was driven to the micro-channel test section. The 2 μm micro-filter can remove any particles or bubbles which may block the micro-channel before the flow enters into the test section. The gas flow at flow rates ranging from 0.21ml/h to 126ml/h was driven to the channel from the other syringe pump. The test sections were placed horizontally. All experiments were conducted at room temperature, 20°C, and under atmospheric pressure at the discharge of the test section. Flow visualization was started after some equilibration time when changing the flow parameters. It was achieved by using a high speed CCD camera, which can operate at a frame rate up to 8000 fps and a shutter speed of 1/8,000 s. In this work, the frame rate of 500 fps was used. The resolution of the camera was 480(H) \times 420(V) pixels. Two Fiber-Lite illuminators provided the high intensity light, which was directed onto the test section by two optical fiber light guides. An adjustable microscopic magnification lens was used to magnify the test section.

In this experiment, the air was used as the gas fluid. Water (viscosity $\mu=0.92$ mPa·s) and three aqueous solutions of glycerol, 50% (w/w) glycerol ($\mu=7.31$ mPa·s), 30% (w/w) glycerol ($\mu=2.68$ mPa·s), and 10% (w/w) glycerol ($\mu=1.19$ mPa·s) were used as the liquid fluid. The viscosity of water-glycerol mixture was measured at room temperature, 20°C, by means of a rotary viscosimeter. To change the gas-liquid interfacial tension and evaluate its effect to bubble generation, 2% (w/w) Tween-20 surfactant is added into the water and mixed for approximately 40 minutes at room temperature. The dilute solution of Tween-20, 2% (w/w), is larger than the critical micellar concentration (CMC) in water, 0.007% (0.059mM). The surface tension measured by a digital tensiometer changes from around 72mN/m (water + air) to 37mN/m (water/Tween-20 + air). It has to be pointed out that small change in temperature [$\sim O(10)\text{K}$] and

composition can result in 5% variation around the measured values. Image analysis software ImagJ was used to analyze the image frames to determine the bubble size.

To further understand the break-up physics, a micron-resolution particle image velocimetry system (micro-PIV), shown in Fig. 5-4, was used where fluorescent particles (Duke Scientific) were seeded into the de-ionized water flow. Two Nd:YAG lasers (Continuum) were directed to the same optical path by optical lenses (Edmund) and expanded by a beam expander made up of a concave and a convex lens. The 0.69 μm particles absorb green light ($\sim 542\text{nm}$) and emit red light ($\sim 612\text{nm}$). The emitted light is imaged through a 10 \times objectives lens (NA=0.3) and passed to the fluorescent filter cube (Olympus), where the green light from the background reflection is filtered out and the red fluorescence from the sub-micron particles is passed to the 0.5 \times lens (Olympus) and recorded on the CCD camera (Cooke). The concentration of the fluorescent particles solution was prepared to ensure at least 5-10 seed particles in each interrogation volume. In this work, this time delay is set to be 100 μs , so the particles move approximately 1/8th of an interrogation window between pulses. The interrogation windows measure 64 camera pixels square, thus the particles moves approximately 8 pixels between laser pulses. Assume that the measured velocity is accurate to within 1/5th of a pixel. It results in an experimental uncertainty of less than $\pm 2.5\%$ (Prasad *et al* 1992).

5.3 Numerical Simulation

The numerical simulation presented here is used to examine the bubble dynamics in the break-up process. Since the simulation includes two fluids and time dependent bubble motion, the Volume of Fluid (VOF) method is applied. The main purpose of the VOF method is to track the interface between two phases. That is accomplished by solving the continuity equation for

volume fraction of phases at the interface. Suppose there are n phases, and for the i th phase, the continuity equation at interface is in the form of:

$$\frac{\partial}{\partial t}(\alpha_i \rho_i) + \nabla \cdot (\alpha_i \rho_i \vec{v}_i) = \sum_{j=1}^n (\dot{m}_{ji} - \dot{m}_{ij}) \quad (5-2)$$

α_i is the volume fraction of the i th fluid in the cell, ρ_i is density of i th fluid, \vec{v}_i is the velocity vector of the i th fluid, n is the total number of phases, \dot{m}_{ji} is mass transfer from phase j to phase i . For every non-primary phase, Eq. (5-2) will be solved. For the primary phase, its volume fraction is calculated by:

$$\sum_{j=1}^n \alpha_j = 1 \quad (5-3)$$

In this simulation, the primary phase is set to be water and air is the secondary phase. The Navier-Stokes equations are discretized on a standard marker and cell (MAC) grid with velocities on cell walls and the rest of the properties at the cell centers. A QUICK discretization scheme is used for the convective terms and a second order discretization scheme is used for the viscous terms. The simulation mesh is shown in Fig. 5-5. The total number of cells is about 220000. The width and depth of the simulation region are the same with the device used in the experiment, which are 1.691 mm and 0.07 mm, respectively. In the length direction, only a portion of the micro-channel is simulated in order to reduce the computational time. The lengths of air and water inlets are set to be 1 mm and the total simulation region is 10 mm long. This computation region is where an air bubble is generated and breaks up. Thus it can capture the main physical phenomena.

5.4 Results and Discussions

5.4.1 Bubble Break-Up

The bubble generation process can be observed from a video recorded by the high speed camera. Fig. 5-6 shows the time evolution of a periodic break-up procedure and the corresponding bubble shape prediction by the simulation. In the simulation results, blue denotes pure liquid with void fraction of zero and red denotes pure gas with void fraction of one.

During a typical period, there are two steps in the process. Firstly, after the pinch-off of a bubble, the gas ligament expands vertically downward and horizontally until a neck appears. Since the top interface is bounded by the channel, the ligament only develops downward vertically. This period t_e from the pinch-off to the neck appearing is called the gas ligament expansion. After the ligament expansion, the neck propagates downstream and its diameter decreases until it finally breaks, thereby forming a new leaving bubble. The newly formed bubble is immediately bounded as a gas slug due to the high surface tension force in the small channel. This period t_c from the neck appearing to the formation of the new bubble is named the gas ligament collapse. From the last image, we can see the next periodic break-up sequence begins. From the Young-Laplace equation, the Laplace pressure jump across the interface equals to $\sigma(1/r_a+1/r_r)$ where r_a and r_r are the axial and radial radii of curvature, respectively. Both of them are proportional to the corresponding wetting angles which are varying with time, but they are bounded by the width w and height h of the channel, respectively. Since $w \gg h$ in our channel and r_r is minimum at the moment of break-up, the maximum Laplace pressure jump almost equals to σ/r_{\min} . If the total pressure difference between gas and liquid exceeds the maximum Laplace pressure jump, bubble break-up would take place. Otherwise no break-up exists.

The experiment data show that the periodic break-up only exists under certain operating conditions. There are two typical unsteady break-up processes in the experiment, which are shown in Fig. 5-7. The first one, shown in Fig. 5-7a), is the case where the liquid flow rate is so low that the neck can not be broken before the gas ligament flows out the channel. The second one, shown in Fig. 5-7b) and 5-7c), is the case where the ratio of gas and liquid flow rates is so high that the neck is stretched to a very thin gas ligament no matter what the flow rate is, intermediate or high.

Fig. 5-8 shows the instantaneous micro-PIV measurements in one period around the barrier. From Fig. 5-8, we can see that when the liquid enters into the main channel from the liquid sub-channel, it pushes upward due to its larger momentum. As a result, velocity components perpendicular to the gas ligament exist around the barrier which press the bubble interface and form the neck. After the break-up, the high liquid velocity on the top of the bubble pushes it to the bottom wall and forms a gas slug (Fig. 5-8e), then a new periodic cycle begins.

5.4.2 Bubble Distribution and Bubble Size

Over a wide range of gas and liquid flow rates, the bubbles are generated uniformly. Fig. 5-9 shows the uniform bubble distribution near the exit of the channel at different gas and liquid flow rate ratios. Assume that D denotes the distance between the two consecutive bubbles. The bubble length L increases while D decreases with the flow rate ratio.

Changing the gas and liquid flow rates can achieve different bubble lengths. Fig. 5-10 shows the dependence of bubble length L on the gas and liquid flow rates. From Fig. 5-10a) it was found at a fixed liquid flow rate, the bubble length increases with the gas flow rate. That's because with a higher flow rate the gas has a larger force to push the liquid and resist the liquid pressure at the neck, so both of the expansion and collapse time t_e and t_c increase which leads to a longer bubble. While from Fig. 5-10b) we can see at a fixed gas flow rate, L decreases with the

liquid flow rate. The same physics can be applied here. The increasing liquid momentum cuts the neck quickly and shortens the time of both stages which results in a bubble with a short length.

Fig. 5-11 shows the data of L/w at the gas-liquid flow rate ratio ranging from 0.01 – 2 with one gas flow rate 5ml/h and three different liquid flow rates chosen as 21ml/h, 42ml/h, and 63ml/h respectively. It was found that under current experimental conditions, except for the high gas to liquid ratio data shown as the hollow triangles in the figure where the gas flow rate was kept constant at $Q_g = 5\text{ml/h}$, the rest of the data can be correlated successfully by Eq. (5-1) with $\alpha = 1$, which is based on fitting with the experimental data in a T-channel which is shown as the solid line in Fig. 5-11 and expressed as:

$$L/w = 1 + \frac{Q_g}{Q_l} \quad (5-4)$$

The reason why the hollow triangle data deviate from Eq. (5-4) is given as follows: From Fig. 5-8, we know that the bubble break-up physics is similar to that in a T-junction as the bubble break-up requires a vertical liquid velocity component to pinch off the neck. Oak et al. (2004) demonstrated that in the co-flowing micro-channel, when the liquid flow rate is increased, around the barrier there is a correspondingly higher vertical component that is used to form the bubble. So when the liquid flow rate is larger than the critical value, the flow dynamics is almost identical to the T-junction case. When the liquid flow rate is less than the critical value, only a portion of the liquid velocity is used in the bubble formation, which lowers the effectiveness of Q_b . As a result, the L/W is increased from that predicted by Eq. (5-4).

5.4.3 Bubble Frequency

For the macro channel, the bubble velocity is related with the mixture mean velocity $U_g + U_l$ and the mean drift velocity U_{gl} , which can be given by (Zuber and Findlay 1965):

$$U = C_0(U_G + U_l) + U_{gl} \quad (5-5)$$

C_0 is the distribution parameter. The mean drift velocity U_{gl} can be neglected in micro-channels due to the inability of the bubbles to rise through the stagnant liquid (Ali et al. 1993) and Cubaud et al. (2005) found $C_0 \approx 1$ in micro-channels. Hence

$$U = \frac{Q_l + Q_g}{w \cdot h} \quad (5-6)$$

Assume T is the total time of formation of one bubble, then

$$D = UT = U(t_e + t_c) \quad (5-7)$$

Assume the left and right side of the bubble is nearly spherical and the small volume of the film thickness ($\sim 1\%-3\%$ of the total bubble volume from the image) can be neglected, then the gas volume in a bubble is approximately estimated to be $((L-w) \cdot w + \pi \cdot w^2/4) \cdot h$. According to the mass conversation, the relationship between L and D can be written as

$$\frac{Q_l}{Q_g} = \frac{(D-L)w + \left(1 - \frac{\pi}{4}\right)w^2}{Lw - \left(1 - \frac{\pi}{4}\right)w^2} = \frac{D-L + \left(1 - \frac{\pi}{4}\right)w}{L - \left(1 - \frac{\pi}{4}\right)w} \quad (5-8)$$

Combine Eqs. (5-4) - (5-8), and the bubble frequency can be calculated as:

$$fre = \frac{1}{T} = \frac{1}{t_e + t_c} = \frac{Q_l Q_g}{w^2 h \left(Q_g + Q_l \cdot \frac{\pi}{4} \right)} \quad (5-9)$$

Fig. 5-12 shows the experimental bubble frequencies and the theoretical one expressed by Eq. (5-9). The experimental values are calculated by checking the video and getting the time of bubble formation in one period. From Fig. 5-12, we can see the experimental data agree well with the predicted one at the low frequency region. But there is an underestimation at the high

frequency region since in this region the gas flow rate is high and the bubble shape at the interface shows an elliptical shape. When Eq. (5-8) is applied, the gas volume is underestimated which results in the underestimation of frequency.

5.4.4 Effect of Viscosity and Surface Tension

Mixtures of water-glycerol and water-Tween 20 were used to obtain the effects of viscosity and surface tension on the bubble generation respectively. The recorded data shows that the bubble formation still can be steady and periodic as the pure water under the same operating conditions. However, we have found some changes on the bubble shapes at different viscosities and surface tensions. Fig. 5-13 shows the bubble shapes with different viscosities and surface tensions at $Q_L = 21\text{ml/h}$ and $Q_L = 42\text{ml/h}$. With the increasing of the viscosity, the film thickness is obviously increased. A typical example is that the bubble shape changes from a slug to an approximately spherical bubble at the lower Q_g/Q_L . At this time, we can not use the channel width w to be the bubble width w_b . Hence a modified equation can be obtained by using w_b to replace w in Eq. (5-4). Fig. 5-14 shows the measured L/w_b at different ratios of gas to liquid flow rate. The experimental data shows a good agreement with the ones predicted by the modified equation. If w was still used here, the bubble length would be overestimated by around 6%, 18.7%, and 31.2% respectively. From Fig. 5-13, we also see the bubble changes to a tadpole-like shape due to the decrease of surface tension. The tail of the bubble decreases with gas and liquid flow rates. The reason may be at the interface that the increasing inertia forces push and shorten the tail. To compare the bubble length with the former results, we define an equivalent bubble length L_e for the tadpole-like bubbles, which can be approximately calculated by:

$$L_e = \frac{A_b}{w} = \frac{\text{Pixels covered by the bubble area}}{\text{Pixels covered by the channel width}} \quad (5-10)$$

where A_b is the bubble area obtained from the flow image. It is the area enclosed by the bubble interface. This interface can be detected by an image processing function in the commercial software ImageJ, Edge Detection Function, which uses the gradient of the pixel values around the interface to detect it. Fig. 5-15 shows the L_e/w at different surface tensions. The data also have a good agreement with the predict ones. The conclusion can be made that under current operating conditions, the bubble length can still be predicted by a modified equation which uses the real bubble width w_b or an equivalent bubble length L_e . Fluid viscosity and surface tension have a major effect on the bubble shape.

5.4 Summary

In this chapter, we experimentally and numerically investigated the formation of bubbles in a simple co-flowing micro-channel, which has a compact size to be easily scaled up or multiplexed and can generate micro-bubbles roughly from 0.1 μL to 0.6 μL under current operating conditions. The break-up process, bubble length, bubble frequency, and effects of viscosity and surface tension were comprehensively studied. The following conclusions can be made:

- Bubble break-up is obtained by the velocity distribution change around the barrier. It is periodic under certain operating conditions, and it becomes unsteady and nonperiodic when Q_l is less than some critical values or Q_g/Q_l is too large. The process has two steps: gas ligament expansion and collapse.
- The bubble length L is dependent on Q_g and Q_l , and has a quantitative relationship with channel width w and Q_g/Q_l , which is the same as that used for the T-junction since the break-up process becomes similar with that of T-junction under the operating conditions.
- At the low frequency region, bubble generation frequency is a function of channel width w , channel depth h and $Q_l Q_g / (Q_g + Q_l \cdot \pi/4)$. This functional relationship provides a very good prediction at the low frequency region.
- The liquid viscosity affects the film thickness while the surface tension changes the bubble shape. The dimensionless bubble length L/w can still be predicted by a modified equation which uses the real bubble width w_b or an equivalent bubble length L_e .

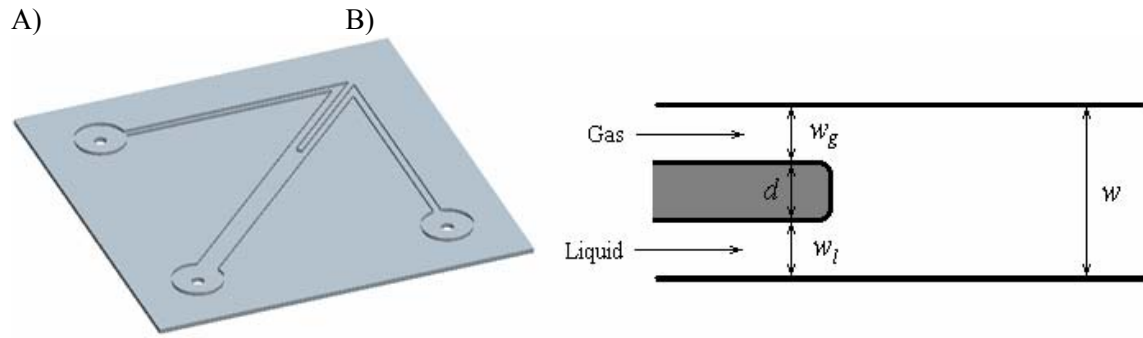


Figure 5-1. Schematic of the co-flowing micro-channel: A) 3-D and B) 2-D

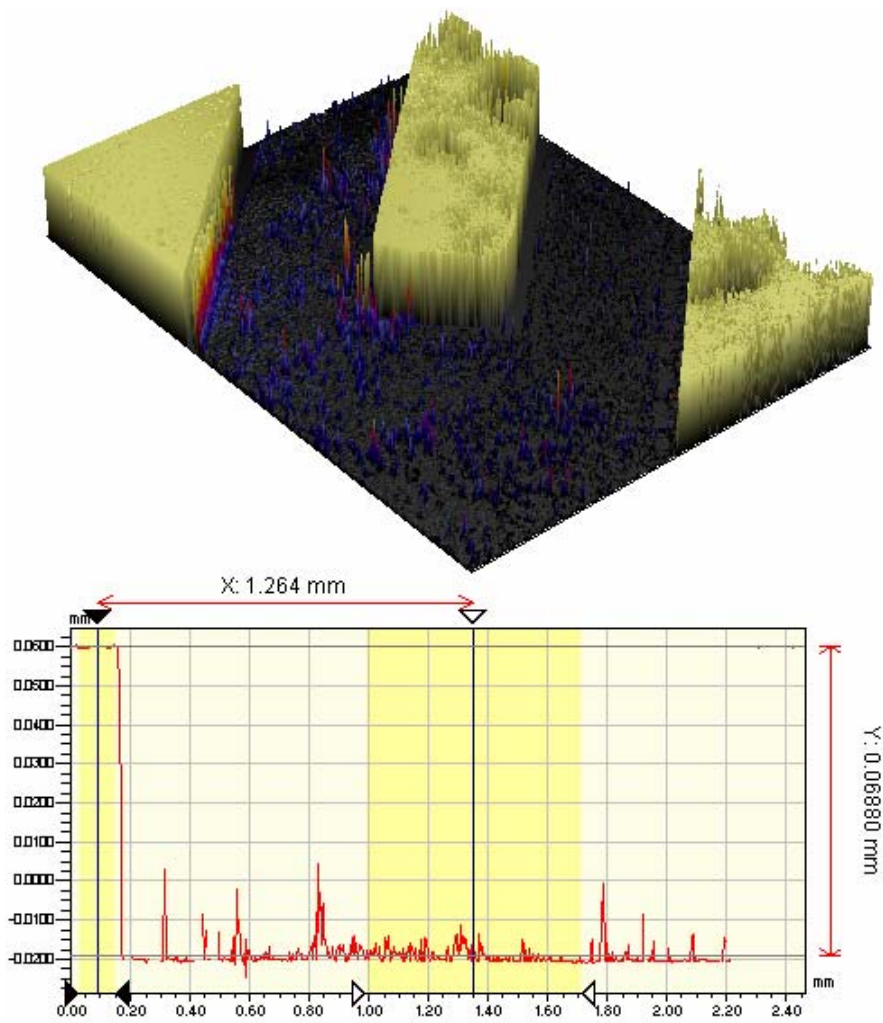


Figure 5-2. 3-D image and depth measurement by the optical profiler

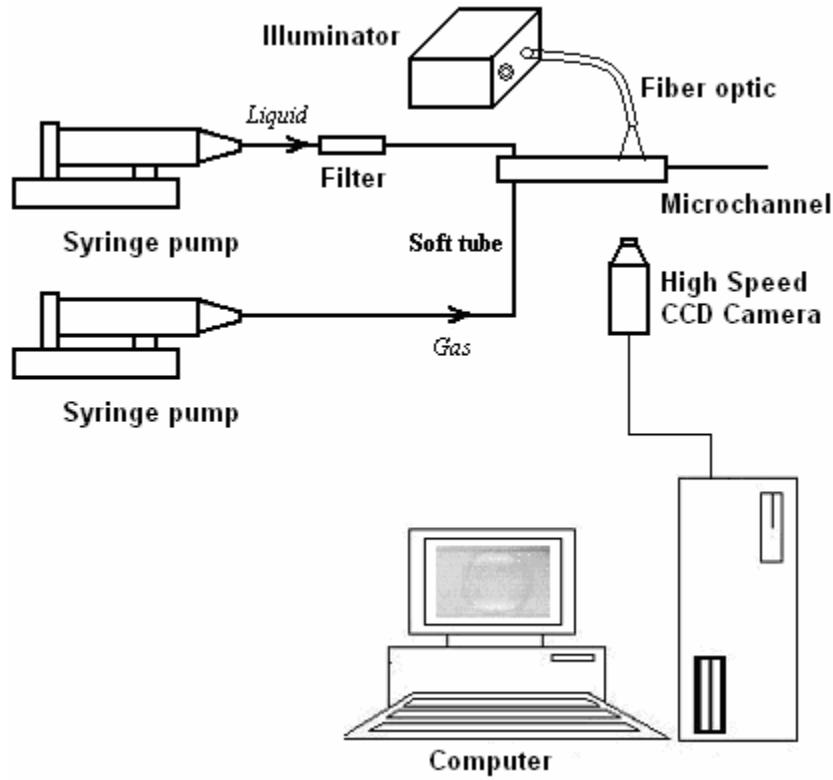


Figure 5-3. Schematic of the experimental flow visualization apparatus

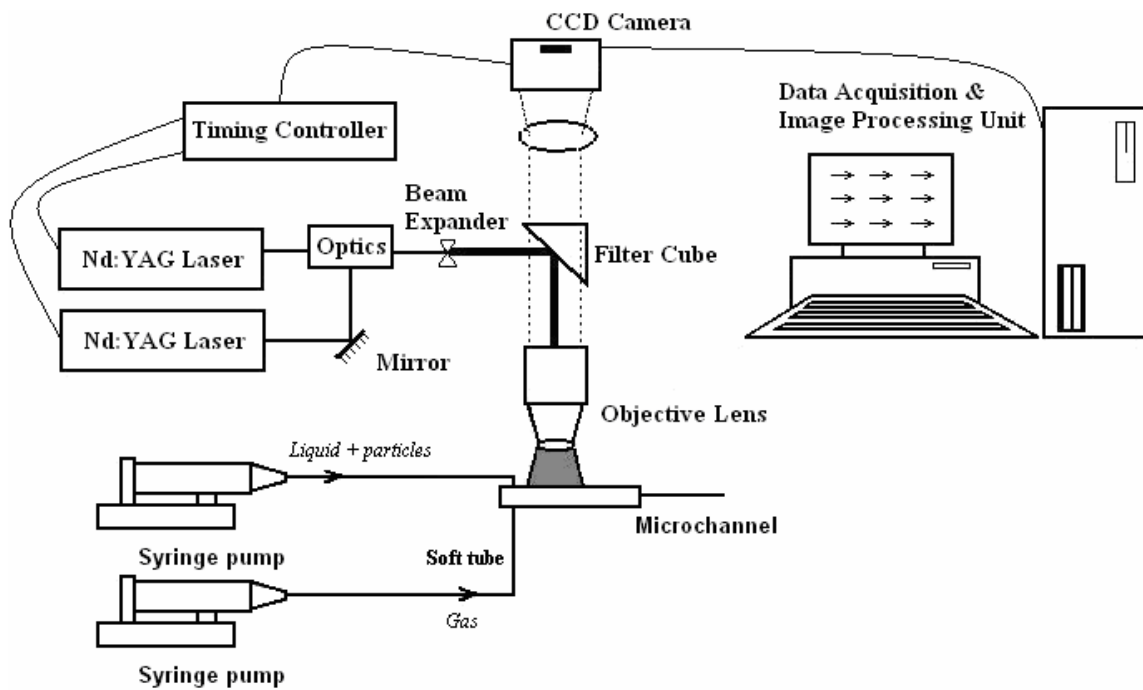


Figure 5-4. Schematic of micro-PIV measurement for micro-bubble dispenser

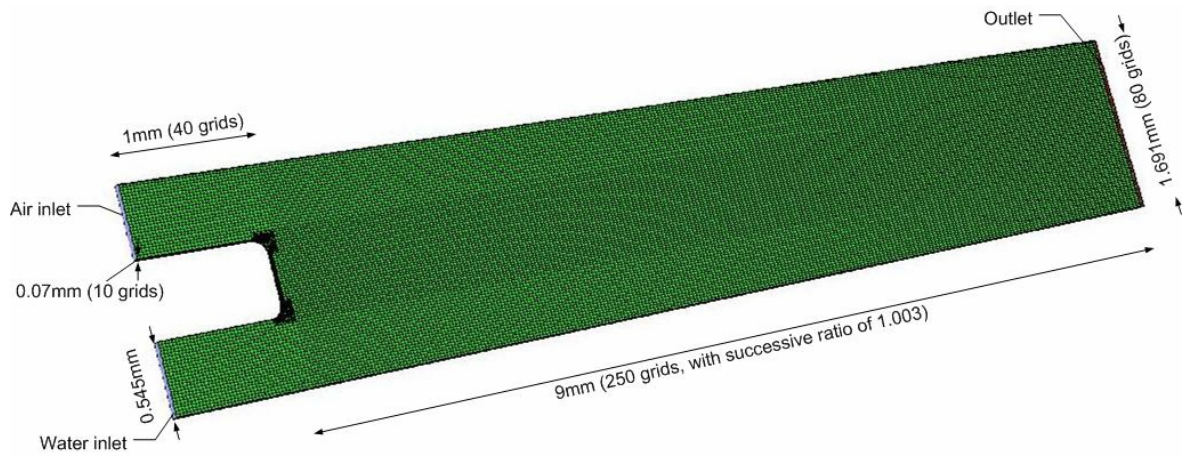


Figure 5-5. Schematic of 3D CFD mesh

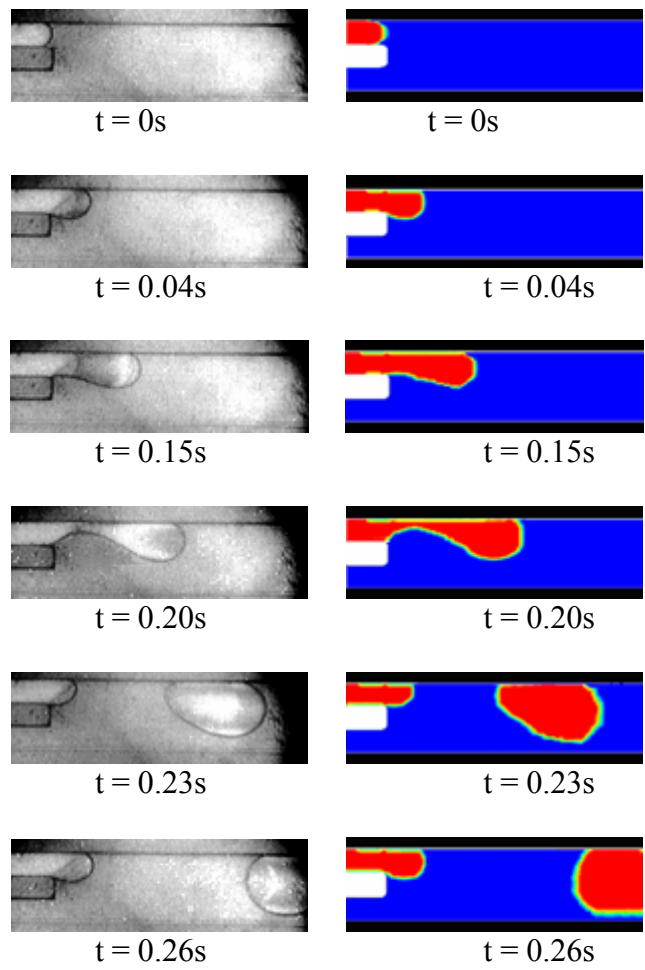


Figure 5-6. Time evolution of the periodic bubble generation process ($Q_g = 6.3\text{ml/h}$, $Q_l = 21\text{ml/h}$, Air+Water) and the prediction by CFD simulation



Figure 5-7. Unsteady break-up process at different flow rates: A) $Q_g = 2.4\text{ml/h}$, $Q_l = 3\text{ml/h}$ B) $Q_g = 105\text{ml/h}$, $Q_l = 42\text{ml/h}$ and C) $Q_g = 37.5\text{ml/h}$, $Q_l = 15\text{ml/h}$

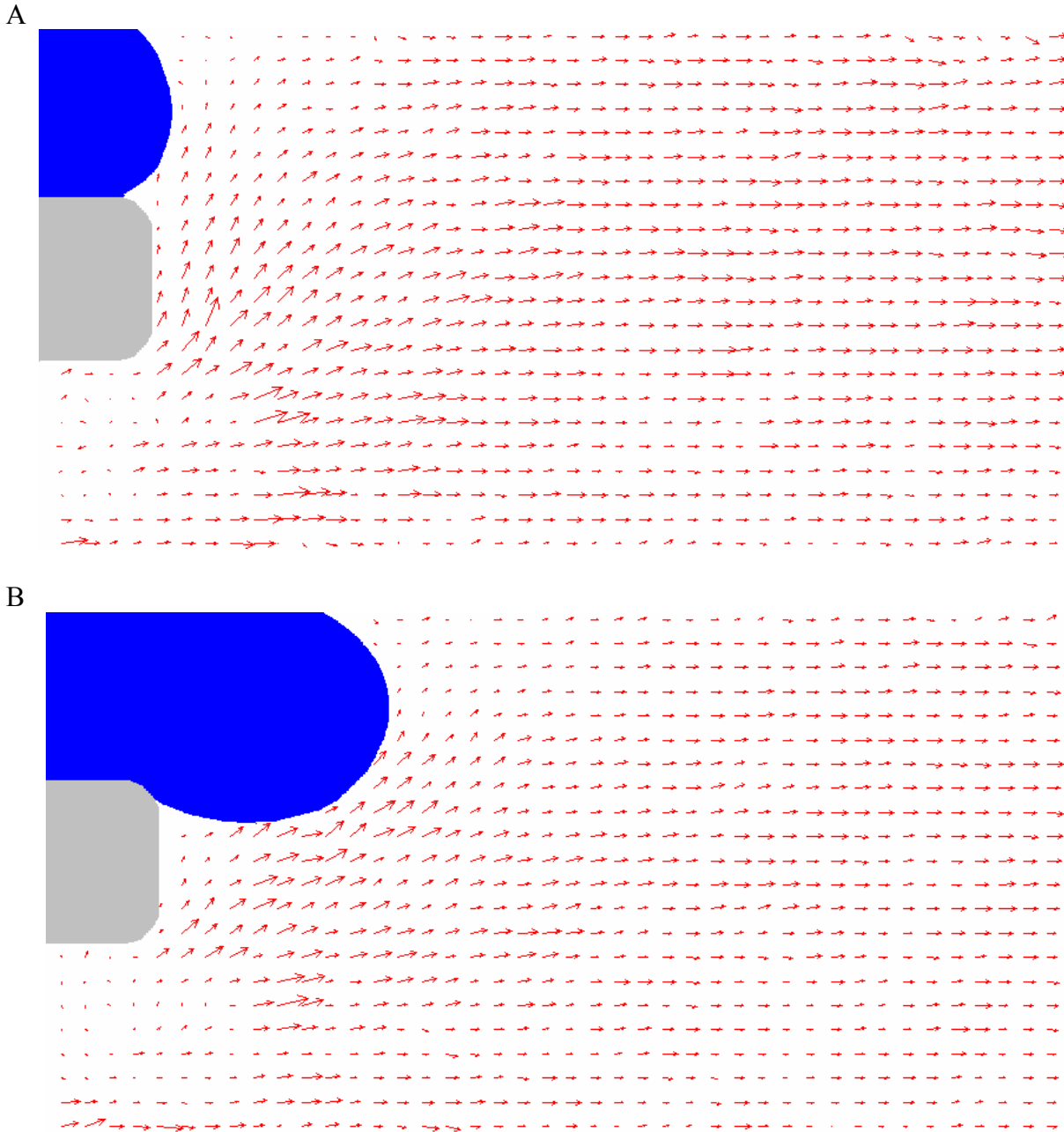
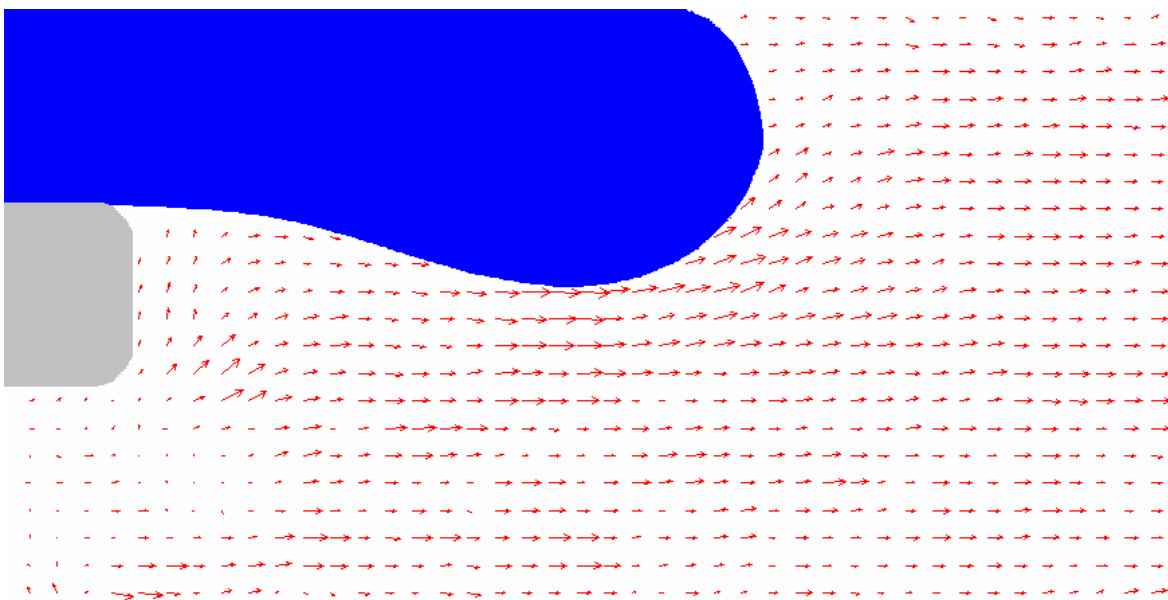


Figure 5-8. Instantaneous micro-PIV measurements around the barrier ($Q_l = 21\text{ml/h}$, $Q_g = 6.3\text{ml/h}$)

C



D

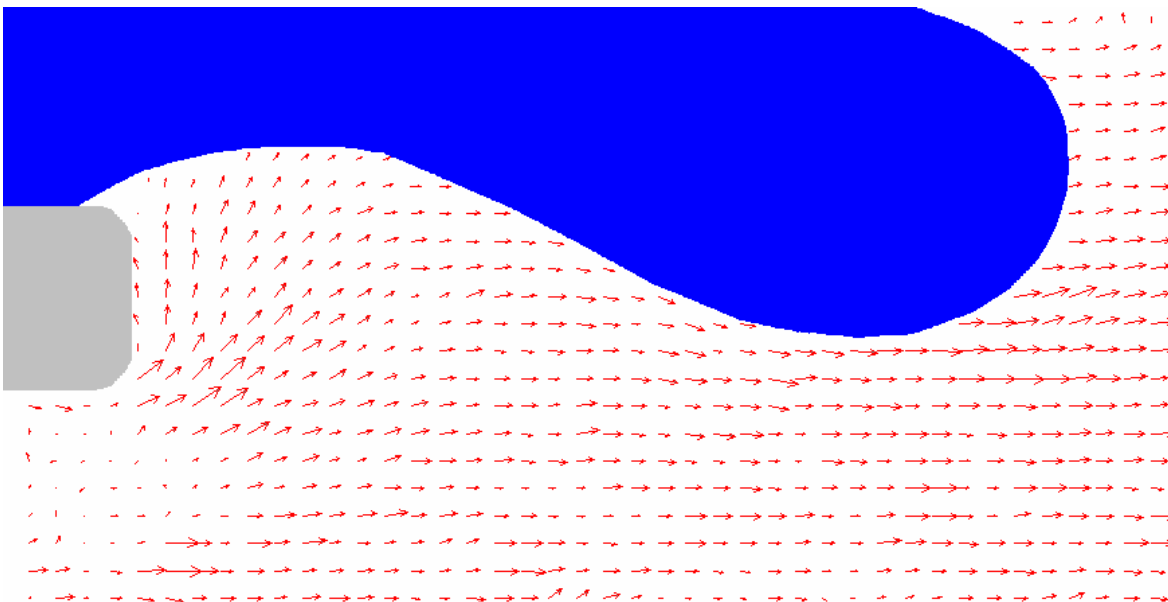
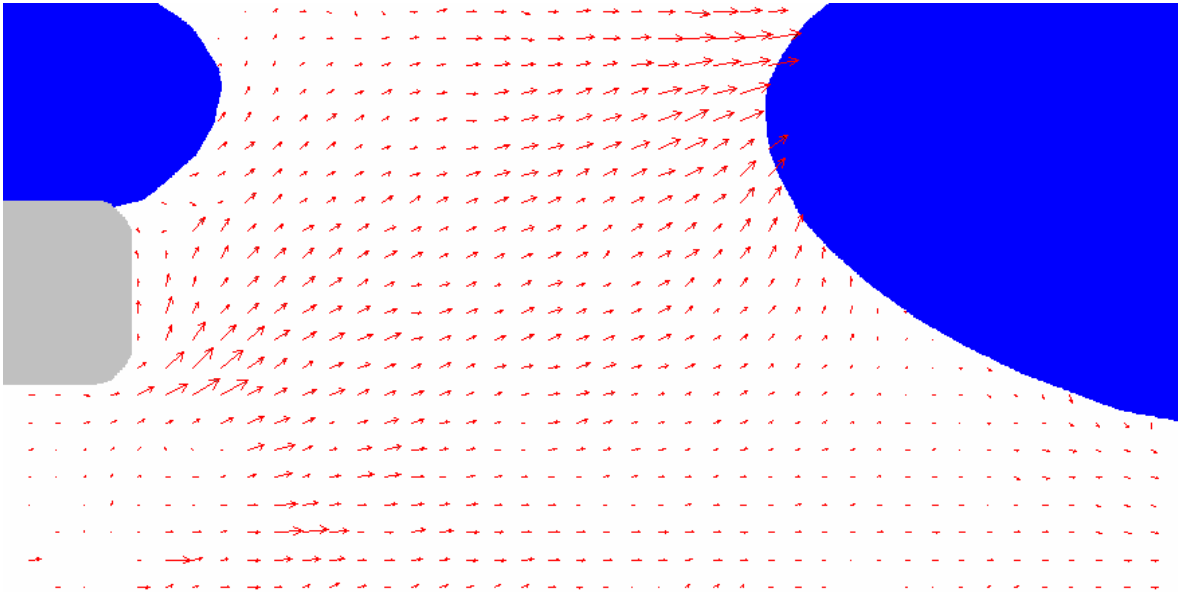


Figure 5-8. Continued

E



F

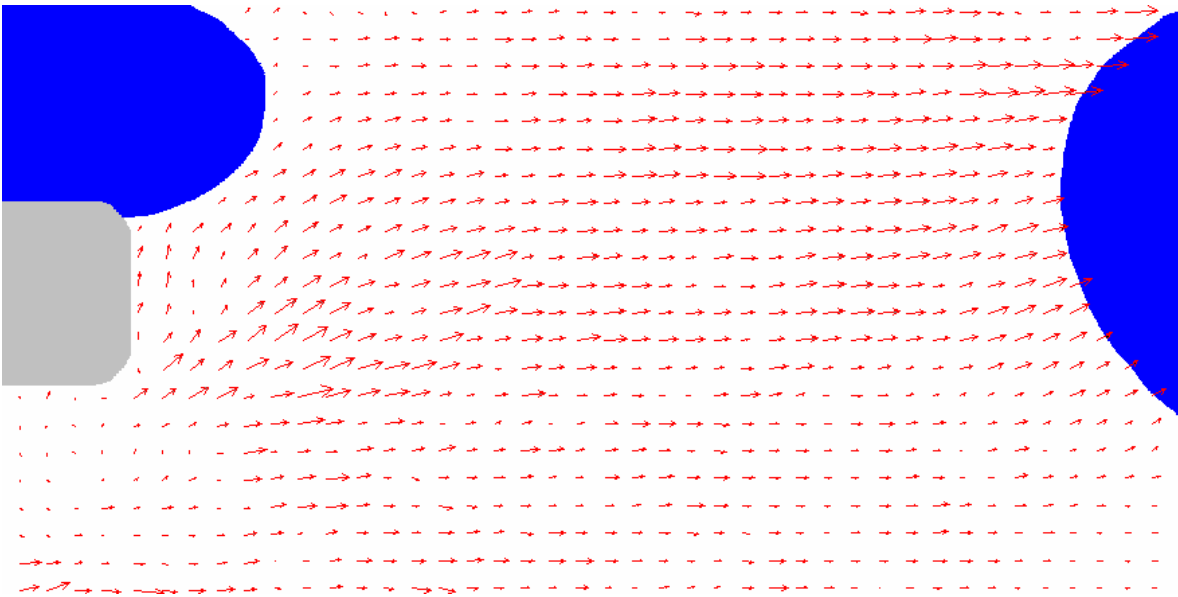


Figure 5-8. Continued

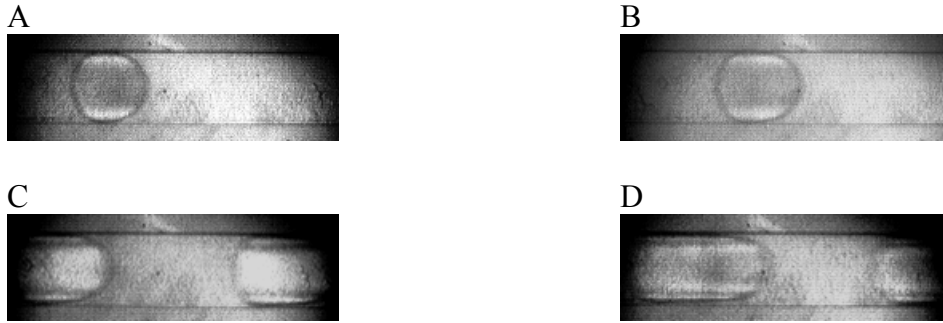


Figure 5-9. Bubble distribution along the channel at different flow rates: A) $Q_g/Q_l = 0.01$ ($Q_l = 21\text{ml/h}$, $Q_g = 0.21\text{ml/h}$) B) $Q_g/Q_l = 0.1$ ($Q_l = 21\text{ml/h}$, $Q_g = 2.1\text{ml/h}$) C) $Q_g/Q_l = 0.5$ ($Q_l = 21\text{ml/h}$, $Q_g = 10.5\text{ml/h}$) D) $Q_g/Q_l = 1$ ($Q_l = 21\text{ml/h}$, $Q_g = 21\text{ml/h}$)

A

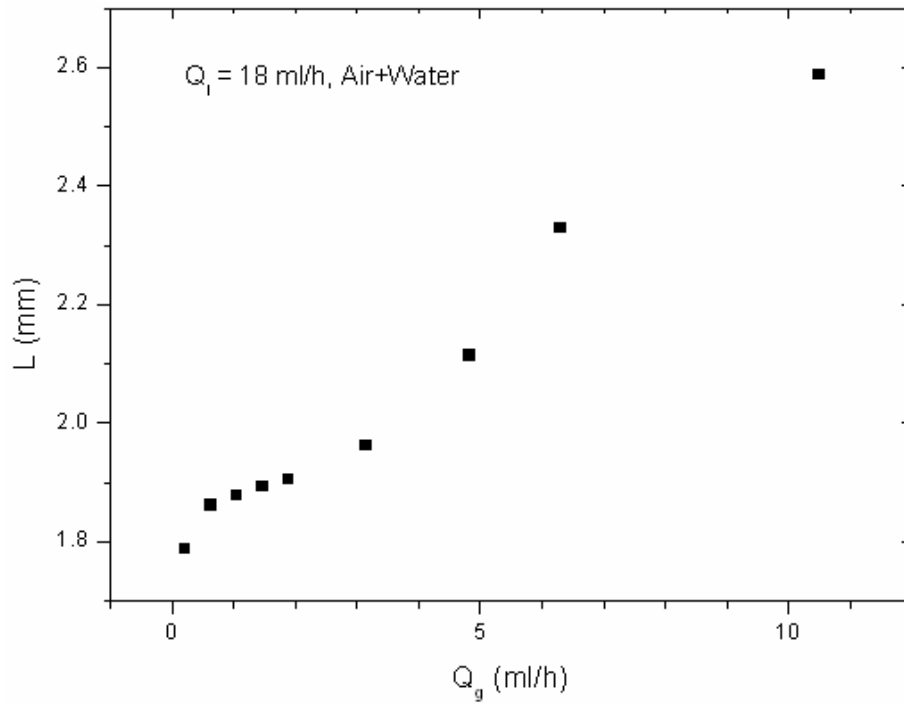


Figure 5-10. Dependence of the bubble length L on the A) gas flow rate ($Q_l = 18\text{ml/h}$) and B) liquid flow rate ($Q_g = 5\text{ml/h}$)

B

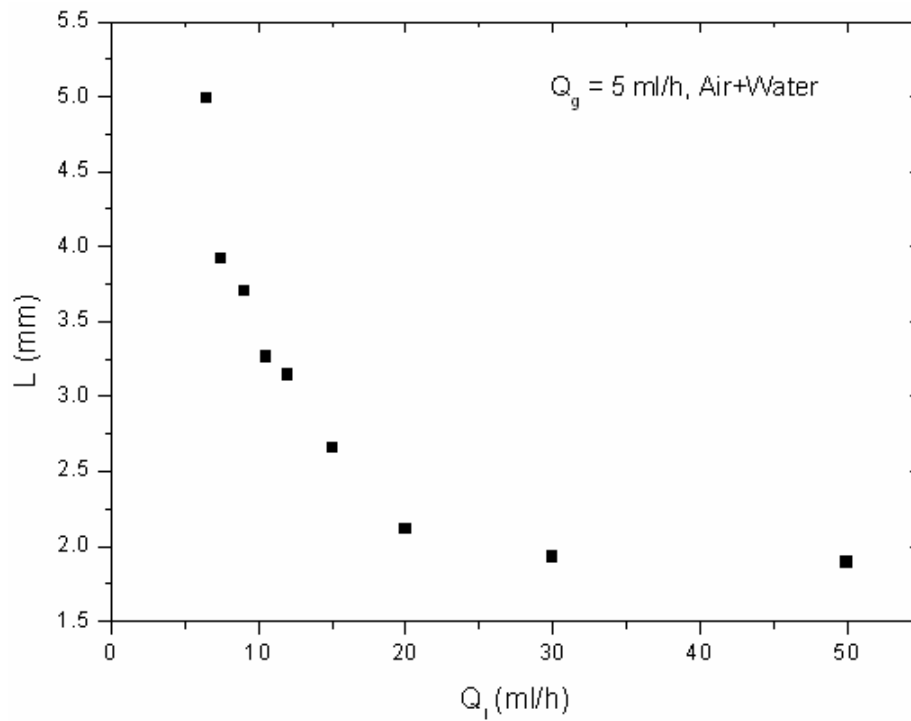


Figure 5-10. Continued

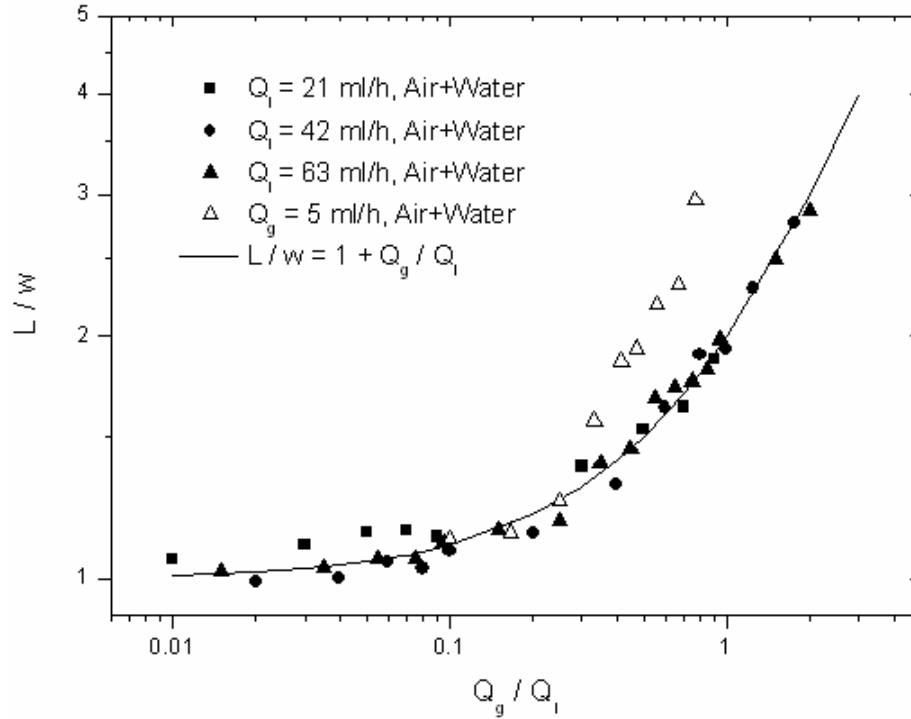


Figure 5-11. Dimensionless ratio (L/w) with the ratio of gas and liquid flow rates

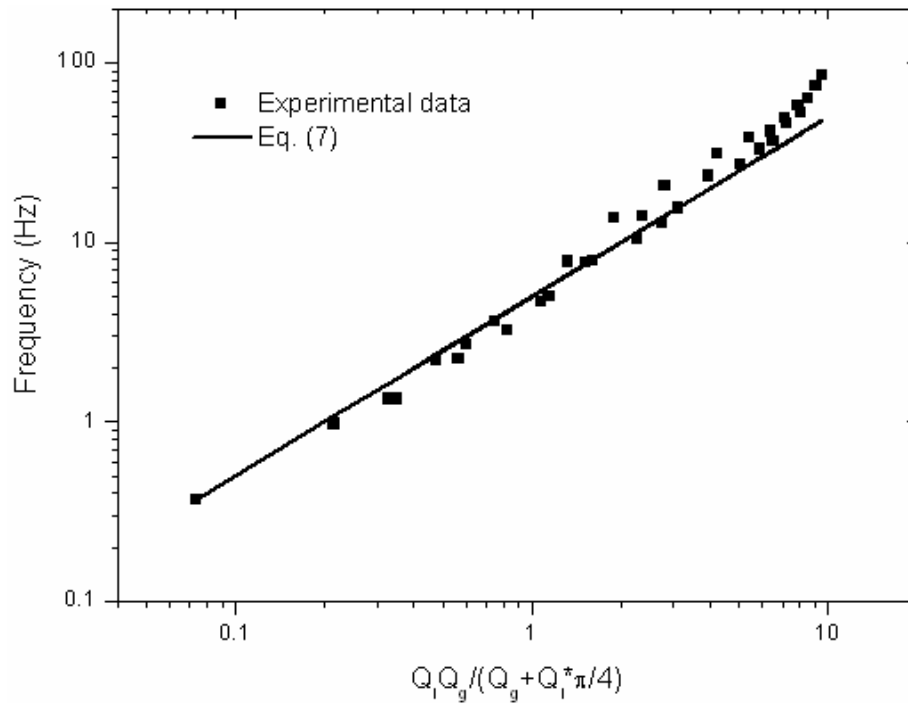


Figure 5-12. Bubble frequency with different liquid and gas flow rates (Air +water)

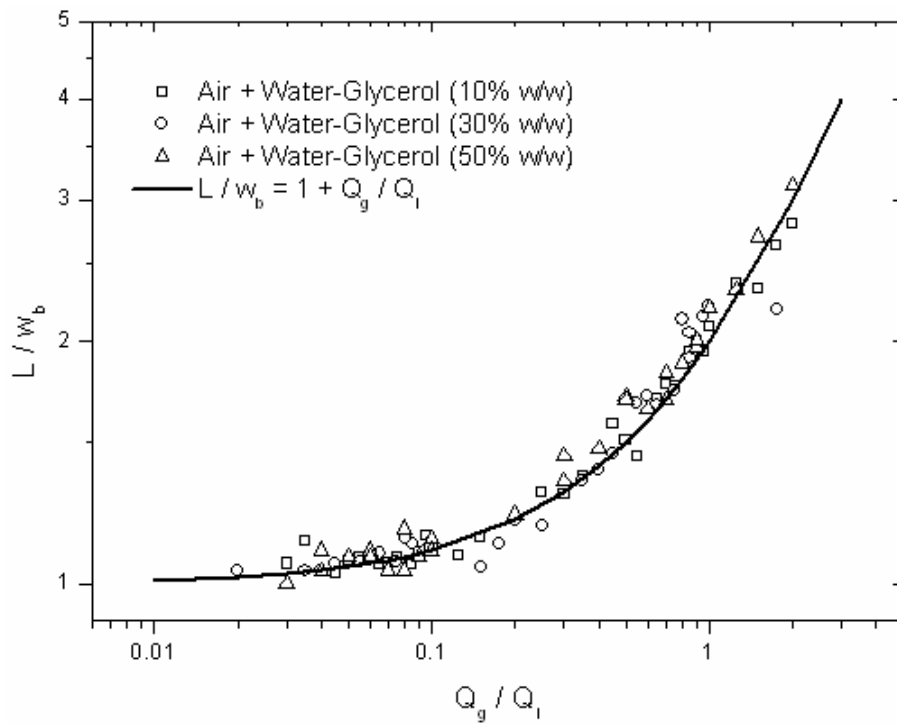


Figure 5-14. Dimensionless ratio (L/w_b) with the ratio of gas and liquid flow rates

A

Q_l/Q_g	Air + Water $\sigma = 72\text{mN/m}, \mu = 0.92 \text{ mPa}\cdot\text{s}$	Air + Water-Glycerol (10%) $\sigma = 72\text{mN/m}, \mu = 1.19 \text{ mPa}\cdot\text{s}$	Air + Water-Glycerol (30%) $\sigma = 72\text{mN/m}, \mu = 2.68 \text{ mPa}\cdot\text{s}$	Air + Water-Glycerol (50%) $\sigma = 72\text{mN/m}, \mu = 7.31 \text{ mPa}\cdot\text{s}$	Air + Water-Tween20 $\sigma = 37\text{mN/m}, \mu = 0.92 \text{ mPa}\cdot\text{s}$
0.1					
0.5					
1					

B

Q_l/Q_g	Air + Water $\sigma = 72\text{mN/m}, \mu = 0.92 \text{ mPa}\cdot\text{s}$	Air + Water-Glycerol (10%) $\sigma = 72\text{mN/m}, \mu = 1.19 \text{ mPa}\cdot\text{s}$	Air + Water-Glycerol (30%) $\sigma = 72\text{mN/m}, \mu = 2.68 \text{ mPa}\cdot\text{s}$	Air + Water-Glycerol (50%) $\sigma = 72\text{mN/m}, \mu = 7.31 \text{ mPa}\cdot\text{s}$	Air + Water-Tween20 $\sigma = 37\text{mN/m}, \mu = 0.92 \text{ mPa}\cdot\text{s}$
0.1					
0.5					
1					

Figure 5-13. Bubble shapes at different viscosities and surface tensions: A) $Q_l = 21\text{ml/h}$ B) $Q_l = 42\text{ml/h}$

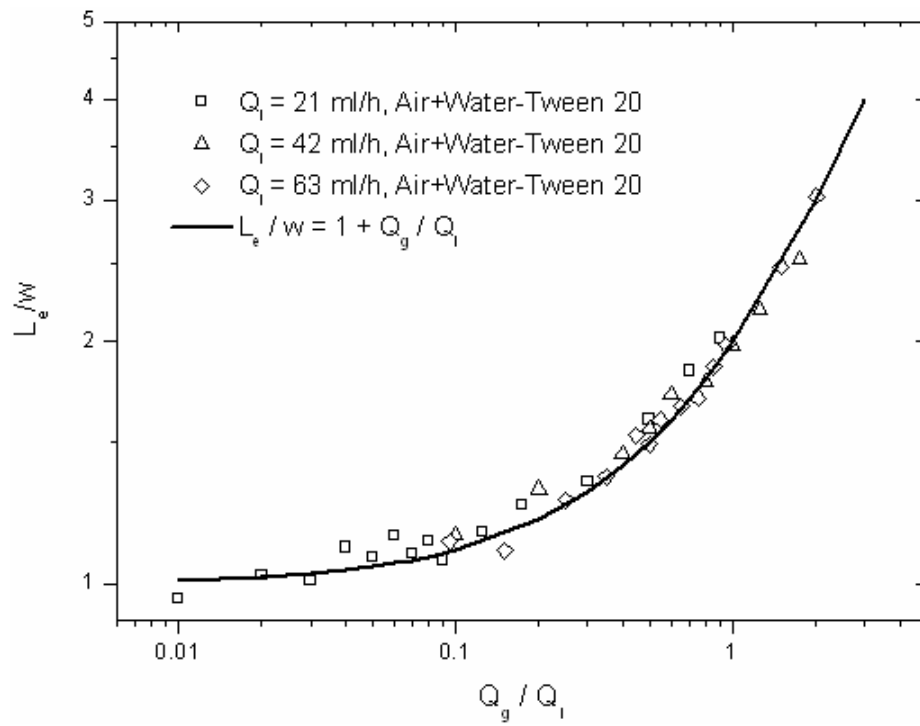


Figure 5-15. Dimensionless ratio (L_e/w) with the ratio of gas and liquid flow rates

CHAPTER 6 CONCLUSIONS AND RECOMMENDATIONS

In this research, many features of the single- and two-phase pressure-driven flows in micro-channels were experimentally and numerically investigated. Major accomplishments and recommendations for future research are provided in the following.

6.1 Accomplishments and Findings

1. For straight micro-channels, the experimental Poiseuille numbers show agreement with standard laminar incompressible flow predictions when the Re is less than a value around 1500. The discrepancy observed by the former researchers is the result of unaccounted bias in experiment setups, such as not accounting for increased pressure drop in the entrance region or unreliable inlet and outlet losses.
2. The flow micro structures around the bend of a serpentine micro-channel can be divided into three categories depending on the flow Reynolds number. When $Re < 100$, there is no induced flow recirculation and flow separation. When $Re > 100$, vortices and flow separation appear and further develop. The outer corner vortex develops along the wall of the channel, and the vortex center moves slightly from the upper stream to the down stream with the increasing of the Re number. The inner wall vortex due to flow separation develops immediately after the flow makes the turn. When $Re > 1000-1500$, the shape and size of the outer and inner vortices become almost constant.
3. In serpentine micro-channels, the additional pressure drop due to miter bends can be divided into two groups. The first group is for $Re < 100$ where there is no eddies and the additional pressure drop is very small for all of the channels. The other group is for flows with the Reynolds numbers exceeding the threshold values that are in the range of 100-300. When the Reynolds is higher than the threshold value, we found the flow separation and formation of vortices that appear on the inner and outer wall around the miter bend. These vortices increase in strength with increasing Re number that causes the bend pressure drop to increase sharply with the Re number. The experimental results also show the bend pressure drop increases with decreasing hydraulic diameters. Bend loss coefficient K_b is a function of the Re number only when $Re < 100$, a function of the Re number and channel size when $Re > 100$, and almost keeps constant and changes in the range of $\pm 10\%$ when Re is larger than some value in 1000-1500. The trend of the experimental pressure drop is consistent with the flow structure change.
4. The phenomenon that micro-channel flow pattern changes with time at a fixed location under a certain gas and liquid superficial velocity was found, which can be attributed to the density wave oscillation in the micro-channel. According to the appearance of the transition flow patterns such as “liquid ring flow”, “liquid lump flow” and “disruption tail of the slug”, four flow patterns can be defined for micro-channels with the hydraulic diameters of 0.412 mm and 0.622 mm: bubbly-slug flow, slug-ring flow, dispersed-churn flow and annular flow. For the micro-channel with the hydraulic diameters of 0.209 mm, the bubbly-slug flow became

the slug-flow and the dispersed flow disappeared. The current flow regime maps show the transition boundary lines shift to high We_{GS} or gas superficial velocity with the decreasing of the hydraulic diameter. It can be explained by the strong surface tension effect in micro-channels. The micro-channel flow maps were compared with the mini-channel flow map based on the Weber number model, which showed poor agreement.

5. Time-averaged void fractions of each micro-channel were measured for 22 runs to cover the whole range of homogeneous void fraction. The data of each run were obtained from the analysis of 8000 flow pattern images captured at a certain gas and liquid superficial velocity. With the decreasing of the hydraulic diameter, the time-average void fraction showed a non-linear relationship with the homogeneous void fraction. A new empirical correlation was proposed to predict the non-linear relationship, and most of the current experimental data and Kawaraha's (2002) data fall within $\pm 15\%$ of the new correlation. The uncertainty of this measurement method was analyzed and the uncertainty range was approximately from 3.1% to 9.8% under the current experimental conditions. The results of this study provide basic information of the effects of length scale reduction on nitrogen-water two-phase flow characteristics in micro-scale channels that would be useful for the design of gas-liquid transport and their separation encountered in low-temperature fuel cells.
6. In a micro-bubble dispenser with co-flowing structure, bubble break-up is obtained by the pressure drop resulting from the sudden velocity distribution change around the barrier. It is periodic under certain operating conditions, and it becomes unsteady and nonperiodic when Q_l is less than some critical values or Q_g/Q_l is too large. The process has two steps: gas ligament expansion and collapse.
7. The bubble length L is dependent on Q_g and Q_l , and has a quantitative relationship with channel width w and Q_g/Q_l , which is the same as that used for the T-junction since the break-up process becomes similar with that of T-junction under the operating conditions. At the low frequency region, bubble generation frequency is a function of channel width w , channel depth h and $Q_l Q_g / (Q_g + Q_l \cdot \pi/4)$. This functional relationship provides a good prediction at the low frequency region. The liquid viscosity affects the film thickness while the surface tension changes the bubble shape. The dimensionless bubble length L/w can still be predicted by a modified equation which uses the real bubble width w_b or an equivalent bubble length L_e .

6.2 Future Research

Future research to further understand the micro-scale pressure-driven flow can be performed both experimentally and numerically.

6.2.1 Experimental Study

1. Segmented bubble transport in serpentine micro-channels to compare with gas-liquid two-phase flow motion and transport in straight micro-channels.
2. Rapid micro-T-junction mixer.

3. Droplet transport in micro-T-junction and serpentine micro-channels.

6.2.2 Numerical Study

1. A general micro-scale two-phase flow model incorporate the inertia force, viscous force, surface tension force to predict the flow patterns, void fraction and frictional pressure drop.
2. A new model to predict the enhanced mixing induced by the segmented micro-bubble/droplet

APPENDIX
TIMING PROGRAM FOR MICRO-PARTICLE IMAGE VELOCIMETRY

The timing controller LC880 needs to be programmed to synchronize the laser and CCD camera. The following channels refer to:

Channel A: Reference clock
Channel B: Control the CCD Camera
Channel C: Control the Flashlamp of laser 1
Channel D: Control the Q-Switch of laser 1
Channel E: Control the Flashlamp of laser 2
Channel F: Control the Q-Switch of laser 2

Overall LC880 settings: Programming preset A, Using 40 MHz internal clock.

Channel A:

Free-running clock: High duration: 1.000000 ms; low duration: 1.000000 ms.

Channel B:

Delayed pulse: Delay after trigger 50.000000 ns then pulse output 1.000000 ms. Invert output (pulse from high to low).

Triggering options: Trigger on rising edge. Skip 100 triggers before triggering.

Trigger Input Logic:

inB = outA;

Channel C:

Delayed pulse: Delay after trigger 0.853800 ms then pulse output 15.000000 us.

Triggering options: Trigger on rising edge. Unlimited retriggering.

Trigger Input Logic:

inC = not outB;

Channel D:

Delayed pulse: Delay after trigger 152.000000 us then pulse output 15.000000 us.

Triggering options: Trigger on rising edge. Unlimited retriggering.

Trigger Input Logic:

inD = outC;

Channel E:

Delayed pulse: Delay after trigger 0.856300 ms then pulse output 15.000000 us.

Triggering options: Trigger on rising edge. Unlimited retriggering.

Trigger Input Logic:

inE = not outB;

Channel F:

Delayed pulse: Delay after trigger 152.000000 us then pulse output 15.000000 us.

Triggering options: Trigger on rising edge. Unlimited retriggering.

Trigger Input Logic:

inF = outE;

LIST OF REFERENCES

- Akbar, M.K., Plummer, D.A., Ghiaasiaan, S.M., 2003. On gas-liquid two-phase flow regimes in microchannels. *Int. J. Multiphase Flow* 29, 855-865.
- Ali, M.I., Sadatomi, M., Kawaji, M., 1993. Two-phase flow in narrow channels between two flat plates. *Can. J. Chem. Eng.* 71, 657-666.
- Armand, A.A., 1946. The resistance during the movement of a two-phase system in horizontal pipes. *Izv.V.T.I.* 1, 16-21.
- Brandner, J., Fichtner, M., Schygulla, U., Schubert, K., 2000. Improving the efficiency of micro heat exchangers and reactors. in *Proc. 4th Int. Conf. Microreaction Technology*, AIChE, March 5-9, Atlanta, GA, 244-249.
- Batchelor, G.K., 1977. Developments in micro-hydrodynamics. in *Theoretical and Applied Mechanics*, ed. W Koiter. 33-35.
- Beebe, D.J., Mensing, G.A., Walker, G.M., 2002. Physics and applications of microfluidics in biology. *Aun Rev. Biomed. Eng.* 4, 261-286.
- Berger, S.A., Talbot, L., Yao, L.S., 1983. Flow in curved pipes. *Annu. Rev. Fluid Mech.* 15, 461-512.
- Bradshaw, P., 1987. Turbulent secondary flows. *Annu. Rev. Fluid Mech.* 19, 53-74.
- Brutin, D., Tadrist, L., 2003. Experimental friction factor of a liquid flow in microtubes. *Phys. Fluids* 15, 653-661.
- Cubaud, T., Tatineni, M., Zhong, X.L., Ho, C.M., 2005. Bubble dispenser in microfluidic devices. *Phys. Rev. E* 72, 037302.
- Chen, W.L., Twu, M.C., Pan, C., 2002. Gas-liquid two-phase flow in micro-channels. *Int. J. Multiphase Flow* 28, 1235-1247.
- Chung, P.M.-Y., Kawaji, M., 2004. The effect of channel diameter on adiabatic two-phase flow characteristics in microchannels. *Int. J. Multiphase Flow* 30, 735-761.
- Coleman, J.W., Garimella, S., 1999. Characteristics of two-phase patterns in small diameter round and rectangular tubes. *Int. J. Heat Mass Transfer* 42, 2869-2881.
- Collier, J.G., Thome, J.R., 1994. *Convective boiling and condensation*. Third ed., Oxford University Press, Oxford.
- Dreyfus, R., Tabeling, P., Williams, H., 2003. Ordered and disordered patterns in two-phase flow in microchannels. *Phys. Rev. Lett.* 90, 144505.
- Erickson, D., Li, D., 2004. Integrated microfluidic devices. *Anal. Chim. Acta* 507, 11-26.

- Flockhart, S.M., Dhariwal, R.S., 1998. Experimental and numerical investigation into the flow characteristics of channels etched in <100> silicon. *J. Fluids Eng.* 120, 291-295.
- Fu, A.Y., Spence, C., Scherer, A., Arnold, F.H., Quake, S.R., 1999. A microfabricated fluorescence-activated cell sorter. *Nat. Biotechnol.* 17, 1109-1111.
- Ganan-Calvo, A.M., Gordillo, J.M., 2001. Perfectly monodisperse microbubbling by capillary flow focusing. *Phys. Rev. Lett.* 87, 274501.
- Garstecki, P., Fuerstman, M.J., Stone, H.A., Whitesides, G.M., 2006. Formation of droplets and bubbles in a microfluidic T-junction - scaling and mechanism of break-up. *Lab Chip* 6, 437-446
- Garstecki, P., Gitlin, I., DiLuzio, W., Whitesides, G.M., Kumacheva, E., Stone, H.A., 2004. Formation of monodisperse bubbles in a microfluidic flow-focusing device. *Appl. Phys. Lett.* 85, 2649-2651.
- Ghiaasiaan, S.M., Abdel-Khalik, S.I., 2001. Two-phase flow in micro-channels. *Advances in Heat Transfer* 34, Academic Press, New York, 145.
- Gordillo, J.M., Cheng, Z.D., Ganan-Calvo, A.M., Marquez, M., Weitz, D.A., 2004. A new device for the generation of microbubbles. *Phys. Fluids* 16, 2828-2834.
- Gui, L., Wereley, S. T., 2002. A correlation-based continuous window shift technique for reducing the peak locking effect in digital PIV image evaluation. *Exp. Fluids* 32, 506-517.
- Gui, L., Wereley, S. T., Lee, S. Y., 2002. Digital filters for reducing background noise in micro PIV measurement. *Proc. of the 11th International Symposium on the Application of Laser Techniques to Fluid Mechanics*, 151, Lisbon, Portugal, July 8-11.
- Guillot, P., Colin, A., 2005. Stability of parallel flows in a microchannel after a T junction. *Phys. Rev. E* 72, 066301.
- Haverkamp, V., Hessel, V., Loewe, H., Menges, G., Warnier, J.F.M., Rebrov, E.V., de Croon, M.H.J. M., Schouten, J.C., Liauw, M.A., 2006. Hydrodynamics and mixer-induced bubble formation in micro bubble columns with single and multiple-channels. *Chem. Eng. Technol.* 29, 1015-1026.
- Heinzel, A., Hebling, C., Muller, M., Zedda, M., Muller, C., 2002. Fuel cells for low power applications. *J. of Power Sources* 105, 250-255.
- Hetsroni, G., Mostak, A., Pogrebnyak, E., Yarin, L.P., 2005. Fluid flow in micro-channels. *Int. J. Heat Mass Transfer* 48, 982-1998.
- Ho, C.M., Tai, Y.C., 1998. Micro-electro-mechanical systems (MEMS) and fluid flows. *Annu. Rev. Fluid Mech.* 30, 579-612.

- Huang, H. T., Fiedler, H. E., Wang, J. J., 1993. Limitation and improvement of PIV, Part II: particle image distortion, a novel technique. *Exp. Fluids* 15, 263-273.
- Humphrey, J.A.C., Taylor, A.M.K., Whitelaw, J.H., 1981. Turbulent-flow in a square duct with strong curvature. *J. Fluid Mech.* 103, 443-463.
- Jiang, X.N., Zhou, Z.Y., Yao, J., Li, Y., Ye, X.Y., 1995. Micro-fluid flow in microchannel. In: *Proc. the 8th Int. Conf. on Solid State Sensors, Actuators and Eurosensors IX*, Sweden, 317-320.
- Judy, J., Maynes, D., Webb, B.W., 2002. Characterization of frictional pressure drop for liquid flows through microchannels. *Int. J. Heat Mass Transfer* 45, 3477-3489.
- Kakac, S., Shah, R.K., Aung, W., 1987. *Handbook of single-phase convective heat transfer*. John Wiley and Sons, New York.
- Kawahara, A., Chung, P.M.-Y., Kawaji, M., 2002. Investigation of two-phase flow pattern, void fraction and pressure drop in a microchannel. *Int. J. Multiphase Flow* 28, 1411-1435.
- Kohl, M.J., Abdel-Khalik, S.I., Jeter, S.M., Sadowski, D.L., 2005. An experimental investigation of microchannel flow with internal pressure measurements. *Int. J. Heat Mass Transfer* 48, 1518-1533.
- Kushida, G., Yamashita, H., Izumi, R., 1985. Study on three-dimensional flow and heat transfer in miter-bend (3rd report, effects of Reynolds number and aspect ratio), *Bulletin of JSME* 28, 2000-2006.
- Lee, H.J., Lee, S.Y., 2001. Pressure drop correlations for two-phase flow within horizontal rectangular channels with small heights. *Int. J. Multiphase Flow* 27, 783-796.
- Lee, S.Y.K., Wong, M., Zohar, Y., 2001. Gas flow in microchannels with bends. *J. Micromecha. Microeng.* 11, 635-644.
- Li, H., Olsen, M.G., 2006. MicroPIV measurements of turbulent flow in square microchannels with hydraulic diameters from 200 μ m to 640 μ m. *Int. J. Heat Fluid Flow* 27, 123-134.
- Li, Z.X., Du, D.X., Guo, Z.Y., 2003. Experimental study on flow characteristics of liquid in circular micro-tubes. *Microscale Thermophys. Eng.* 7, 253-265.
- Lockhart, R.W., Martinelli, R.C., 1949. Proposed correlation of data for isothermal two-phase, two-component flow in pipes. *Chem. Eng. Prog.* 45, 39-48.
- Maharudrayya, S., Jayanti, S., Deshpande, A. P., 2004. Pressure losses in laminar flow through serpentine channels in fuel cell stacks. *J. of Power Sources* 138 (1-2), 1-13.
- Mala, G.M., Li, D., 1999. Flow characteristics of water in microtubes. *Int. J. Heat Fluid Flow* 20, 142-148.

- Mandhane, J.M., Gregory, G.A., Aziz, K., 1974. Flow pattern map for gas-liquid flow in horizontal pipes. *Int. J. Multiphase Flow* 1, 537-553.
- Meinhart, C.D., Wereley, S.T., Gray, M.H.B., 2000a. Volume illumination for two-dimensional particle image velocimetry. *Meas. Sci. Technol.* 11, 809-814.
- Meinhart, C.D., Wereley, S. T., Santiago, J.G., 2000b. A PIV algorithm for estimating time-averaged velocity fields. *J. Fluids Engineering* 122, 285-289.
- Meinhart, C.D., Wereley, S.T., Santiago, J.G., 1999. PIV measurements of a microchannel flow. *Exp. Fluids* 27, 414-419.
- Mishima, K., Hibiki, T., 1996. Some characteristics of air-water two-phase flow in small diameter vertical tubes. *Int. J. Multiphase Flow* 22, 703-712.
- Mishima, K., Ishii, M., 1984. Flow regime transition criteria for upward two-phase flow in vertical tubes. *Int. J. Heat Mass Transfer* 27, 723-730.
- Nguyen, N.T., Wereley, S. T., 2002. *Fundamentals and applications of microfluidics. MEMS Series.* Artech House, Norwood, MA.
- Nguyen, N., Wereley, S.T., 2006. *Fundamentals and applications of Microfluidics. 2nd Edition,* Artech House, Boston.
- Oak, J., Pence, D.V., Liburdy, J.A., 2004. Flow development of co-flowing streams in rectangular micro-channels. *Microscale Therm. Eng.* 8, 111-128.
- Peng, X.F., Peterson, G. P., 1996. Convective heat transfer and flow friction for water flow in microchannel structures. *Int. J. Heat Mass Transfer* 39, 2599-2608.
- Peng, X.F., Peterson, G.P., Wang, B.X., 1994. Frictional flow characteristics of water flowing through rectangular microchannels. *Exp. Heat Transfer* 7, 249-264.
- Pfund, D., Rector, D., Shekarritz, A., 2000. Pressure drop measurements in a micro channel. *AIChE J.* 46, 1496-1507.
- Prasad, A.K., Adrian, R.J., Landreth, C.C., Offutt, P.W., 1992. Effect of resolution on the speed and accuracy of particle image velocimetry interrogation. *Exp. Fluids* 13, 105-116.
- Qu, W., Mala, G.M., Li, D., 2000. Pressure-driven water flows in trapezoidal silicon microchannels. *Int. J. Heat Mass Transfer* 43, 353-364.
- Qu, W., Yoon, S.M., Mudawar, I., 2004. Two-phase flow and heat transfer in rectangular micro-channels. *J. Electronic Packaging* 126, 288-300.
- Santiago, J.G., Wereley, S.T., Meinhart, C.D., Beebe, D.J., Adrian, R.J., 1998. A particle image velocimetry system for microfluidics. *Exp. Fluids* 25, 316-319.

- Sevilla, A., Gordillo, J.M., Martinez-bazan, C., 2005. Bubble formation in a coflowing air-water stream. *J. Fluid Mech.* 530, 181-195.
- Shah, R.K., London, A.L., 1978. *Advances in Heat Transfer, Suppl. 1.* Academic Press, New York.
- Sharp, K.V., Adrian, R.J., Beebe, D.J., 2000. Anomalous transition to turbulence in microtubes. In: *Proc. Int. Mech. Eng. Cong. Expo., 5th Micro-Fluidic Symp.*, Nov. 5-10, Orlando, FL.
- Song, H., Tice, J.D., Ismagilov, R.F., 2003. A microfluidic system for controlling reaction networks in time. *Angew. Chem. Int. Ed.* 42, 768-772.
- Stone, H.A., Kim, S., 2001. Microfluidics: basic issues, applications, and challenges. *AICHE J.* 47, 1250-1254.
- Stone, H.A., Stroock, A.D., Ajdari, A., 2004. Engineering flows in small devices: microfluidics toward a lab-on-a-chip. *Annu. Rev. Fluid. Mech.* 36, 381-411.
- Streeter V. L., 1961. *Handbook of fluid dynamics.* McGraw-Hill, New York.
- Tabatabai, A., Faghri, A., 2001. A new two-phase flow map and transition boundary accounting for surface tension effects in horizontal miniature and micro tubes. *J. Fluids Eng.-Trans. ASME*, 123, 958-966.
- Taitel, T., Barnea, D., Dukler, A.E., 1980. Modeling flow pattern transitions for steady upward gas-liquid flow in vertical tubes. *AICHE J.* 26, 345-350.
- Taitel, Y., Dukler, A.E., 1976. A model for predicting flow regime transitions in horizontal and near horizontal gas-liquid flow. *AICHE J.* 22, 47-55.
- Triplett, K.A., Ghiaasiaan, S.M., Adbel-Khalik, S.I., Sadowski, D.L., 1999. Gas-liquid two-phase flow in microchannels. Part I: two-phase flow patterns. *Int. J. Multiphase Flow* 25, 377-394.
- Triplett, K.A., Ghiaasiaan, S.M., Adbel-Khalik, S.I., Sadowski, D.L., 1999. Gas-liquid two-phase flow in microchannels. Part II: void fraction and pressure drop. *Int. J. Multiphase Flow* 25, 395-410.
- Wereley, S. T., Gui, L., 2003. A correlation-based central difference image correction (CDIC) method and application in a four-roll mill flow PIV measurement. *Exp. Fluids* 34, 42-51.
- Wereley, S.T., Meinhart, C.D., 2001. Second-order accurate particle image velocimetry. *Exp. Fluids* 31, 258-268.
- White, F.M., 1991. *Viscous fluid flow, 2nd edition.* McGraw-Hill, New York.
- Wilding, P., Pfahler, J., Bau, H.H., Zemel, J.N., Kricka, L.J., 1994. Manipulation and flow of biological fluids in straight channels micromachined in silicon. *Clin. Chem.* 40, 43-47.

- Wilmarth, T., Ishii, M., 1994. Two-phase flow regimes in narrow rectangular vertical and horizontal channels. *Int. J. Heat Mass Transfer* 37, 1749-1755.
- Wu, H.Y., Cheng, P., 2003. Friction factors in smooth trapezoidal silicon microchannels with different aspect ratios. *Int. J. Heat Mass Transfer* 46, 2519-2525.
- Wu, P., Little, W.A., 1983. Measurement of friction factors for the flow of gases in very fine channels used for microminiature Joule-Thomson refrigerators. *Cryogenics* 23, 273-277.
- Xiong, R.Q., Chung, J.N., 2007a. Flow characteristics of water in straight and serpentine microchannels with miter bends. *Exp. Therm. Fluid Sci.* 31, 805-812.
- Xiong, R.Q., Chung, J.N., 2007b. An experimental study of the size effect on adiabatic gas-liquid two-phase flow patterns and void fraction in micro-channels. *Phys. Fluids* 19, 033301.
- Xu, B., Ooi, K.T., Wong, N.T., Choi, W.K., 2000. Experimental investigation of flow friction for liquid flow in microchannels. *Int. Comm. Heat Mass Transfer* 27, 1165-1176.
- Xu, J.H., Li, S.W., Wang, Y.J., Luo, G.S., 2006. Controllable gas-liquid phase flow patterns and monodisperse microbubbles in a microfluidic T-junction device. *Appl. Phys. Lett.* 88, 133506.
- Yamashita, H., Kushida, G., Izumi, R., 1984. Study on three-dimensional flow and heat transfer in miter-bend (1st report, analysis of flow in laminar region). *Bulletin of JSME* 27, 1905-1912.
- Yamashita, H., Izumi, R., Kushida, G., Mizuno, T., 1986. Fluid flow and heat transfer in a two-dimensional miter-bend (1st report, experiments and analysis). *Bulletin of JSME* 29, 4164-4169.
- Yang, C.Y., Shieh, C.C., 2001. Flow pattern of air-water and two-phase R-134a in small circular tubes. *Int. J. Multiphase Flow* 27, 1163-1177.
- Zhang, L., Koo, J.M., Jiang, L., Asheghi, M., Goodson, K.E., Santiago, J.G., Kenny, T.W., 2002. Measurements and modeling of two-phase flow in microchannels with nearly constant heat flux boundary conditions. *J. MEMS* 11, 12-19.
- Zhao, T.S., Bi, Q.C., 2001. Co-current air-water two-phase flow patterns in vertical triangular microchannels. *Int. J. Multiphase Flow* 27, 765-782.
- Zheng, B., Tice, J.D., Ismagilov, R.F., 2004. Formation of arrayed droplets of soft lithography and two-phase fluid flow, and application in protein crystallization. *Adv. Mater.* 16, 1365-1368.
- Zuber, N., Findlay, J.A., 1965. Average volumetric concentration in two-phase flow systems. *ASME J. Heat Transfer* 87, 453-459.

BIOGRAPHICAL SKETCH

Renqiang Xiong was born in 1978, in China. He grew up predominantly in Jingdezhen city, Jiangxi Province, China, and received his Bachelor of Science in energy engineering and Master of Science in optical engineering from Zhejiang University in June 1999 and May 2002, respectively. Renqiang moved to the Sunshine state in Spring 2003 and enrolled in the Department of Mechanical and Aerospace Engineering at the University of Florida where he received a Master of Science in mechanical engineering with minor in statistics in August 2005. He then continued to pursue his PhD degree and worked as a research assistant on a part-time basis with Dr. Jacob N Chung. In the meantime, he is also pursuing a Master of Science in electrical and computer engineering. His research interests include microfluidics, micro-PIV, MEMS, and cryogenics.